Trinity College Dublin
Coláiste na Tríonóide, Baile Átha Cliath
The University of Dublin

# Optimisation and 3D Printing of Paediatric Stents

By

Samuel Geraghty

A thesis submitted in partial fulfilment of the requirement of a Master in Science (M.Sc. (Ind.)) in Mechanical, Manufacturing and Biomedical Engineering

Supervisor:
Prof. Caitríona Lally

Trinity College Dublin

30th of January 2023

# Abstract

Aortic coarctation is a congenital heart defect that occurs 3 per 10,000 live births with a life expectancy of 35 years if left untreated. Stenting is a common treatment method, but devices are not specifically designed for paediatric patients, leading to off label stent use and potentially hazardous device modifications. The combination of unique pathologies and low patient numbers associated with aortic coarctation leads to little commercial incentive to develop devices for this patient cohort. This study has the overarching aim of investigating the feasibility of developing devices for this population with additive manufacturing (AM).

A stent design inspired by commercial devices was adapted and produced by AM. A post-processing parameter study was conducted to enable the manufacture of an open cell varied diameter stent not easily fabricated with typical stent manufacturing techniques. Furthermore, these devices were tested mechanically to analyse their radial strength and flexibility. Geometric properties such as strut thickness and surface roughness were also measured to gain insight into the relationship between post-processing technique parameters and stent properties.

These devices were compared to contemporary commercial and additively manufactured stents previously presented in the literature. Analysis of surface roughness and strut thickness showed the stents produced in this work have the lowest surface roughness and strut thickness for AM stents to date and are comparable to commercial devices. The analysis of mechanical properties showed these devices are less radially stiff and more flexible than contemporary commercial stents and AM stents to date. Overall, these results prove the feasibility of using AM to produce stents with a wide range of geometric and mechanical properties with AM.

In summary, this work pushes the boundaries of AM fabrication showing the feasibility of developing devices with an open-cell design and varied diameter. The use of AM and the post-processing techniques presented in this work proves the viability of developing stents with tuneable local mechanical and geometric properties. AM enables rapid prototyping and feasible manufacture of these devices which may enable the commercial viability of disease or patient specific devices in future work.

## Declaration

I declare that this thesis has not been submitted as an exercise for a degree at this or any other

university and it is entirely my own work.

I agree to deposit this thesis in the University's open access institutional repository or allow the Library to do so on my behalf, subject to Irish Copyright Legislation and Trinity College Library conditions of use and acknowledgement.

I consent to the examiner retaining a copy of the thesis beyond the examining

period, should they so wish (EU GDPR May 2018).

30/01/2023

## Acknowledgments

Firstly, I would like to thank Prof. Caitríona Lally for the advice, guidance, and support over the past two years. I am grateful for the opportunity to have worked in and been a part of the Lally Lab. I would like to thank SFI and AMBER for making this work possible.

I would like to acknowledge the support and guidance of the Lally Lab past and present. Specifically, Dr. Orla McGee, Dr. Ciara McKenna, Dr. Robert Johnston, Dr. Niall Linnane, Dr. Harry Shipley, Peter O'Reilly, and Conor O'Keeffe for their help related to this project. Special mention to Celia and Yasmine, beginning this journey at the same time, I wish you both the best of luck with your future research journeys.

Finally, I wish to thank my family for their support and encouragement throughout my studies. As well, Caoimhe and Janet from our time at Royal Oak, you both made this journey much easier through past unprecedented times.

# List of Journal Publications, Conference Proceedings and Awards

## Journal Articles

McGee, O., Geraghty, S., Hughes, C., Jamshidi, P., Kenny, D., Attallah, M. and Lally, C., 2022. An investigation into patient-specific 3D printed titanium stents and the use of etching to overcome Selective Laser Melting design constraints. Journal of the Mechanical Behavior of Biomedical Materials, 134, p.105388.

## Conference Proceedings

Geraghty, S., McGee, O., Jamshidi, P., Garrard, R., Attallah, M., Kenny, D. and Lally, C. (2022) Chemical Etching of 3D Printed Patient Specific Paediatric Stents, in *Proceedings of the 11th European Solid Mechanics Conference, Galway, Ireland*

Geraghty, S., McGee, O., Jamshidi, P., Garrard, R., Attallah, M., Kenny, D. and Lally, C. (2022) Chemical Etching as a Method to Overcome Design Constraints of 3D Printed Titanium and Nitinol Stents, in *Proceedings of the 27th Annual Conference of the Section of Bioengineering of the Royal Academy of Medicine in Ireland, Galway Ireland*

McGee, O., Geraghty, S., Jamshidi, P., Kenny, D. Attallah, M. and Lally, C. (2021) The Use of Etching to Overcome Design Restrictions of the SLM Technique when 3D Printing Titanium Stents, in *Proceedings of the 26th Congress of the European Society of Biomechanics (Online)*

## Awards

3rd Prize Medtronic Best Medical Devices Research Oral Presentation, Royal Academy of Medicine in Ireland (RAMI) Section of Bioengineering, May 2022

# Table of Contents

# List of Figures

# List of Tables

# Chapter 1. Introduction

Aortic coarctation is defined as a discrete narrowing of the aorta [1], such as that seen in Figure 1. This typically occurs in the ascending aorta and affects 3 per 10,000 live births worldwide with an average life expectancy of 35 years if untreated [2]. Available treatments for this condition include surgical anastomosis, balloon angioplasty and stenting which has been identified as the most effective method of treatment [2]. There exists limitations associated with the use of stents, devices are not specifically designed for paediatric patients and the majority are used on an off-label basis, such as the use of biliary stents. This can require hazardous modification of devices such as cutting a device to shorten it, resulting in inferior long-term outcomes for these patients. There is also the concern of aortic wall injury leading to aneurysm formation or aortic dissection. [3] notes an injury rate of 12% for patients treated using stents for aortic coarctation. The development of stents optimised for paediatric patient anatomy could deliver more favourable long-term clinical outcomes and improved long-term health for patients.

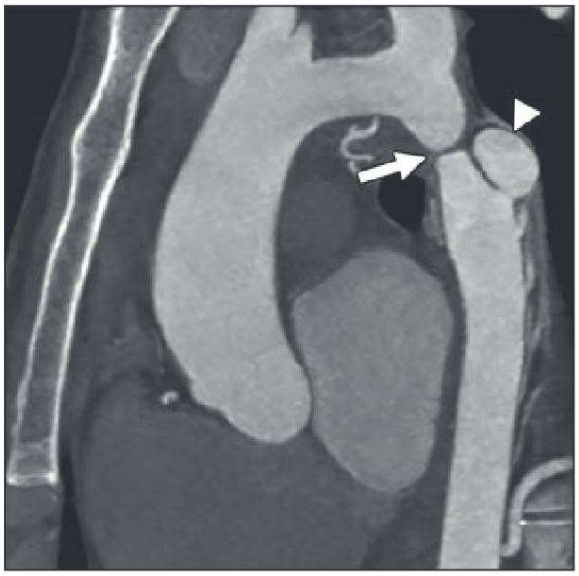

Figure 1. Cardiac MRI of patient with severe aortic coarctation [4]

An improved understanding of the physiological effects of stent design has led to decreased prevalence of restenosis [5]. Within the context of congenital heart disease (CHD), the choice of products on the market available to paediatricians remains limited [6]. This consequently leads to a heavy reliance on off-label use of devices. A study in 2008 noted up to 90% of cardiac catheterization devices used in a paediatric setting were off-label [7], commonly used stents include the Palmaz P188. Palmaz 3010, Genesis 19 and, DoubleStrut

and LD Mega variants of the IntraStent [3] This technological gap may be explained by the limited financial incentive for the development and commercialisation of devices for a relatively small patient population [8]. In the context of aortic coarctation, this problem is exacerbated by the heterogeneous nature of the disease state pathology [1].

Stents currently used for coarctation treatment are typically open cell laser cut designs with a constant diameter and strut thickness lending to constant mechanical properties over the device length. The use of these stents may not be optimal for coarctation treatment. The heterogeneous nature of this disease state and affected tissue, such as vessel curvature can lead to issues related to vessel straightening or exerting excess pressure on healthy tissue to obtain the required lumen gain. Stents with design characteristics, such as varied diameter [9], changing strut thickness [10] and tapered strut profiles [11], may be better suited to this application. These design features could enable the development of stents with local tuneable mechanical properties suitable for the heterogenous nature of aortic coarctation. These design features are difficult to fabricate with current stent manufacturing techniques as balloon expandable stents are typically laser cut from constant diameter tubing. The fabrication of these devices would require custom tubing and complex laser cutting control techniques to manufacture. This would lead to increased costs and thus even less commercial incentive to bring these potential devices to market given the low patient numbers.

Additive manufacturing (AM) techniques such as laser powder bed fusion (LPBF) may be an alternative technique to feasibly manufacture devices with these design features and push the boundaries of stent design by enabling greater design freedom. AM enables the fabrication of multiple devices with complex shapes and geometries within a single production cycle. This may also enable the development of patient-specific devices. Work to date concerning AM stents has shown the feasibility of printing stents [9], [12]–[16] and the use of post-processing to realize open cell stent designs [17]. Little work to date has recreated commercial stent designs and conducted a comparative analysis of mechanical and geometrical properties of AM and commercial stents. There has also been little work in developing a controlled and predictable post-processing technique to achieve stent design freedom and control device properties such as flexibility and radial strength. Consequently, this project aims to recreate a commercial stent design using AM and compare the mechanical and geometrical properties of these devices. Additionally, this project aims to display the feasibility of using AM and post-processing to both control device properties and achieve increased stent design freedom.

# Chapter 2. Literature Review

## 2.1 Additive Manufacturing (AM) of Metal Stents

The earliest incidence of AM metal stents in the literature is from the work of Wessarges *et al.* in 2014 [12]. Here 4 helical design variations fabricated from 316L stainless steel were examined by investigating their expansion behaviour through balloon expansion. Radial and flexural properties were also examined through mechanical testing. This study exhibited the feasibility of producing AM stents but also noted issues with crack formation from balloon expansion.

The work of Demir *et al.* [18] provided insight into the application of design for additive manufacturing (DfAM) to stent design by outlining several design rules as shown:

1. The print angle should be greater than or equal to 45relative to the layer plane.
2. All overhang features should be less than 1mm in length.
3. Where bridging features exist, these should be limited to a length of less than 4mm.
4. A minimum feature distance of 0.3mm should be enforced.

An illustration of these design rules is given in Figure 2.

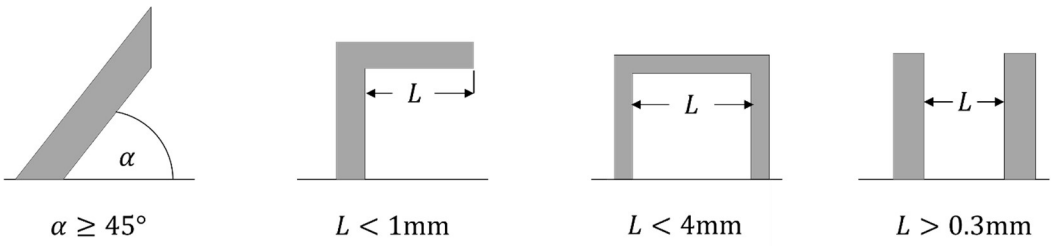


Figure 2 Illustration of design rules for AM, inspired by [18]

There are several materials available as feedstock for additive manufacturing, a summary of which is presented in Table 1. Previous work has indicated that AM Ti6Al4V has a lower Young's Modulus after heat treatment compared to CoCr or SS316L, enabling less resistance to deformation, an important factor in device deliverability. Additionally, Ti6Al4V has been shown to have similar failure strain quantities to AM CoCr a common stent material and a greater ultimate tensile strength in comparison to SS316L. In summary, the material properties of AM Ti6Al4V may enable the manufacture of devices with less resistance to deformation and similar yield strains compared to currently used stent materials and was chosen in this work.

Table 1 Summary of materials commonly used for additive manufacturing of metals and overview of observed mechanical properties in an as-built state and after post-processing.

| Material | Treatment | E (GPa) | UTS (MPa) | $\varepsilon_f$ (%) | Source |
|---|---|---|---|---|---|
| CoCr | As Built | 218 ± 19 | 1312 ± 15 | 11 ± 1.02 | [19] |
| CoCr | Heat Treated | 242 ± 40 | 1272 ± 116 | 9.1 ± 1.9 | [19] |
| SS316L | As Built | 536.4±4 | 668.4 ± 5 | 24.7 ± 2 | [20] |
| Ti-6Al-4V | As Built | 48.1 ± 2.3 | 903 ± 22.2 | 10.6 ± 1.6 | [21] |
| Ti-6Al-4V | Heat Treated | 118.8 ± | 988 ± 2 | 9.5 ± 2 | [21] |

The application of these design rules is intended to increase the printability of stent designs. The work presents an example of such a design printed from CoCr and includes an analysis of stent morphology, surface finish and results of electropolishing to improve surface finish. Finazzi *et al.* in 2019 [18] provides an extension of the previous work by presenting designs for bifurcations and investigating the expansion behaviour of the previously shown stents. Finazzi *et al.* in 2020 [14] contains details of this expansion behaviour investigation. A 170% diameter increase was achieved with an 8-bar pressurized balloon. This paper also includes further detail on the use of electropolishing as a method to improve surface finish and decrease the stent strut size below the geometric limits of the manufacturing process through material removal.

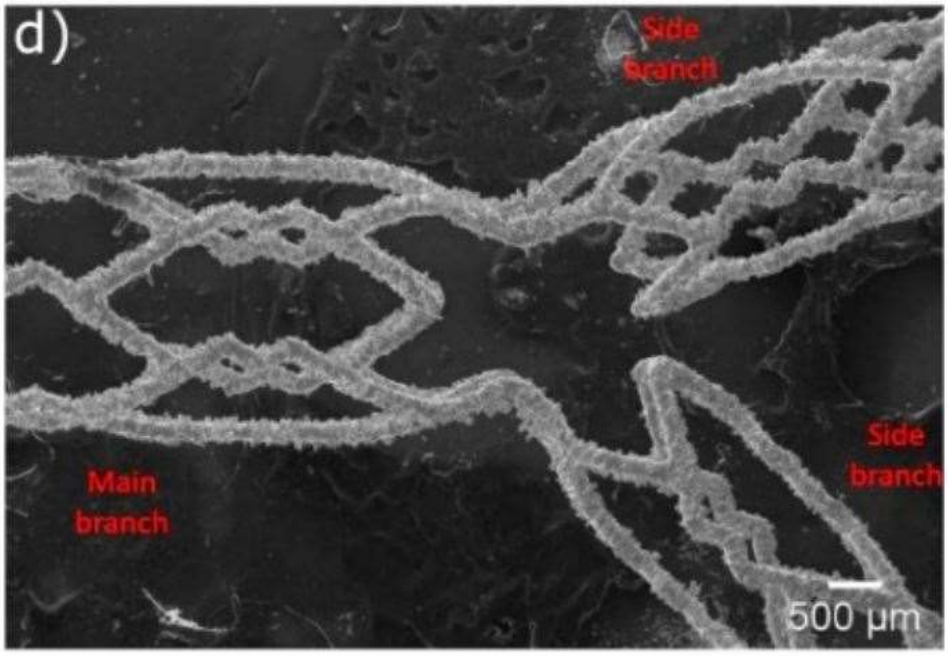


Figure 3 AM stent design for bifurcations presented by [18]

The surface morphology of AM parts has a large influence on mechanical properties, specifically defects caused by AM processes. Wiesent *et al.* [22] attempted to account for this within computational models investigating the effect of heat treatment and electropolishing on SS316L stents. The heat treatment employed in this work consisted of holding devices at a temperature of 1050 ºC for a period of 1 hour and subsequent cooling to ambient temperature inside the furnace. CT data was used to create detailed models of the stent surface before and after post-processing. These were then used in FE models which were fitted to experimental data of mechanical testing to provide insight into stent properties during expansion and compression. The work provides a discussion on methods of accounting for geometrical irregularities. This work also noted the computational expense of using CT data in models and the potential to account for these defects using stochastic methods which may be more computationally efficient.

Omar *et al.* [15] investigated the use of hot isostatic pressing (HIP) and polishing as post-processing techniques for CoCr AM stents where the mechanical and microstructural properties were analysed. HIP is a method of reducing internal porosity and thus increasing the density of AM parts, this is achieved by exposing and holding parts at high temperatures under high pressures. HIP was shown to lead to a 10% increase in stiffness and electropolishing led to an improvement in surface finishing, noting that further investigation is needed concerning fatigue analysis to ascertain the potential service life of AM stents. Langi *et al.* [16] approached stent design with additive manufacturing from a different perspective whereby AM was used to produce the tubing used for stent micro-machining. The microstructure, surface roughness and hardness of SS316L tubing produced with AM were investigated and compared to a typical commercial stent. This study highlights differences in surface roughness and microstructure that require optimization to produce AM stents comparable to contemporary commercial devices.

To increase design freedom associated with AM stents, Grad *et al.* [23] investigated several support design structures that were removed through a combination of mechanical blasting and electropolishing. Through an evaluation of the surface finish and geometry, this work proposed an optimized support geometry to be removed with a combination of sandblasting and electropolishing. This study showed the feasibility of realizing open cell designs, expanding the design freedom of AM stents. Maffia *et al.* [9] presented early results of open cell and variable diameter NiTi AM stents, see Figure 4. This work provided an overview of the effects of process parameters on porosity, surface roughness and transformation

temperatures of singular struts printed vertically. The open cell designs were realized by inserting a small cell gap in the design between the stacked stent crowns as seen in Figure 4. These cell gaps prevent or reduce material fusion between ends of the crowns and any residual material is removed using ultrasonic cleaning.

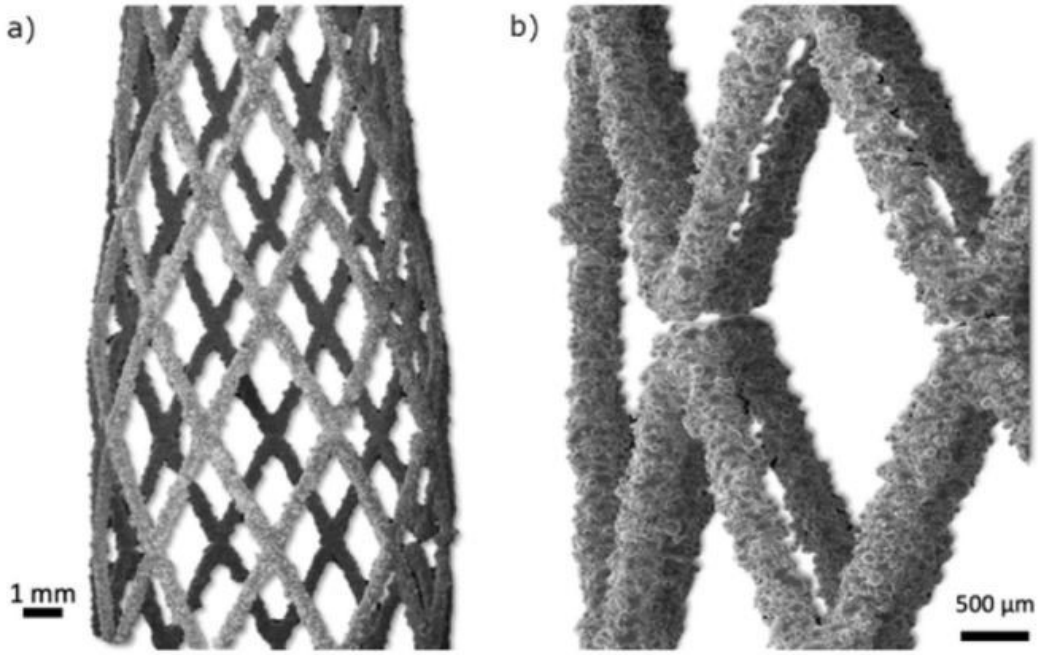


Figure 4 Varied diameter open cell NiTi stent presented by [9]

Previous work on AM metal stents showed promise as a method of fabricating patient-specific stents and realizing novel designs. These include those with a varied diameter or stent thickness with the potential to develop optimized stents for paediatric patients. There are several aspects of the manufacturing process that require optimization. Including, post-processing to achieve a controlled surface finish, material removal and support removal and, gaps in the literature where the mechanical properties of AM and commercial stents are compared. One of the aims of this thesis is to address this knowledge gap.

## 2.2 Post Processing of AM Components

Chemical etching is a common subtractive manufacturing technique, commonly referred to as chemical milling, utilized in the aerospace industry during the manufacture of titanium components since the middle of the 20th century. This technique is favoured over traditional fabrication methods as titanium is relatively difficult to machine due to its thermal properties [24]. It is also commonly used to remove the outer α-case layer present in investment cast titanium, this microstructure has a propensity for crack initiation and propagation [25].

Chemical etching has seen increased use as a post-processing technique for AM titanium lattices to improve the surface finish of the internal struts to realize mechanical efficiency and fatigue property benefits. As outlined by Balyakin [26], titanium is generally etched in a solution of hydrofluoric acid (HF) and nitric acid (HNO3). The reaction of HF and titanium is given as shown in Equation 1.

$$2\,\mathrm{Ti} + 6\mathrm{HF} \rightarrow 2\mathrm{TiF_3} + 3\,\mathrm{H_2} \qquad (1)$$

This reaction produces titanium trifluoride and hydrogen gas. The use of HF alone results in a slow etching process and the production of hydrogen gas can cause hydrogen embrittlement due to the propensity of titanium to pick up hydrogen atoms. To mitigate these factors nitric acid is added to produce the following reaction in Equation 2.

$$\mathrm{Ti} + 6\mathrm{HF} + 4\mathrm{HNO_3} \rightarrow \mathrm{H_2\,TiF_6} + 4\,\mathrm{NO_2} + 4\mathrm{H_2O} \qquad (2)$$

Producing hexafluorotitanic acid, nitrogen dioxide and water, and most importantly not producing hydrogen gas.

As outlined by Lhuissier *et al.* [27], AM metal components typically have surface defects. These are characterized by Type I and Type II defects. Type I defects are characterized by powder particles that have not fully melted and become stuck to the surface of the part. Type II defects consist of a plate-pile-like tacking defect as a by-product of the layer-by-layer manufacturing process, illustrations and images of these defects are seen in Figure 5.

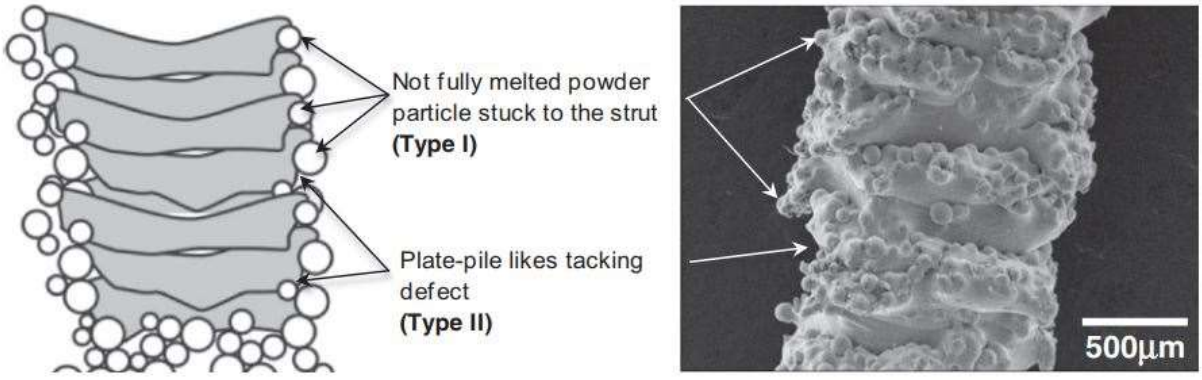


Figure 5 Illustration and microscopy images of typical defects found on AM metal components, from [27]

These defects can be removed with chemical etching. Lhussier *et al.* [27] displayed the temporal evolution of the defect dissolution process; Type I defects are quickly dissolved and Type II become smoother over time as seen in Figure 6.

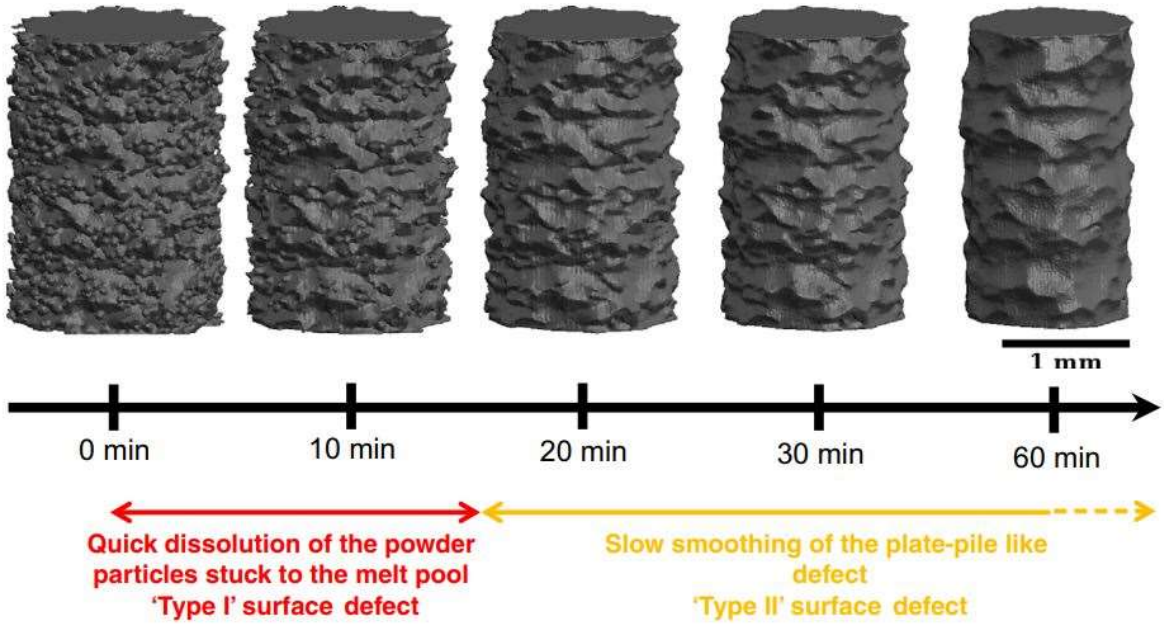


Figure 6 CT data illustrating temporal evolution of etching process and its effects on surface defects, from [27]

Pyka *et al.* [28] conducted a study using a design of experiments (DOE) technique to assess the interactive and individual effects of chemical etching duration and concentration on surface roughness. The work determined that solution concentration had the greatest influence on surface finish. The work of Persenot *et al.* [29] similarly assessed the influence of etching time but investigated its effects on fatigue properties. Here a 60% increase in fatigue endurance at $10^7$ cycles compared to as-built samples with fresh powder and a corresponding decrease in surface roughness was seen. This increased fatigue life with increased etchant concentration may be due to the removal of surface defects which can act as sites for crack initiation and subsequent failure. More recently Bezuidenhout *et al.* in 2020 [30] undertook a study where the HF concentration was varied between 1, 2 and 4M and kept the HNO3 concentration constant, investigating its effects on fatigue life and surface roughness. The study noted that higher concentrations led to a greater mass removal rate and improved surface finish with results illustrated in Figure 7. But this work notes that the process efficiency reduces much faster with higher concentrations due to depletion of the etchant. Increased concentrations also led to increased fatigue strength relative to as-built

conditions. No statistically significant difference was seen between the fatigue strength of samples etched in 2 and 4M HF solutions. Formanoir *et al.* [31] evaluated the effectiveness of chemical etching as a post-processing technique by investigating its effect on the relative stiffness of printed lattice structures. This is defined as the ratio of a linear elastic stiffness calculated from compressive testing divided by the Young's modulus of fully dense titanium. This study found etching decreased surface roughness and increased the relative stiffness of the component, thus leading to increased mechanical efficiency.

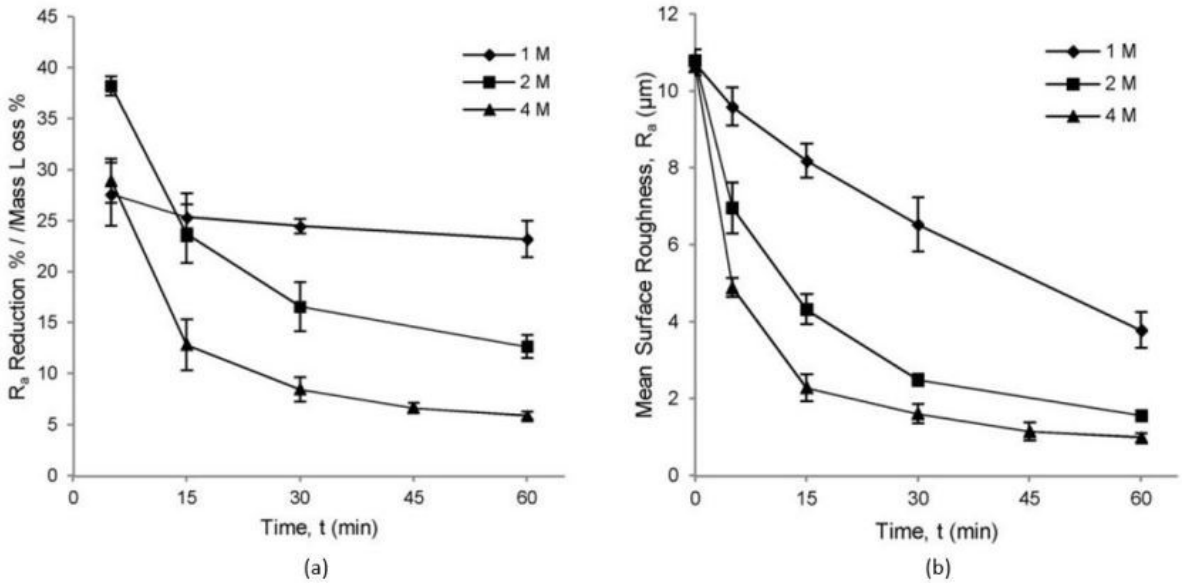


Figure 7 Reduction in mean surface roughness $R_a$ (a) and process efficiency concerning $R_a$ reduction and mass lost percentages (b) for AM titanium specimens presented in [30]

Some studies have considered chemical etching in combination with other post-processing techniques such as mechanical blasting, machining, and HIP and, investigated their effects on surface roughness and fatigue performance. Ahmadi *et al.* [32] considered the effects of sand blasting, heat treatment, HIP and chemical etching on fatigue life. The use of heat treatment alone was not seen to increase fatigue life. The authors noted that sandblasting effectively removed Type I powder particle defects and can induce compressive stresses which are attributed to increased fatigue life. This study indicates that there is a need to conduct a more thorough study on the effects of sandblasting parameters to fully understand its effects. The paper proposed a combination of HIP, sandblasting, and a light chemical etching to achieve optimal fatigue performance improvements. Similarly, Karami *et al.* [33] investigated the same post-processing techniques and their effects on quasi-static mechanical properties and fatigue endurance. This study again proposed the same

combination of post-processing techniques as Ahmadi *et al.* [32] to improve fatigue life. Sun *et al.* [34] utilized HIP, chemical etching, and standard and precision machining as methods to improve surface finish and fatigue performance. Standard machining consisted of 0.5 mm thickness removal and the precision machining consisted of 2.5 mm thickness removal. The main result of this study concluded that the surface finish improvements had a greater impact on fatigue life than HIP alone. The greatest endurance was seen where HIP and precision machining were utilized, the results are summarized in Figure 8.

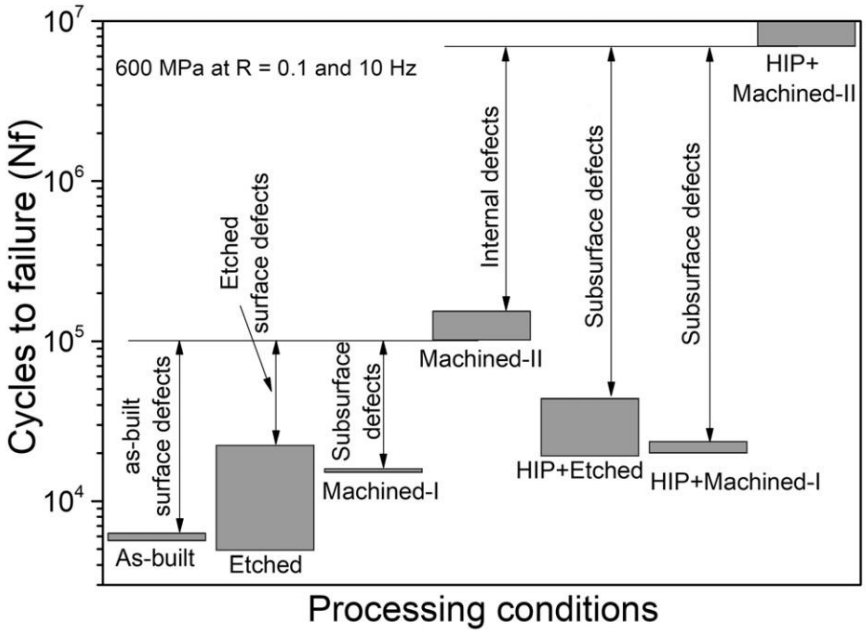


Figure 8 Illustration of influence of various post-processing methods on fatigue cycles to failure, from [34]

Previous work has shown the feasibility of using chemical etching as a post-processing technique to improve mechanical, fatigue, and surface properties of AM components. Specifically in the context of lattice structures, which are comprised of struts at similar geometric scales to commercial stents and thus may apply to AM stents. Within this research, the feasibility of using post-processing techniques will be investigated. A primary focus will be placed on developing an etching solution and protocol for support removal, material removal and controlled surface roughness improvement. In addition to chemical etching, the use of sandblasting for the same purposes will be investigated.

## 2.3 Stent Design

### 2.3.1 Evolution of Stent Design

Innovations in angioplasty and other related catheter interventions in the 20th century such as the Dotter technique and Gruentzig's balloon [35] revolutionized the treatment of atherosclerosis through the provision of a viable alternative treatment to surgical methods to treat obstructive vascular diseases. In 1963 Charles Dotter unintentionally recanalized the right iliac artery while passing a catheter through an occlusion for an aortogram [35]. Upon recognizing the potential he began to conduct cadaveric studies and in 1964 the first intentional procedure was conducted on an 82-year-old patient suffering from gangrene due to stenosis of the popliteal artery who refused amputation [36]. Figure 9 and Figure 10 illustrate the successful results of this procedure.

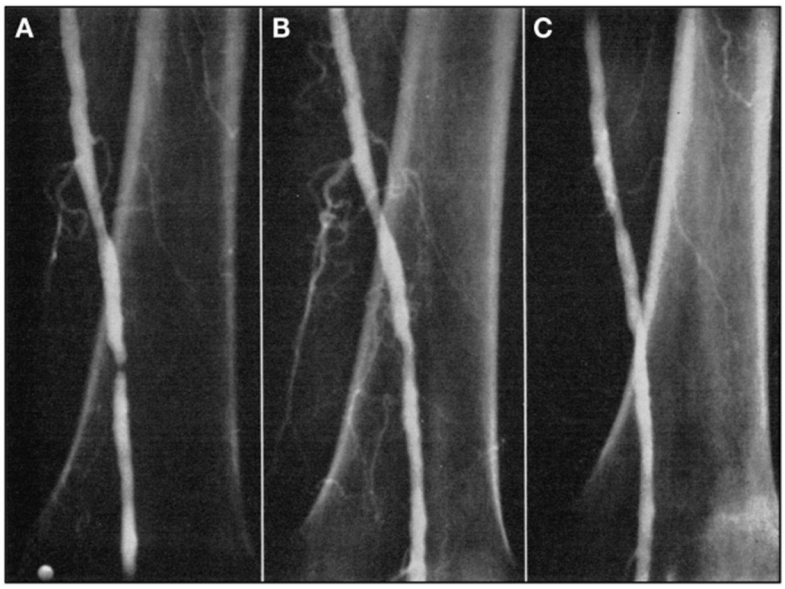


Figure 9 Medical imaging of before and after case reported in [36] where (a) is before luminal expansion, (b) is immediately after dilation and (c) is three weeks after dilation

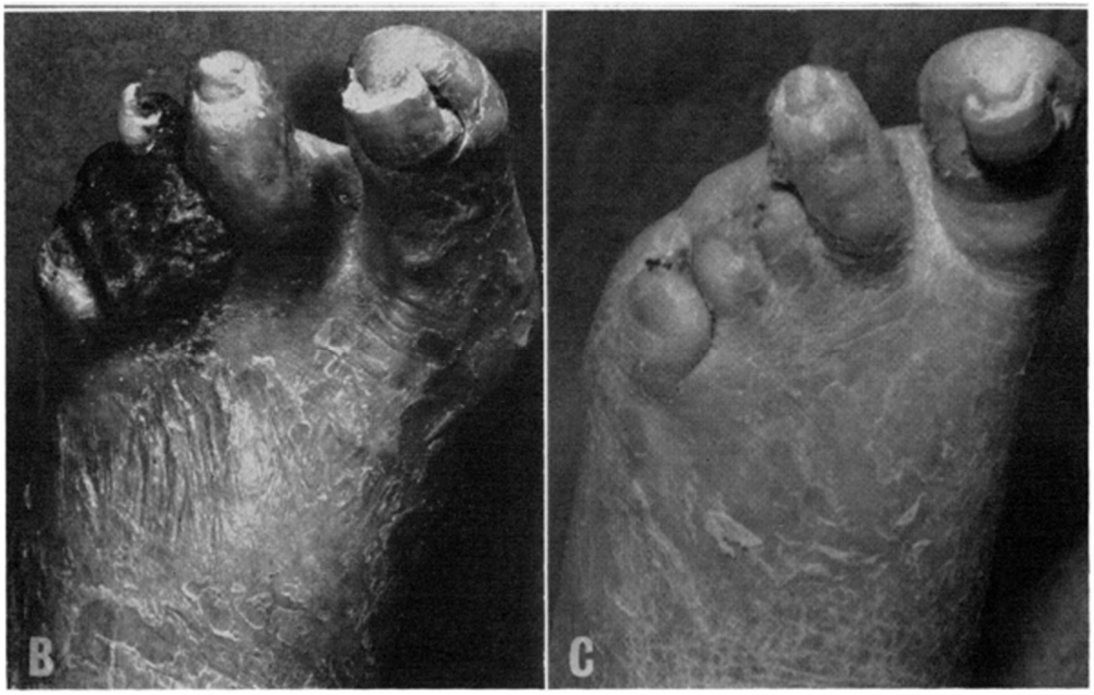


Figure 10 Photographs of patient's affected foot described in [36] with objective improvement where (a) is 1 week and (b) is 5 months after the procedure

In 1969 Dotter began experimentation with the placement of tubular prostheses in canine subjects with the concept displayed in Figure 11. The use of plastic tubing and stainless steel coil springs for this purpose acted as one of the precursors for modern-day stents [37], [38]. This procedure involved percutaneous placement of a catheter with a guide wire, this was guided across the intended narrowing site and withdrawal of the system left the graft in place within the narrowing.

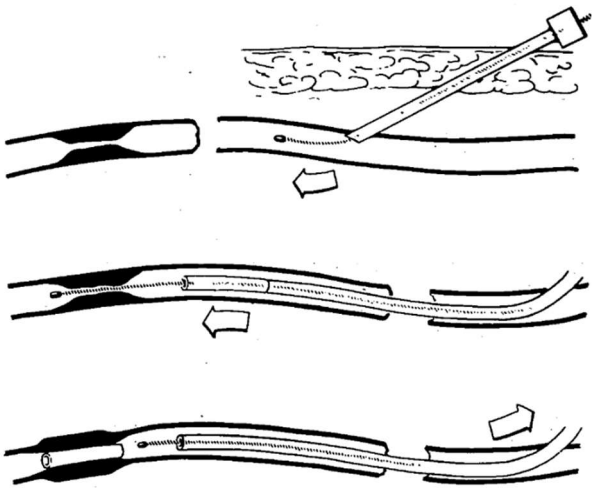

Figure 11 Technique for percutaneous, transluminal placement of tubular prosthesis within blood vessels [37]

By 1983, Dotter had begun experimenting with nitinol coil grafts where the shape memory effect was utilized to induce an outward radial force in the graft. This was achieved by the introduction of saline at 60 °C into the catheter system [39]. Radiography images of the placement and post-procedure evaluation of this device are shown in Figure 12.

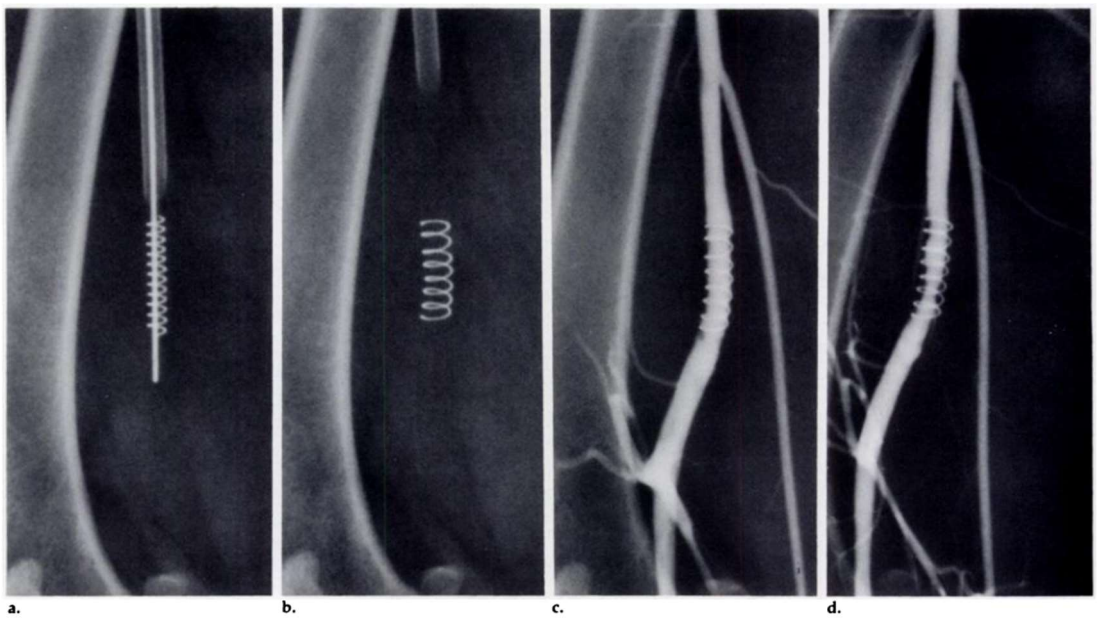


Figure 12 Nitinol coil stent placement, (a) compact stent, (b) expanded state, (c) five days and (d) one-month post-procedure [39]

By the 1980s several stent design methodologies were developed, this review will focus on the operating principles of balloon-expandable and self-expanding stents.

### 2.3.2 Balloon Expandable Stents

Balloon expandable stents were pioneered by Palmaz in the mid-1980s [40] as a method to overcome the prevalence of restenosis after vascular balloon dilation. The initial designs consisted of continuous woven stainless steel wire to form intraluminal grafts where 150 um and 200 um wire diameters were used [40]. An illustration of these initial designs is shown in Figure 13. Later devices were fabricated by electrical discharge machining (EDM) and in current times, laser cut processing of metallic tubes [41]. Thiebes *et al*. [5] conducted a comparative study of the mechanical properties of braided and laser cut stents. This study concluded that laser-cut stents experience less elongation during crimping and had greater radial resistance than braided contemporary stents. Common modern stent design characteristics include thinner struts, this has an influence on deliverability by enabling a lower crimped profile and may reduce disturbance to blood flow, this translates to lower

rates of restenosis post implantation. Open cell designs have also increased in popularity since the first generation of balloon expandable stents, this influences device flexibility and deliverability [42].

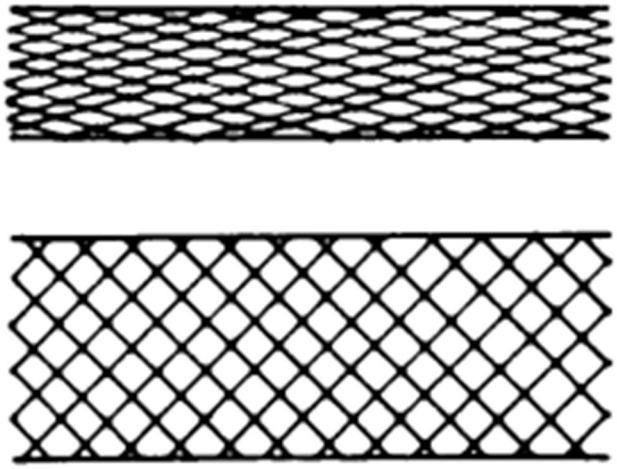

Figure 13 Illustration of early woven stainless steel stents developed by [40]

These devices rely on controlled diametrical expansion via balloon dilation whereby a target diameter is reached, the device is deformed beyond the elastic limit of the material and plastic deformation occurs [43]. This concept is illustrated in the stress-strain curve of a typical elastic-plastic material in Figure 14. The balloon catheter is expanded elastically until the material goes beyond its yield strength where plastic deformation begins to occur. When the target device diameter is reached the balloon is deflated and the device retains an increase in lumen due to plastic strain. Some diameters decrease upon deflation occurs due to elastic recoil where elastic energy within the material is recovered.

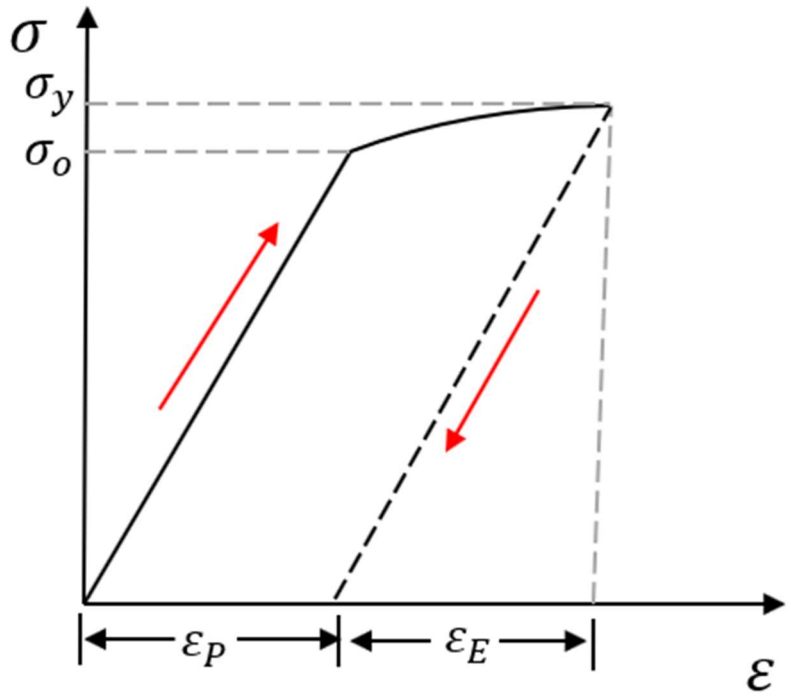


Figure 14 Stress-strain curve showing loading and unloading behaviour of elastic-plastic material. Where $\epsilon_E$ and $\epsilon_P$ are plastic and elastic strain respectively. $\sigma_o$ and $\sigma_y$ denote the initial and updated yield strength

To gain an increased understanding of the mechanical behaviour of these devices, the hoop stress and diameter evolution of a typical stent and target vessel during a balloon expandable stent deployment are represented in Figure 15. Beginning with the stent, the hoop stress increases as the balloon inflates until it reaches the maximum inflation at point b. From here the balloon is deflated, and the hoop stress in the stent goes to zero with a small decrease in diameter due to elastic recoil. The vessel meets the stent at point a, inducing hoop stress due to expansion and reaches its maximum value at point b of maximum inflation. Upon balloon deflation, the reduction in stent diameter due to elastic recoil leads to a decrease in diameter and equilibrium of hoop stress between the stent and the vessel as seen at point c.

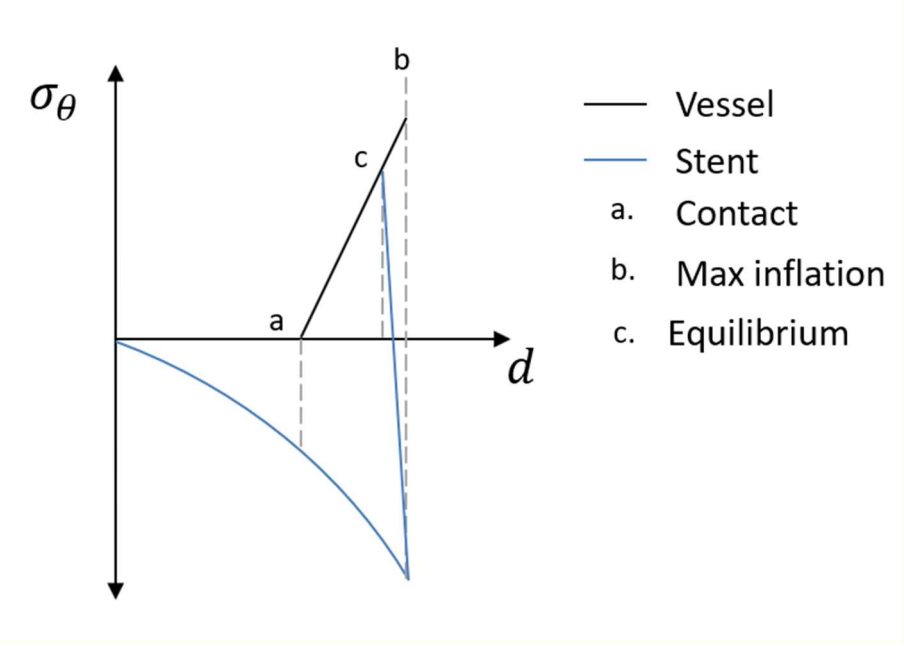


Figure 15 Hoop stress $\sigma_\theta$ and diameter $d$ evolution over typical deployment of balloon expandable stent. Adapted from [44]

### 2.3.3 Self-Expanding Stents

Early self-expanding stent designs also consisted of woven stainless steel [45]. These devices were fabricated in an "expanded" state, for implantation the device is elastically compressed radially under a sheath and placed on a catheter. Upon device placement, the sheath is removed which allows the stent to dilate due to elastic radial recoil. Self-expanding stents are designed to have a larger diameter than the target vessel, the dilation exerts a radial force on the target vessel leading to expansion.

Improvements in manufacturing in the 1990s saw seamless nitinol tubing become available, enabling stents to be laser cut from this material [46]. Initial studies showed the material properties of super-elasticity and shape memory enabled efficient device placement with minimal foreshortening and good lateral stability [47]. Figure 16 illustrates the typical stress-strain behaviour of a super-elastic material during a loading and unloading cycle. The material initially deforms linearly in the austenite phase until reaching a plateau stress where transformation to a detwinned martensite micro-structure begins. The material can deform in this transformation phase while inducing little or no stress. When the material is completely transformed to detwinned martensite linear elastic-like behaviour begins again. Upon unloading the material can recover from large deformations without residual strain and an inverse transformation back to the initial austenite microstructure occurs.

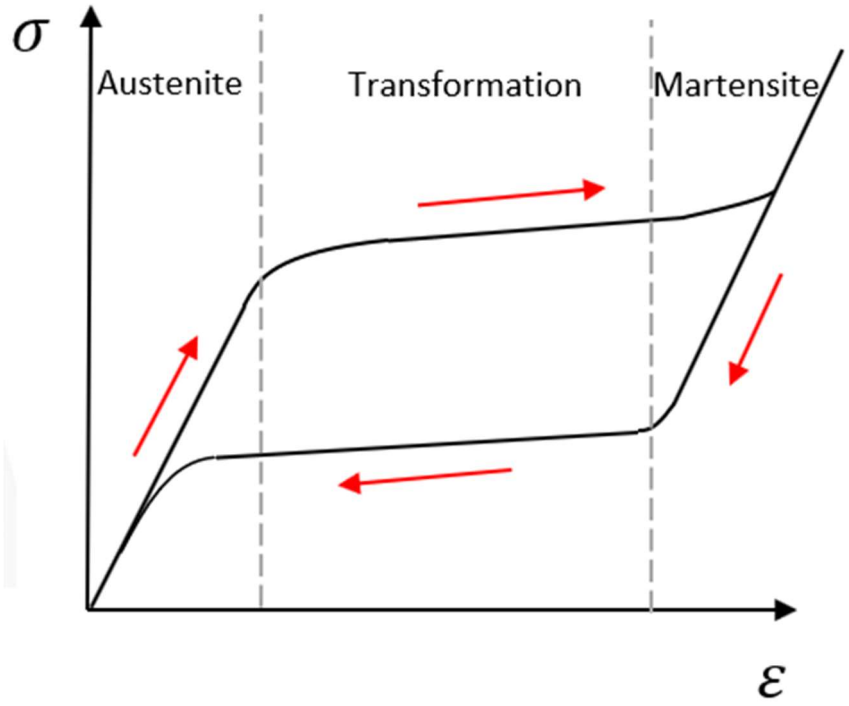


Figure 16 Stress-strain curve showing loading and unloading behaviour of super-elastic material

The delivery of self-expandable stents in some contexts require balloon inflation, this may be to increase the diameter of the stent itself post deployment or, prior to deployment balloon expansion of the vessel may be required to prepare the affected vessel for stent implantation.

In a similar manner to balloon expandable stents, the mechanical behaviour of self-expanding stents is considered in Figure 17. The hoop stress and diameter evolution of a typical stent and target vessel for a self-expanding stent deployment are shown. Beginning with the stent, as the delivery sheath is removed the stent begins to expand radially with a corresponding decrease in hoop stress until reaching equilibrium at point b. From here the stent is inflated with a balloon leading to a further decrease of hoop stress until reaching maximum deflation at point c. From here the balloon is deflated and elastic recoil causes the stent diameter to decrease, and the hoop stress reaches equilibrium with the target vessel. The hoop stress and diameter evolution of the target vessel are similar to that seen for the balloon expandable stents, coming into contact with the stent at point a. The vessel diameter and hoop stress increase until reaching maximum inflation at point d. The elastic recoil of the stent then leads to a slight decrease in diameter and hoop stress.

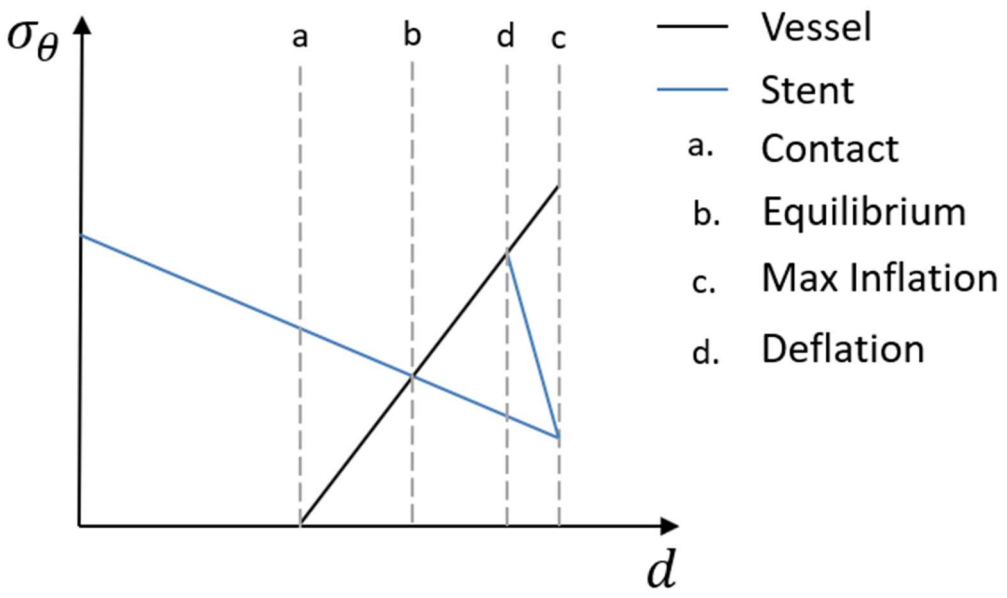


Figure 17 Hoop stress $\sigma_\theta$ and diameter $d$ evolution over typical deployment of a self-expanding stent. Adapted from [44]

## 2.4 Stent Characterisation

### 2.4.1 Radial Stiffness and Strength

This characterises the ability of a device to resist collapse under long or short-term external loads, thus preventing vessel recoil and lumen loss post-implantation. ISO 25539-2:2019 [48] defines patency as the ability to maintain an open lumen and specifies that this can be quantified with two variants of crush resistance tests. Firstly, the crush resistance test with a radially applied load determines the force required to cause clinically relevant buckling or a diameter reduction of 50%. ASTM F3067-14 [49] provides a guide to conducting these tests and an overview of radial loading measures and interpretation of results. A schematic of a typical test setup is shown in Figure 18. A crush resistance test with parallel plates allows for the quantification of device resistance to permanent deformation, a setup of this test is shown in Figure 19.

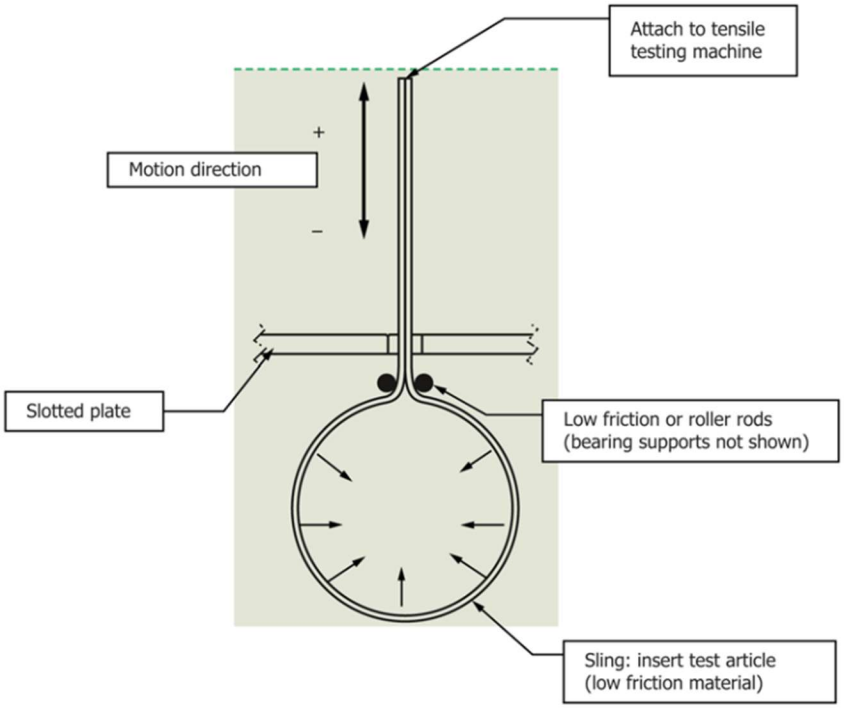


Figure 18 Radial loading crush resistance test setup from [49]

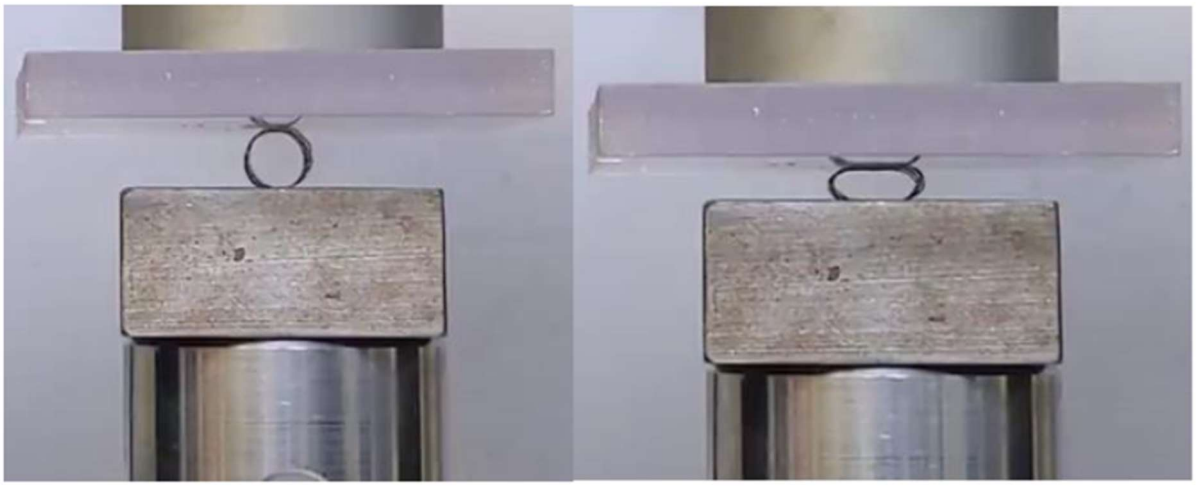

Figure 19 Parallel plate crush resistance test setup from [17]

The FDA recommends reporting radial stiffness as the change in diameter as a function of uniform externally applied pressure and radial strength as the pressure a stent experiences irrecoverable deformation [50]. ISO 25539-2 also outlines a test method for local compression whereby the ability to locally resist radial deformation is quantified. A point load is applied until a 50% reduction in diameter is achieved, and the minimum diameter of the device is measured after this test is reported.

### 2.4.2 Elastic Radial Recoil

The minimization of elastic recoil is desirable as it minimizes the required diameter a stent must be inflated to achieve a desired relaxed diameter. A high recoil stent may lead to excessive expansion of the target vessel resulting in tissue damage and poor patient outcomes. Recoil is noted as influenced by the material and geometrical properties of a given stent design [51]. ASTM-F2079 provides a standard test method to quantify intrinsic elastic recoil of balloon expandable stents by comparing inflated and final device diameters. Radial recoil, $\mathrm{Recoil_R}$, is quantified by Equation 3.

$$\mathrm{Recoil_R} = 1 - \frac{\mathrm{D_F}}{\mathrm{D_{INF}}} \tag{3}$$

Where $\mathrm{D_F}$ is the final diameter and $\mathrm{D_{INF}}$ is the inflation diameter Barragan *et al.* [52] conducted a comparative analysis of 22 commercially available stents including platinum, steel, tantalum and nitinol devices. Yamamoto *et al.* [53] similarly conducted a comparable study. The results indicated that flexible coil stents offered lower radial strength and thus higher elastic recoil than slotted tube or laser cut stents.

### 2.4.3 Flexibility

In both delivery and expansion, a high level of flexibility is desirable [54]. In the context of delivery, flexibility is required to reach the target vessel without tissue damage and similarly where a stent is expanded in a tortuous vessel high flexibility is required to prevent vessel straightening which can cause vessel damage or device failure [50]. The FDA recommends determining the smallest radius of curvature a device can withstand without kinking and providing evidence that it will recover to the original size and shape after testing. This can be conducted by placing devices within a silicon tube and bending them around a mandrel at 180º as seen in the work of Brandt-Wunderlich *et al*. [55].

ISO 25539-2 provides guidance on quantifying device flexibility. This is achieved by determining the minimum radius a deployed device can be flexed without kinking, reducing in diameter by over 50% or without recovery to its original shape and provides guidance on two test methods to determine this. ASTM F2606 [56] provides an in-depth standard guide to quantifying flexibility with a three-point bend test such as that seen in Figure 20. This test method is used to obtain force vs. deflection or mid-span bending moment vs. curvature

curves to assess flexibility and provides guidance on the test protocol, recommended span lengths and interpretation of results.

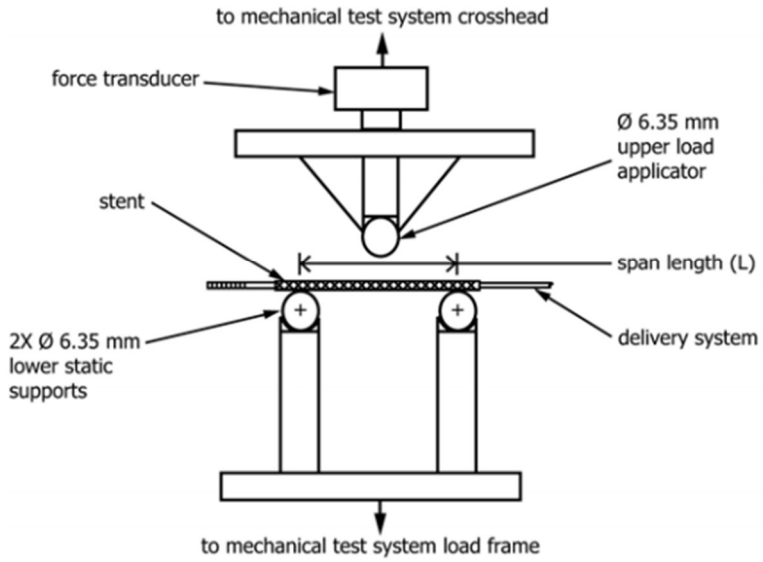


Figure 20 Schematic of three-point bend test to determine flexibility from [56]

### 2.4.4 Longitudinal Recoil

Foreshortening or longitudinal recoil post-dilation can induce shear forces on the vessel wall and lead to tissue injury through the tearing of endothelial cells during expansion [54]. Wiktor *et al.* [57] notes there has been an increased interest in longitudinal recoil and deformation behaviour. Designs with thinner struts, open cell designs and the use of more flexible materials such as Co-Cr. These developments have increased deliverability but may be associated with a decrease in longitudinal strength. Longitudinal recoil, $\mathrm{Recoil_L}$, is quantified by Equation 4.

$$\mathrm{Recoil_L} = 1 - \frac{\mathrm{L_{LOAD}}}{\mathrm{L_{UNLOAD}}} \tag{4}$$

Where $\mathrm{L_{Load}}$ and $\mathrm{L_{UNLAOD}}$ are the device lengths at maximum balloon expansion and upon balloon deflation respectively.

Leibundgut *et al.* [58] conducted longitudinal compression testing with a parallel plate setup similar to that shown in Figure 19 for the radial crush test. This method is quantitative but it has been argued that it does not reflect longitudinal deformation modes seen in clinical practice [57]. Ormiston *et al.* [59] proposed a method of assessing longitudinal strength with local point compression to simulate asymmetrically applied longitudinal forces with the

potential to distort stents as seen in clinical practice. An example of such a test setup is shown in Figure 21.

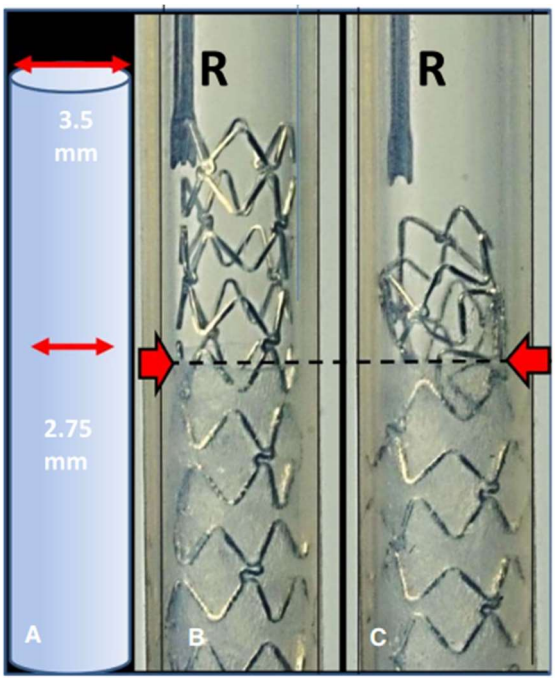


Figure 21 Setup and procedure of longitudinal point compression testing from [59]

The FDA recommends reporting the length decrease between catheter conditions and deployment diameters up to the maximum labelled diameter and points to ASTM F2081 [60] for additional guidance on this topic. This standard states device lengths should be measured with non-contact methods such as with a laser micrometre. Clinically useful devices have reported length changes during expansion in the range of 0 to 20%.

### 2.4.5 Contact Surface Area

Devices are required to provide optimal vessel coverage to prevent prolapse of tissue between stent struts but this should be balanced to prevent a thrombotic response due to the body's immune response to the stent [54]. The FDA recommends reporting the percent surface area, $A_S$ for the smallest and largest nominal deployment diameters and is calculated with Equation 5.

$$A_S = \frac{A_C}{A_{FC}} \tag{5}$$

Where $A_C$ is the area in contact with the vessel and $A_{FC}$ is the equivalent full cylinder area of the stent. The FDA and ISO 25539-2 point to ASTM F2081 [60] for additional guidance

on this topic and recommends the determination of contact area through suitable image analysis, dimension measurements or by CAD software. The standard states that clinically useful devices have contact surface area percentages between 7% and 20%.

## 2.5 Operational Characteristics of Stents

### 2.5.1 Crossing Profile

This characteristic is defined as the maximum outer diameter of the stent on the delivery system, this influences the operational ability of a given delivery system to move through the vascular system [50]. The minimization of the crossing profile can prevent flow disturbances within the vascular system and can be achieved through the reduction of strut thickness [54]. ISO 25539-2 outlines a test method for determining the crossing profile, provides guidance on accuracy requirements and points to ASTM F2081 [60] for additional guidance on this topic. This standard notes that clinically useful devices have crossing profiles of less than 1mm and up to 2mm.

### 2.5.2 Trackability

This is defined as a measure of the ability of a device to move through a tortuous vessel and is dependent on shaft flexibility, friction with the surrounding environment and axial stiffness [54]. The FDA recommends assessing this by performing delivery simulations within *in vitro* fixtures that mimic physiological and anatomical conditions with a tortuous path and aqueous environment. ASTM F2394 [61] provides a standard guide for measuring the securement of stents on the delivery system and provides details of a test tracking fixture to assess this and trackability. A schematic of a test tracking fixture from this standard is provided in Figure 22.

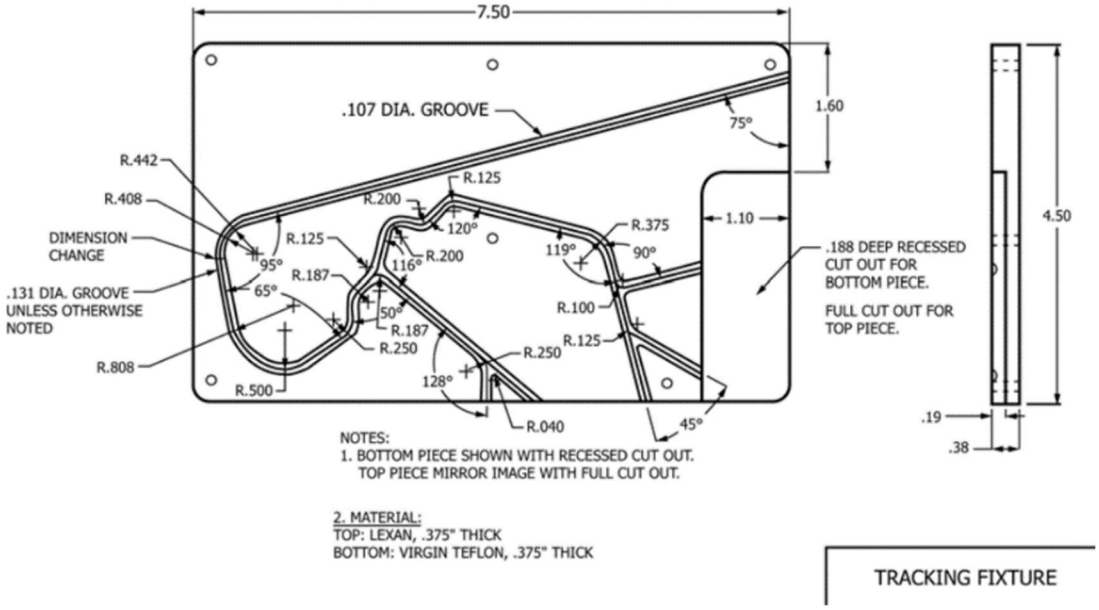


Figure 22 Schematic of test tracking fixture from [62]

### 2.5.3 Withdrawal

The ability to withdraw a stent delivery system safely and consistently must be considered with a focus on hazards such as improper balloon deflation, balloon winging, stent dislodgement or device damage [48]. Similar to trackability, the FDA recommends that this be assessed with the fixture described in ASTM F2394 and seen in Figure 22.

### 2.5.4 Sterilization

ISO 25539-2 states stents and stent systems are required to have a sterilization assurance level of $10^{-6}$. Sterilization of stent products are of utmost importance to patient outcomes as infections related to bare metal stent have high mortality rates, noted as up to 30% [63]. The ISO points to three methods of sterilization, by use of ethylene oxide to which ISO 11135-1 [64] applies, by moist heat to which ISO 17665-1 [65] applies and by radiation where ISO 11137-1 [66] applies. The aforementioned standards were developed in conjunction with the Association for the Advancement of Medical Instrumentation (AAMI).

## 2.6 Material Characteristics of Stents

### 2.6.1 Radiopacity

This refers to the visibility of a device when using angiographic or radiographic imaging. High visibility enables accurate placement of the device and patient to follow-up assessment

[50]. The FDA recommends providing a qualitative or quantitative measure of visibility on real-time and plane film x-ray. These images may be from animal implants or *in vitro* implants. ASTM F640 [67] provides a standard test method for determining radiopacity for medical use.

### 2.6.2 Biocompatibility

Materials used in stents and their respective delivery systems must not induce an adverse response from the body such as thrombosis or restenosis, an example of each of these is shown in Figure 23.

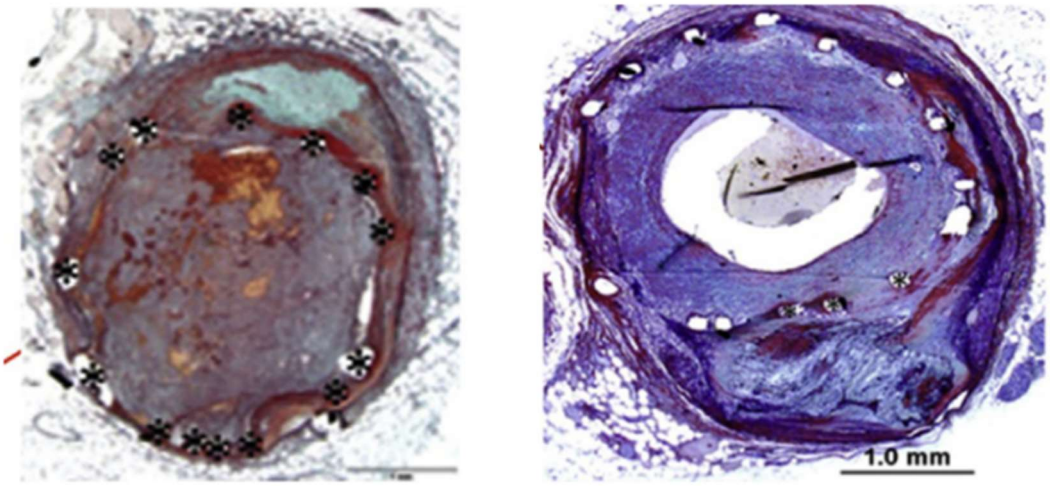


Figure 23 Medical imaging of (a) typical thrombosis and (b) restenosis from [68]

The FDA recommends the determination of all patient contact materials biocompatibility and points to ISO 10993 [69] to identify suitable tests that should be considered. Furthermore, the FDA recommends several tests for the stent material including cytotoxicity, sensitization, irritation, and carcinogenicity testing.

### 2.6.3 Corrosion Resistance

The presence of corrosion can contribute to or lead to premature device failure, by-products of corrosion may also have associated toxicity or induce adverse tissue responses [50]. The FDA recommends the assessment of devices for fretting, pitting and crevice and, galvanic corrosion modes.

Fretting corrosion can occur due to overlap of stent struts in clinical use, this can be tested within a tortuous phantom, where the use of a 15mm radius of curvature vessel and

accelerated wear testing for 10 year period is recommended [50]. An example of fretting corrosion wear is seen in Figure 24.

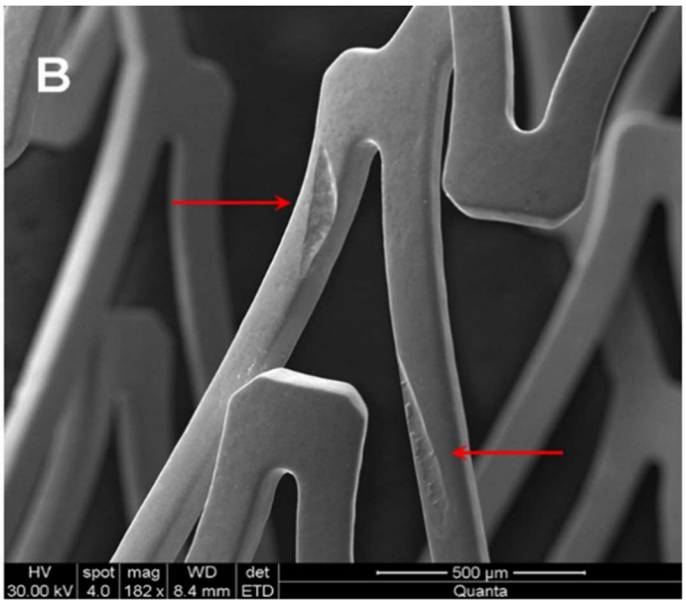


Figure 24 SEM image of typical fretting corrosion damage from [70]

Pitting and crevice corrosion can occur due to fatigue loading with the potential to reduce the service life of a stent. The FDA recommends quantifying corrosion susceptibility with cyclic potentiodynamic polarization measurements as described in ASTM F2129-19a [71]. A typical example of pitting and crevice corrosion is shown in Figure 25.

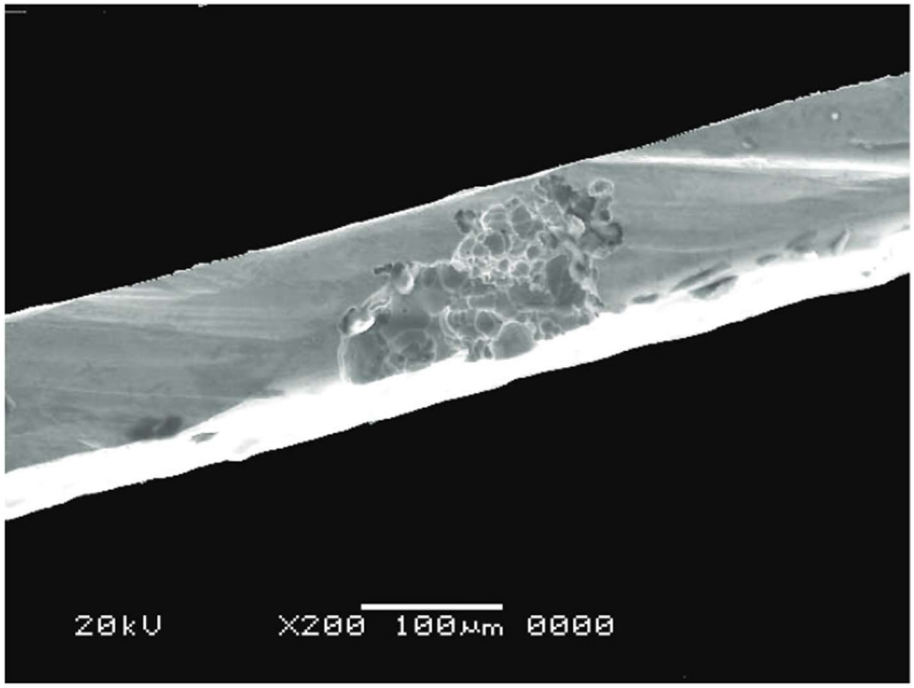


Figure 25 SEM image of typical pitting and crevice corrosion damage from [72]

Galvanic corrosion may occur where stents contain multiple materials, for example, a stent may have added marker bands for radiopacity [50]. Where it is envisioned that stent struts will overlap or where two materials are in contact the FDA recommends testing for susceptibility to galvanic corrosion according to ASTM G71 [73]. A test method from this standard is adapted for medical devices in the previously mentioned ASTM F2129-19a.

### 2.6.4 Fatigue Properties

Blood flow induces cyclic stresses on stents which can lead to fatigue failure. It is recommended devices are designed to withstand 10 years of service life equivalent to 380 million cycles [54]. Stent failure may cause loss of radial support of the stented vessel, focal restenosis or perforation of the vessel by a broken stent strut [50]. The FDA recommends fatigue analysis combined with finite element (FE) modelling and accelerated durability testing to quantify device durability. The output of FE modelling is recommended to be presented as a Goodman diagram where mean and alternating stresses simulating physiological conditions are used to determine a fatigue safety factor of a device. A typical Goodman diagram is seen in Figure 26.

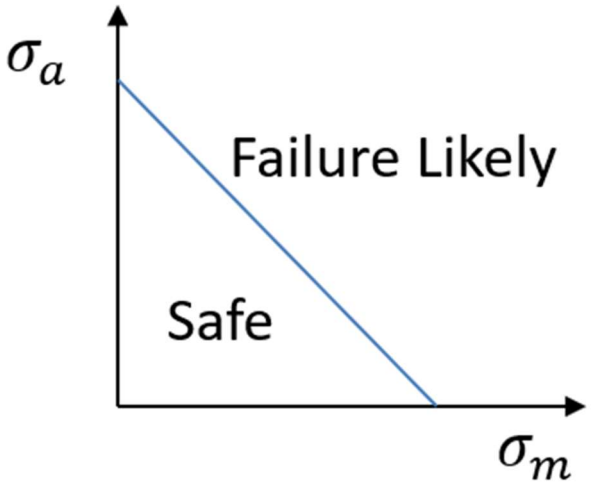


Figure 26 Goodman diagram used for fatigue analysis where $\sigma_a$ and $\sigma_m$ are alternating and mean stresses respectively

The use of accelerated durability testing is recommended to validate fatigue analysis results and can identify device conditions that may contribute to failure that are not present in the computational analysis [50]. ASTM F3211 [74] provides guidance on conducting fatigue to fracture tests to characterize device durability whereby hyper-physiological high-cycle fatigue testing is used. Relevant test methodologies to assess *in vitro* axial, bending and torsional durability is provided by ASTM F2942-19 [75]. Axial durability is assessed through tension and compression cycling, bending durability can be assessed through a columnar buckling fixture or bending on a mandrel. Figure 27 displays a typical columnar buckling fixture setup. Torsional durability can be assessed through cyclic loading where a stent is fixed at one and the other end rotated similar to that described in [76]. Figure 28 displays a typical schematic of this test.

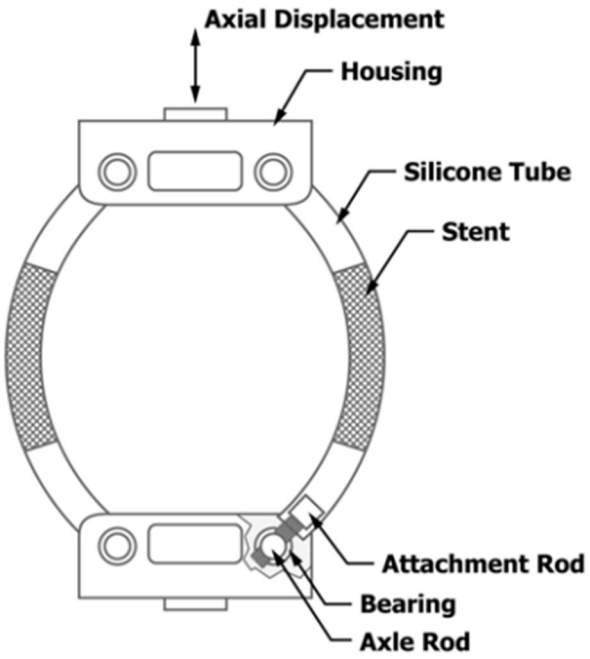


Figure 27 Columnar buckling setup to assess axial durability of stents from [77]

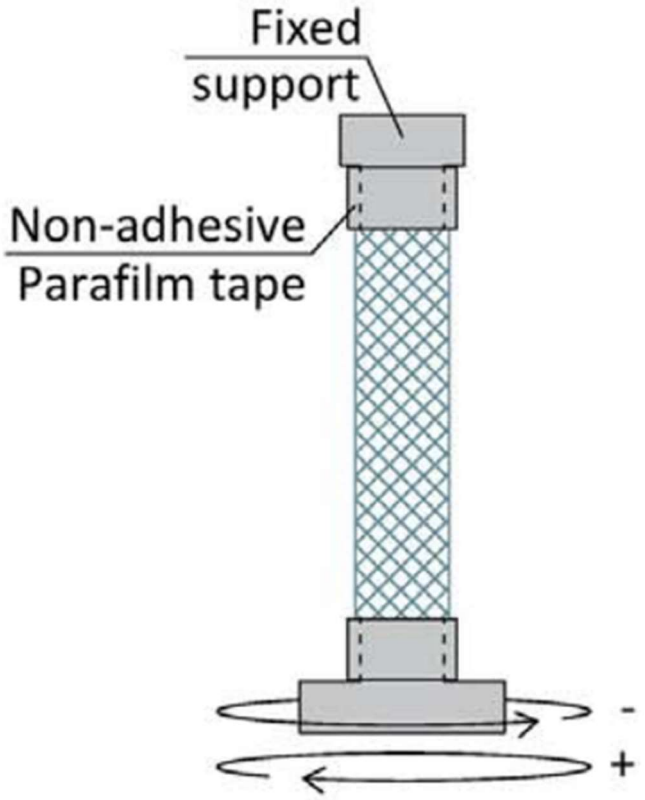


Figure 28 Schematic of torsion durability test of a stent from [76]

ASTM F2477 [78] provides a standard test method for *in vitro* pulsatile durability testing of stents intending to assess device failure due to typical cyclic blood vessel diametric distension. The standard provides guidance on two physiological pressure test methods. One where a fixed fluid volume is cyclically injected within a mock vessel and a strain-controlled method where clinically relevant changes in diameter are reproduced in the mock vessel. It should be noted that for all test methods described, it is recommended that they are conducted in a mock vessel that emulates *in vitro* conditions, i.e. a phantom with an aqueous environment at 37 °C.

### 2.6.5 MRI Compatibility

MRI safety and compatibility is an important consideration as MRI patients with stents can cause movement or heating of implants, this has the potential to cause displacement or tissue damage. The device may also lead to artefacts rendering in MR images which can result in misleading or uninterpretable results. The ASTM provide several test methods for determining the MRI compatibility of a medical device.

ASTM F2052-15 [79] provides a standard test method for determining magnetically induced displacement force on medical devices in the MR environment. This is measured by calculating the deflection angle of a device in a magnetic field. The device of interest is suspended on a test fixture with a schematic of the forces and parameters of interest shown in Figure 29.

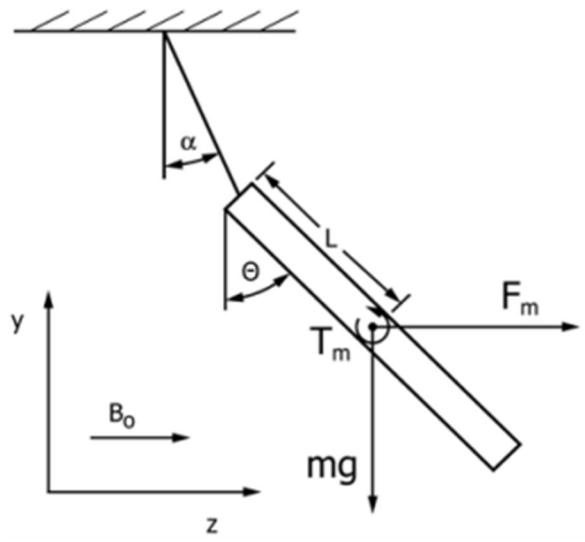


Figure 29 Schematic of the test device in magnetic field for measurement of magnetic induced displacement force, from [79]

ASTM F2213-06 [80] provides a standard test method to determine magnetically induced torque on medical devices in the MR environment. This can be quantified by placing the device of interest on a torsion spring or pulley torque apparatus as described in the test method. An example of the torsion spring test device is shown in Figure 30.

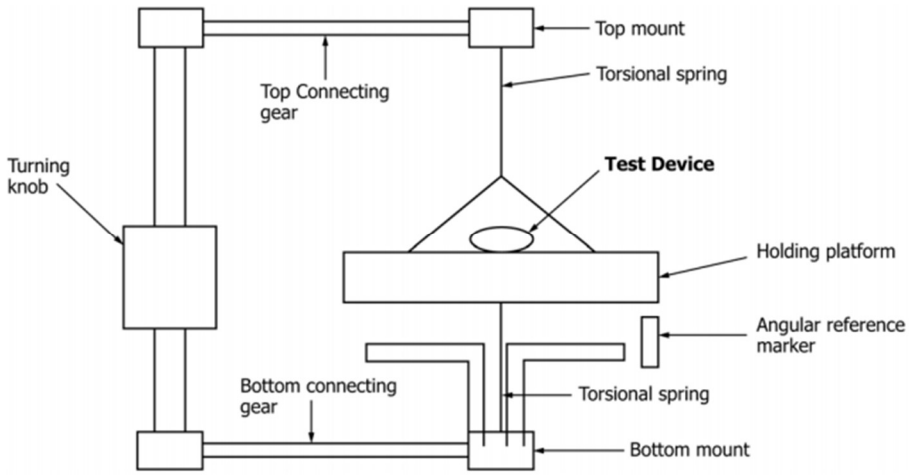


Figure 30 Schematic of the test device in magnetic field for measurement of magnetic induced torque, from [80]

ASTM F2182-11a [81] provides a test method for determining radio frequency-induced heating of passive implants due to MRI. This is quantified by placing a device of interest in a gelled-saline phantom and placing temperature probes along the length of the device. The temperature evolution over time is then measured in an MR environment.

ASTM F2119-07 [82] provides a test method for the evaluation of MR image artefacts due to passive implants. The test method provides information on recommended MR parameters, image set requirements and quantifying an artefact size.

## 2.7 Stent Mechanical Characterization Studies

A review of commercial stent mechanical characterization studies was conducted to gather data for direct comparison with AM stents and to gain an understanding of the experimental methods typically used to conduct testing. Some papers mentioned in the previous section are discussed in more detail.

Yamamoto *et al.* in 1999 [53] studied the effect of stent design on elastic recoil by investigating differences between the flexible coil, slotted tube and locking stent designs. The elastic recoil was evaluated using intravascular ultrasound imaging within an *in vitro* model of circumferential compression, stents were placed within a latex balloon which was

deflated to negative pressure. From here change in cross-sectional area and mean lumen diameter was recorded. This study, as previously stated, showed that coil stents showed the least amount of radial strength.

Dyet *et al.* in 2000 [83] investigated radial strength, flexibility, radio-opacity and trackability of a variety of commercial stents. Radial strength was determined using the method outlined by [84] where a cylindrical contact compresses the stent imposing an eccentric deformation on the stent wall. Flexibility was quantified by measuring the force required per degree of flexion. Trackability was measured by assessing the delivery system over angles of 90° and 60°. Radio-opacity was measured by comparing the stent against an aluminium test piece. The work concluded that balloon expandable stents exhibited greater radial strength and radio-opacity than self-expanding stents which were generally more flexible and had better trackability.

Barragan *et al.* [52] as previously mentioned, conducted a comparative analysis on 22 commercial stents whereby elastic recoil was measured post expansion with and without exterior stress at several time intervals up to 2 hours. The external pressure was applied using a flexible tube on the outside of the stents and recoil was measured with a contact-free 3D optical gauging system. This study showed that external pressure had little effect on recoil and in both conditions, recoil remained relatively stable over time. It also notes differences between tubular and coil stents in their recoil behaviour. Garica *et al.* [85] carried out a study on in vivo stent recoil by implanting several stents into porcine arteries, using continuous ultrasound cross-sectional area, and, minimum and maximum diameters were measured at peak inflation and immediately after inflation. The results of this study showed a greater acute area recoil for modular stents versus slotted tube stents. It is also of note that this study was conducted on healthy porcine arteries and thus is the best-case scenario for elastic recoil.

Schmidt *et al.* [86] presented a comparison of mechanical properties of nitinol self-expanding and stainless steel balloon-expandable stents by comparing their flexural stiffness, radial strength and change in length due to expansion. Flexural stiffness was measured using a cantilever beam setup whereby stents were held at one end and a load is to the other. Radial strength was quantified using a test chamber where pressure is applied to a polymeric tube covering the stent. Change in length due to expansion was measured with microscopy. The results of this study showed low flexural stiffness and collapse

pressure for the self-expanding stents and noted a change in length behaviour is determined by the stent design geometry and not by material properties. The work of Wang *et al.* [87] aimed to characterize the mechanical response of a typical aortic stent to internal and external pressure by measuring axial and radial deformation. Internal and external pressures were applied using a polymer bag with a pressure system with digital cameras to track deformation. This work proposed an analytical model based on slender rod theory to model the relationship between pressure and stent radius.

Isayama *et al.* [88] conducted radial and flexural stiffness on several biliary self-expanding stents. radial stiffness was measured with a cylindrical radial force testing machine as seen in Figure 31. Flexural stiffness was measured by quantifying the force required to bend the stent to 60° at several distances from the end of the stent. This study provides a good range of comparative data. Hirdes *et al.* [89] conducted a similar study on self-expanding oesophagal stents. Johnston *et al.* [90] investigated the radial behaviour of some self-expanding stents. Radial stiffness and outward radial force were measured using a hydrostatic pressure chamber and a mylar film device as seen in Figure 32. The results of this study showed longer stents had greater radial force and stiffness and, overlapping two stents increased these measures to values greater than the sum of the individual stents.

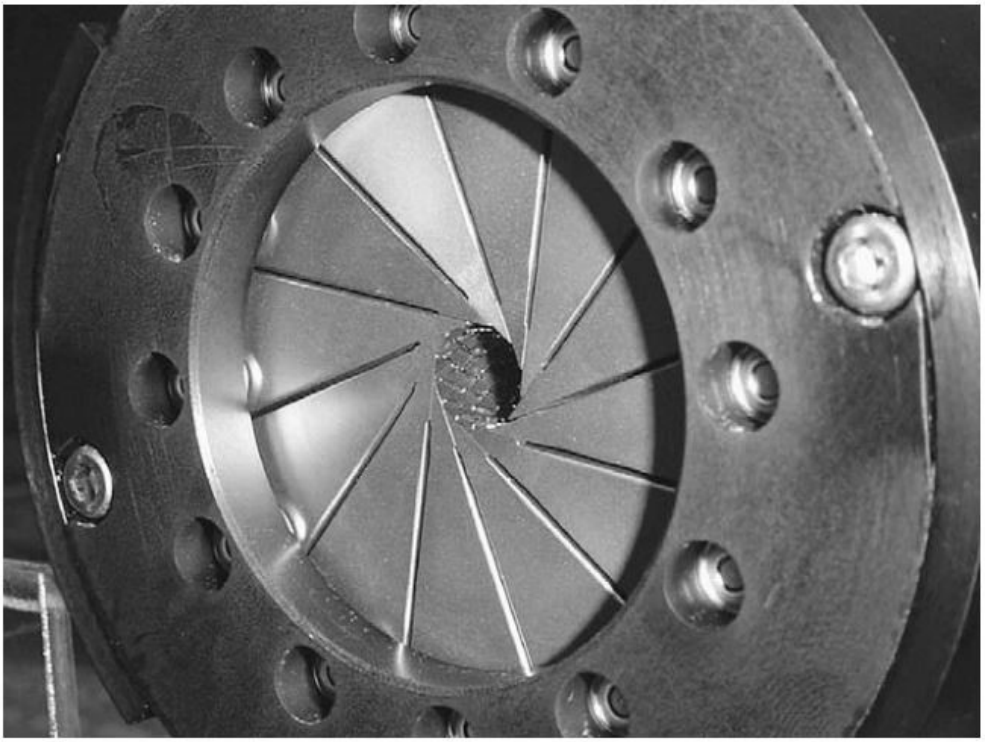

Figure 31 Cylindrical radial force test machine for stents, from [88]

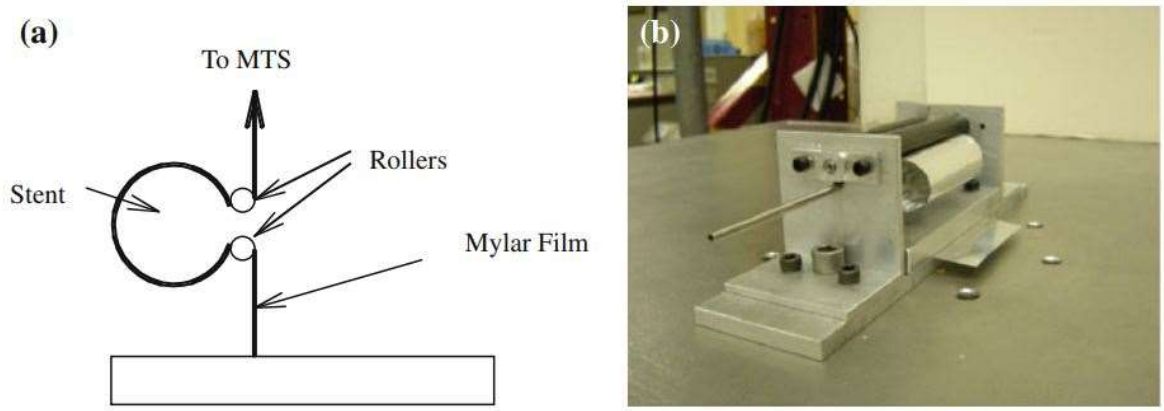


Figure 32 Mylar film radial testing device (a) schematic and (b) image of device, from [90]

## 2.8 Summary

Overall, this literature review has identified a number of knowledge gaps which this work intends to address. There is little comparison of commercial and AM stents in terms of mechanical and geometric properties in the literature. Similarly, there is little work in the literature quantifying the effects of post-processing techniques on the mechanical and operational properties of AM stents, this work aims to investigate this relationship with a parameter study.

Little work to date has shown the feasibility of producing AM stents with varied mechanical properties achieved through non-uniform strut thickness or diameter. Stents with these properties may be more optimal for the treatment of aortic coarctation by enabling lumen gain, where required, while ensuring minimal loading of non-diseased tissue and vessel straightening.

In summary, a more ideal AM stent design may require the following:

- Radial stiffness tunability
- Flexibility for delivery
- Open cell design for flexibility
- Ability to crimp and recover for deliverability
- Low surface roughness

The selection of these parameters of interest is based on the availability of data within the literature in the context of AM and commercial stents for comparison with the devices fabricated in this work.

# Chapter 3. Materials and Methods

## 3.1 Stent Design for AM

### 3.1.1 IntraStent Design

The Medtronic IntraStent is a peripheral and biliary stent commonly used in coarctation procedures. The stent is an open cell design laser cut from 316L stainless steel, with a 12 mm diameter and 200x250 um rectangular strut profile. In the context of the AM rules outlined by Demir *et al.*[18], it is not possible to manufacture this stent design. The stent contains overhangs and as a consequence of the open cell design, it is not a self-supporting structure.

To investigate the feasibility of recreating this device with AM, the geometry was adapted to enforce the self-supporting structure AM design rules. The strut dimensions were increased to 300x350 um to ensure the design was within the resolution of the printer and enable the use of post-processing to be used for material removal to achieve strut thicknesses similar to commercial stents. Additionally, 100x350 um support structures were added to the open cells with a view of removing them with post-processing and resulting in a self-support structure. Stents were designed at 15 mm in length for radial strength testing and post-processing optimization. 46 mm stents were also designed for flexibility testing.

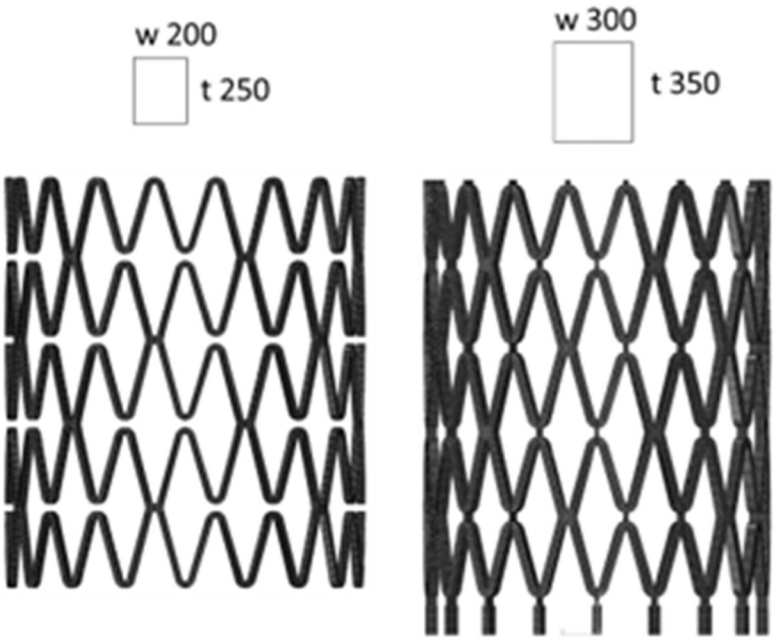


Figure 33 Intrastent (a) commercial design and (b) adapted design for AM with strut dimensions and profile.

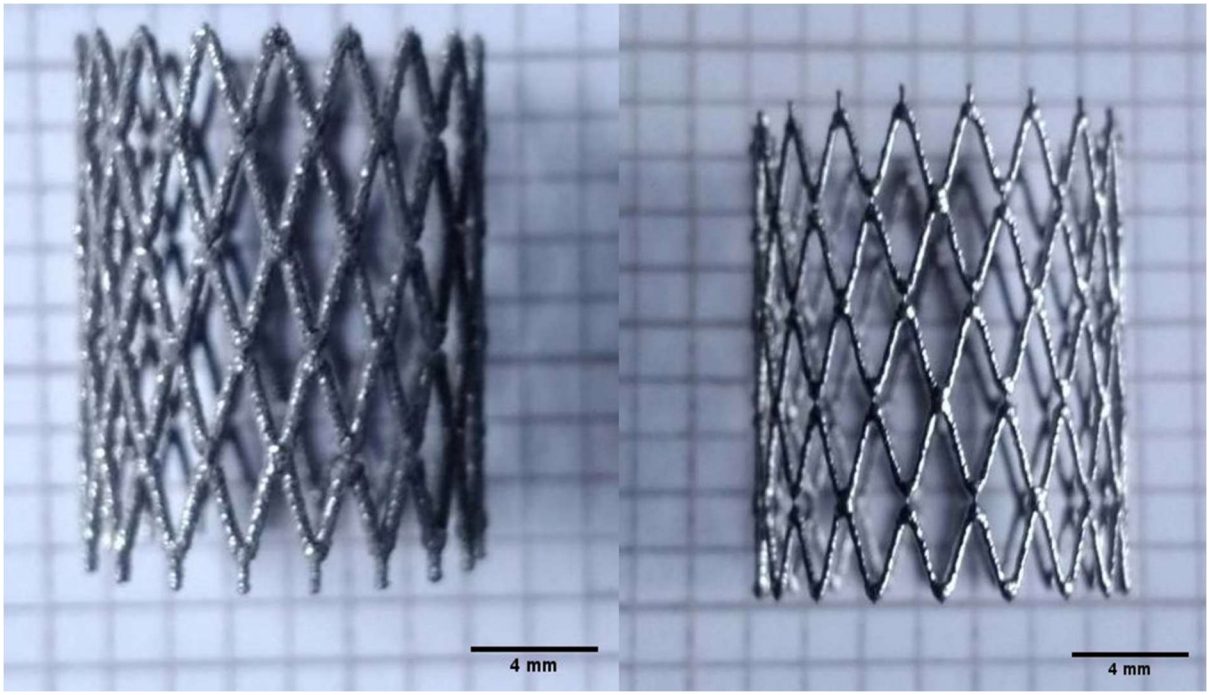


Figure 34 As built and post-processed AM IntraStent

### 3.1.2 Tapered Stent Design

To show the feasibility of using AM to achieve greater design freedom for stents, a modified tapered IntraStent was developed. A 25% taper in diameter was added, changing from 12 mm to 9 mm over the 19 mm length of the stent. This was achieved using the Flex tool in SolidWorks. Realizing this design with standard balloon expandable stent manufacturing techniques would require custom-sized tubing and complex laser cutting techniques. Using AM to fabricate this design offers increases in time efficiency and enables rapid prototyping of such designs.

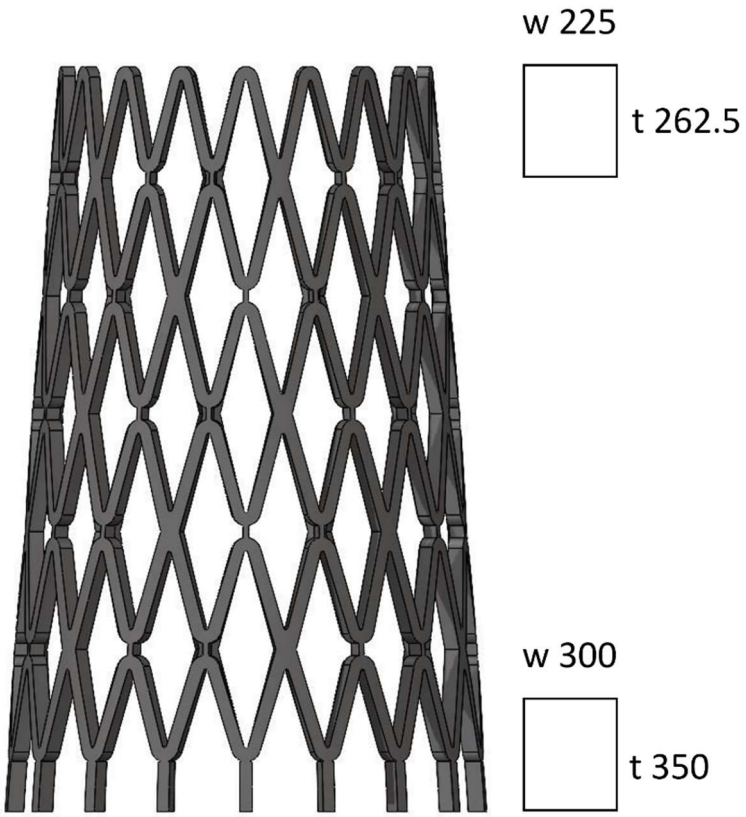


Figure 35 Modified tapered intrastent design with a 25% taper giving a change in diameter

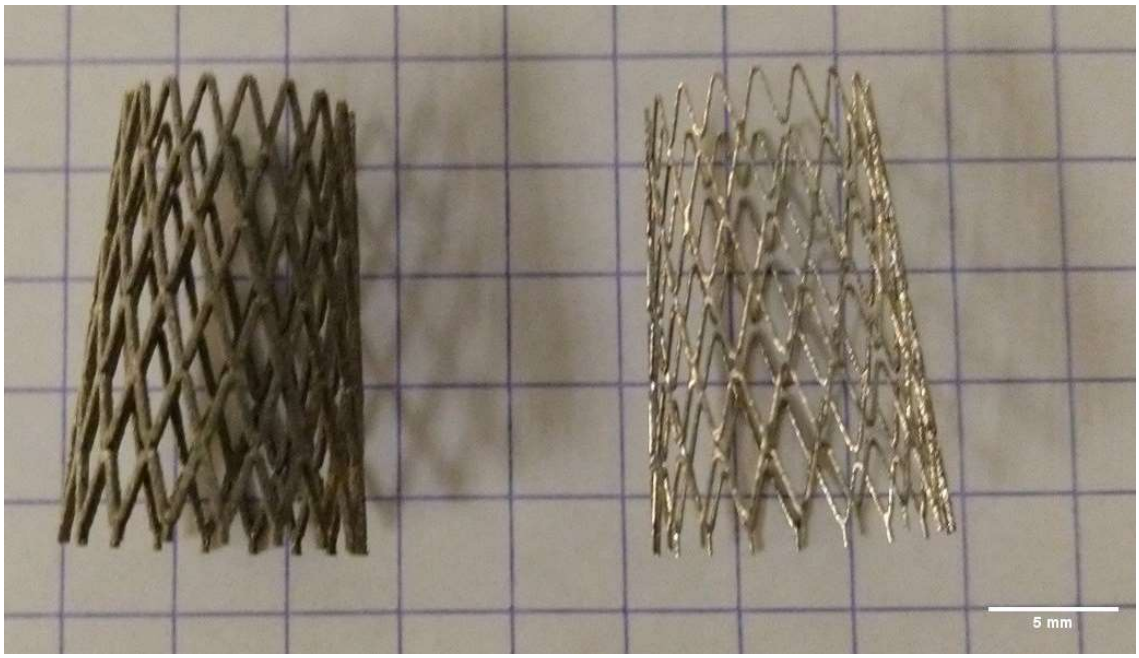


Figure 36 As built and post-processed tapered stent design

## 3.2 Commercial Stents & Balloon Expansion

For comparative analysis of radial strength and flexibility two commercial stents were balloon expanded and subjected to mechanical testing. A 10 mm diameter and 17 mm length stainless steel VALEO vascular stent (Becton, Dickinson and Company, United States), with a 200 um strut thickness, was used for radial strength comparison. Additionally, a 12 mm diameter and 36 mm length stainless steel IntraStent LD Max stent (Medtronic, United States) was used for flexibility comparison. Both stents were expanded to 10 mm diameter using a VALEO vascular stent balloon catheter inflated to 6 bar using a BasixCOMPAK inflation device (Merit Medical, United States). The devices were then allowed to recoil radially, and dimensions measured with a calliper.

## 3.3 Titanium Powder

The powder used was Ti-6Al-4V ELI (Grade 23) (Carpenter Additive, Cheshire, UK). The powder was spherical and produced by gas atomisation. Its size distribution was 22.5 – 47.2 um with an average size of 32.7 um. The chemical composition of this powder is given in Table 2.

Table 2 Chemical composition of Ti-6Al-4V powder

| **Element** | **N** | **C** | **H** | **Fe** | **O** | **Al** | **V** | **Ti** |
|---|---|---|---|---|---|---|---|---|
| Mass Fraction (%) | 0.01 | 0.01 | 0.0027 | 0.21 | 0.11 | 6.3 | 3.9 | Bal |

## 3.4 Laser Powder Bed Fusion

A ReaLizer Selective Laser Melting (SLM) 50 with a 100 W fibre laser was used to print the stent geometries from Ti-6Al-4V. The estimated beam diameter was in the range of 15-20 um. The processing chamber was filled with argon gas reaching an overpressure of 15 mbar. A circulation pump was used to maintain parallel flow to the powder bed and oxygen was maintained below 1.2%. A modulated continuous wave laser emission was used with an exposure time of 40 us and a point distance of 10 um. The laser current was maintained at 1463 mA for the outer boundary and 2800 mA for the inner hatching. A boundary-scan was executed first with parallel hatching scan lines with a hatch distance of 0.1 mm used internally. A layer thickness of 25 um was kept constant throughout the build. Magics 23.02 (Materialise, Leuven, Belgium) was used to prepare the models. RDesigner (DMG MORI, Bielefeld, Germany) was used for setting laser trajectories and ROperator (DMG MORI,

Bielefeld, Germany) was used for the machine preparation. A summary of machine parameters is presented in Table 3. Additionally, all devices were placed in an ultrasonic cleaner for 15 minutes after printing. This process removes any loose powder particles adhered to the stents.

Table 3 Summary of ReaLizer SLM 50 printing parameters

| Parameter | Quantity | Unit |
|---|---|---|
| **Outer Boundary** | | |
| Exposure Time | 40 | us |
| Point Distance | 10 | um |
| Laser Current | 1463 | mA |
| **Inner Boundary** | | |
| Exposure Time | 40 | us |
| Point Distance | 10 | um |
| Laser Current | 1463 | mA |
| **Hatch** | | |
| Exposure Time | 132 | us |
| Point Distance | 10 | um |
| Laser Current | 2825 | mA |
| Melting Trace Width | 0.14 | mm |
| Hatch Distance | 0.1 | mm |
| Hatch Offset | 0.08 | mm |
| Overlap | 0.04 | mm |
| Fill Lines Distance | 0.04 | mm |

## 3.5 Design of Experiments

To optimize the sand blasting and chemical etching times for stent post-processing a design of experiments (DoE) approach was used, namely the Latin Square Design method. Upper and lower bounds were identified for sandblasting and chemical etching times. For chemical etching, times between 5 minutes and 27.5 minutes at 2.5 minute intervals were chosen. Similarly, sandblasting times between 10 seconds and 120 seconds at 10 second intervals were chosen. This resulted in a grid from which experiment parameters were chosen using the Latin Square Design method. This method results in an experimental plan where each parameter is chosen only once in each row and column, in this case for each sandblasting and chemical etching time. Each experimental parameter set was repeated 3 times. This is illustrated in Figure 37.

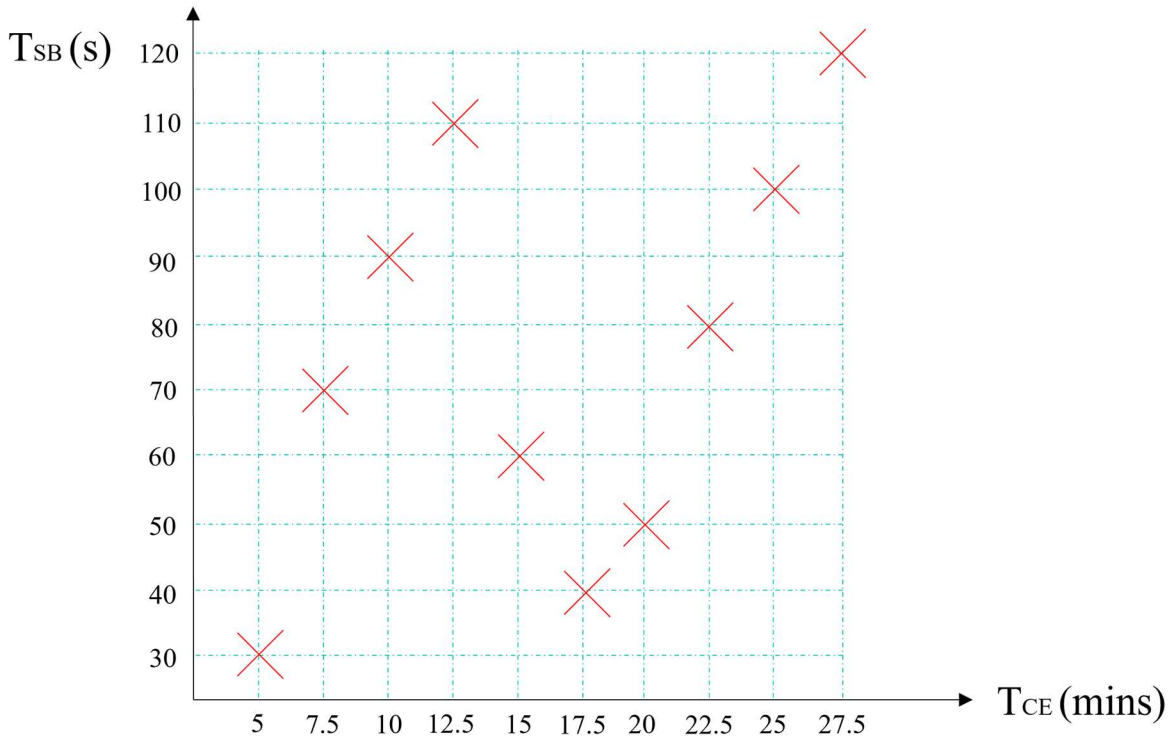


Figure 37 Latin Square Method DoE technique applied to sandblasting and chemical etching times, $T_{SB}$ and $T_{CE}$ respectively

## 3.6 Statistical Analysis

Statistical analysis was performed using GraphPad Prism 9 statistical software (GraphPad Software Inc) with the aim of investigating and quantifying statistically significant differences between as built and post-processed stents. To investigate statistically significant differences between the means of each group a Welch's t-test with a 95% confidence interval was applied. This test method assumes the means of the compared populations are normally distributed and is insensitive to equality of variance. The t-tests estimate with 95% confidence that there is a statistically significant difference between each of the stent groups. A sample size of 3 was selected for each experiment.

## 3.7 Microscopy Imaging

To quantify the strut thickness of the stents a Leica LM DM (Leica, Germany) stereoscopic microscope was used. Stents were imaged at 5 x magnification using a ZEISS Axiocam 208 colour microscope camera (Zeiss, Germany) in the ZEISS Efficient Navigation (ZEN) software (Zeiss, Germany). In this software, the measure tool was used to quantify the strut thickness 3 times for each strut analysed.

## 3.8 Scanning Electron Microscopy (SEM)

To qualitatively investigate surface roughness, Scanning Electron Microscopy (SEM) was conducted using a Zeiss ULTRA plus (Zeiss, Germany) system. All samples were imaged at an electron high tension (EHT) voltage of 10 kV with the Type II secondary electrons (SE2) detector. Due to the variance in device sizes, a variety of working distances and magnifications were used to produce sufficiently detailed images.

## 3.9 White Light Interferometry

White Light Interferometry (WLI) was used to assess the relative surface roughness of each of the stents to investigate differences between printed, sandblasted, and sandblasted and etched stents. Additionally, AM stents were compared to commercial devices with this method. A ProFilm 3D (Filmetrics, Inc., San Diego, CA.) optical profilometer was used and arithmetical average roughness for a given path, Ra, was used to compare surface quality. ISO 4288:1996 [91] recommends a roughness sampling length of 0.8 mm and a roughness evaluation length of 4 mm for Ra values greater than 0.1 um and less than or equal to 2 um, corresponding to the Ra range for the etched stents. Similarly, the ISO standard specifies a roughness sampling length of 2.5 mm and roughness evaluation length of 12.5 mm for Ra values greater than 2 um and less than or equal to 10 um, corresponding to the Ra range for the unetched stents. Due to limitations related to the length of the diagonal struts, it was not possible to attain this recommended sampling length. To mitigate this a consistent sample length of 600 um was used across all measured struts and in a similar fashion to [92] and the effect of the low-test length was neglected as the measurements were used comparatively. Ra is defined by Equation 6.

$$R_a = \frac{1}{\mathrm{L}} \int_0^L |Z(x)| dx \tag{6}$$

Where L is the evaluation length and Z(x) is the profile height function.

Images were obtained at 50 x magnification, giving a field of view of 0.4 x 0.34 mm. Two scans were taken with a back-scan length of 110 um and then stitched together with the provided profilometer software to achieve the prescribed sample length. The stitched images provided a 3D map of the surface topography, this was then processed within the software package to remove outliers whereby pixels with a slope above 60° were removed and invalid pixels were filled in. The line roughness tool was then used to calculate a Ra value along the

strut within the scan length. Additional microscopy images at 10 x and 50 x magnification were taken for further qualitative comparison of surface roughness and defect.

## 3.10 Sandblasting

A Guyson Formula F1200 blast cabinet was used for sandblasting stents. Brown aluminium oxide, FEPA F120 (120 um) grain blasting media was used at a pressure of 6 bar with a trigger-operated blasting gun in the process. A bespoke stent holding fixture was fabricated from aluminium to ensure the stent is allowed to rotate in a fixed position during blasting. This ensures the even and consistent processing of devices. An image of the fixture in situ is presented in Figure 38.

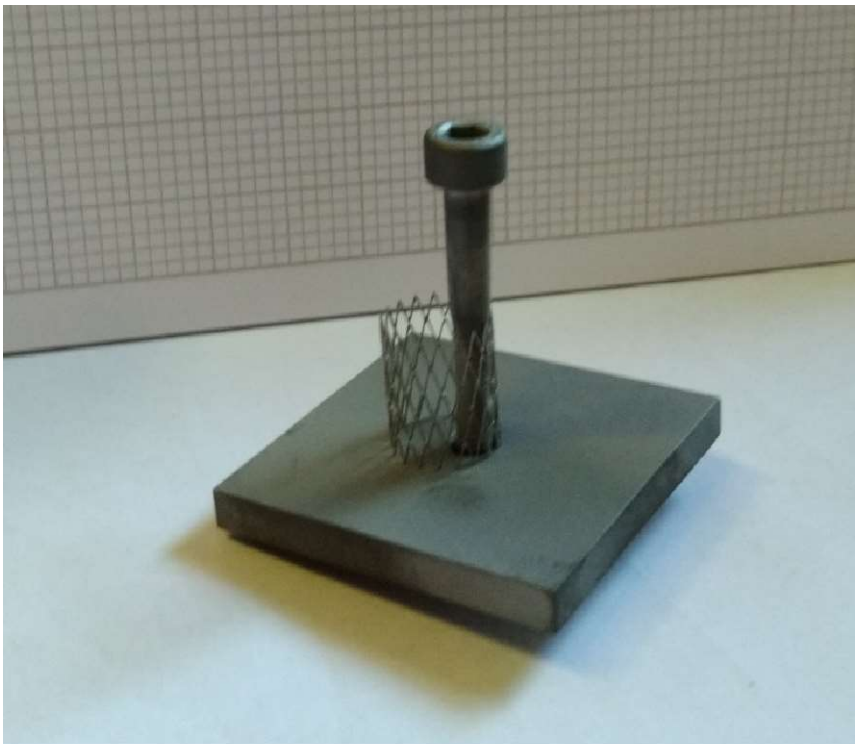

Figure 38 Sandblasting stent holding fixture

## 3.11 Chemical Etching

The titanium stents were etched using Kroll's etchant (Reagecon Diagnostics Ltd, Ireland), which is a combination of hydrofluoric, nitric acid and water as described in ASTM-E407-99 [93]. A 100 mL volume of Kroll's etchant contains 92 mL distilled water, 6 mL of nitric acid and 2 mL of hydrofluoric acid. Each stent was placed in a 100 mL beaker horizontally fully immersed in 40 mL of the etchant solution. After etching for the desired time, the stents

are cleaned with water and dried for 5 minutes on a Metaserv specimen dryer (Buehler Ltd, United States).

## 3.12 Mechanical Testing

Mechanical testing was conducted using a Zwick/Roell Z2.5 (Zwick Roell Group, Germany) materials testing machine using an xForceP 200 N load cell (Zwick Roell Group, Germany). All data was processed using the TestXpert II V3.71 software (Zwick Roell Group, Germany) and exported for analysis.

### 3.12.1 Radial Strength Testing

Radial strength testing was conducted by compressing stents between two parallel plates. In compliance with ISO 25539-2[48] all stents were compressed to 50% of their nominal diameter. A 0.5 N or 0.1 N preload was applied to the stents dependent on stiffness prior to compression at a rate of 3 mm/min. A stiffness quantity was then defined as the slope of the initial linear region for comparative analysis between samples. Radial strength testing was conducted for the AM Intrastent, the tapered design. Performing the parallel plate crush test on tapered stents may not yield directly comparable results for stents with a uniform diameter due to the temporal evolution of the plate contact area. In this case, the crush test results for the tapered stents should only be directly compared for as built and post-processed tapered samples. Additionally, a commercial BARD Valeo Vascular Stent was also tested. A summary of test parameters is provided in Table 4 and an image of the test setup is provided in Figure 40.

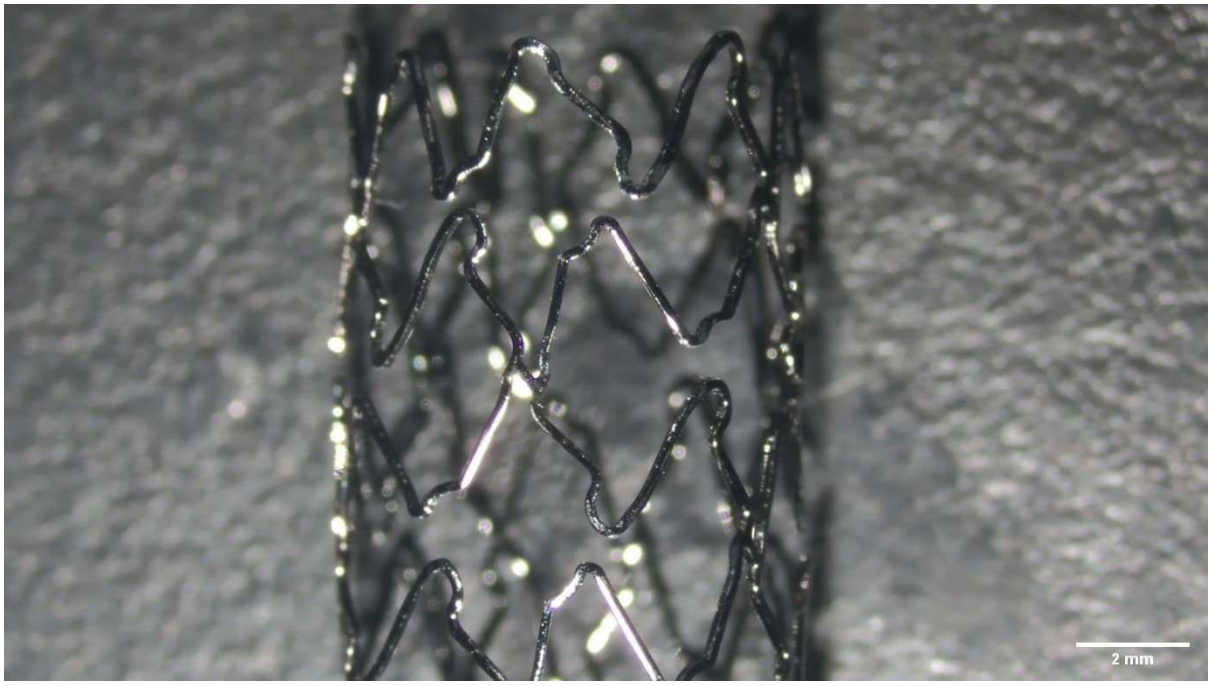


Figure 39 Microscopy image of BARD Valeo vascular stent

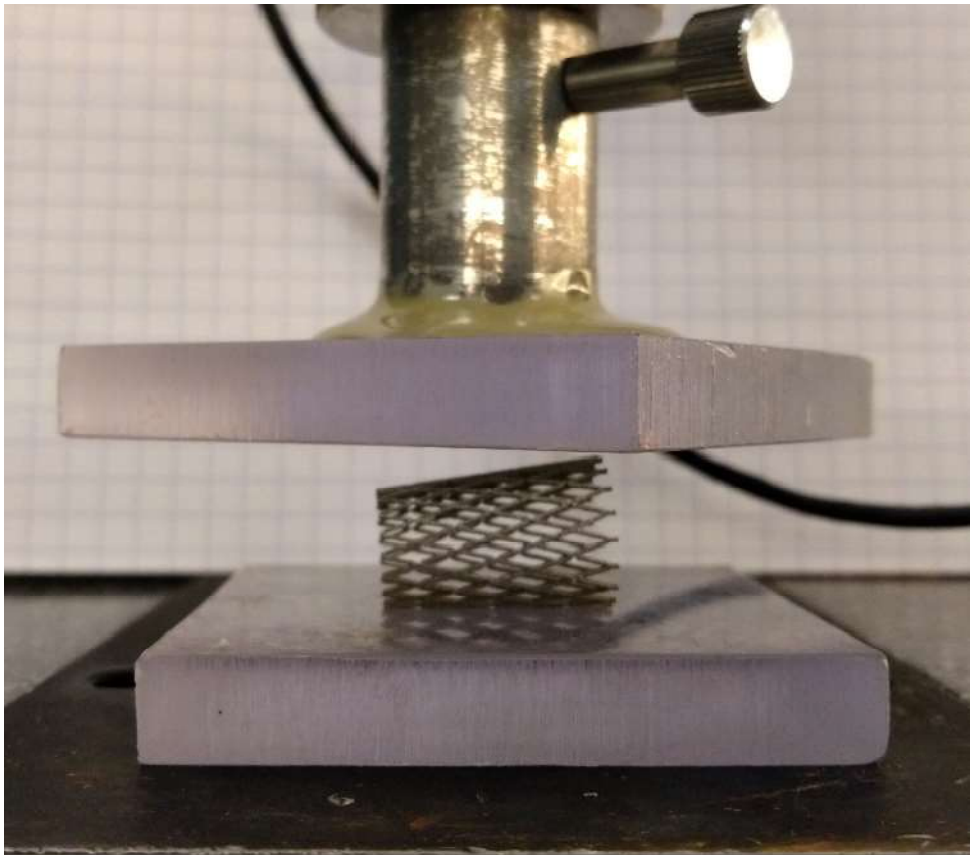

Figure 40 Parallel plate radial strength test setup with tapered stent design

Table 4 Stent type, geometric and testing parameters for radial strength testing

| Stent Type | Diameter (mm) | Compression (mm) | Length (mm) | Preload (N) |
|---|---|---|---|---|
| AM Intrastent AB (n=3) | 12 | 6 | 15 | 0.5 |
| AM Intrastent SB (n=3) | 12 | 6 | 15 | 0.5 |
| AM Intrastent CE (n=3) | 12 | 6 | 15 | 0.5 |
| AM Intrastent SB + CE (n=3) | 12 | 6 | 15 | 0.1 |
| AM Intrastent Tapered AB (n=1) | 9 | 4.5 | 19 | 0.1 |
| AM Intrastent Tapered SB + CE (n=1) | 9 | 4.5 | 19 | 0.1 |
| Valeo Vascular Stent (n=1) | 8.34 | 4.17 | 17 | 0.1 |

### 3.12.2 Flexibility Testing

Flexibility was quantified using three-point flexural testing. The test parameters were determined by the method outlined in ASTM F2606-8 [56]. The required span length and maximum for each stent type was calculated as a function of the stent length. For a given specimen with a length greater than 35 mm the span length is determined as follows.

$$L_s = \frac{L_{ST}}{1.093} - 2 \tag{7}$$

Where $L_s$ is the required span length and $L_{ST}$ is the stent length. Similarly, the maximum deflection, $\delta_m$, is then determined by the following Equation.

$$\delta_m = 0.2L_s \tag{8}$$

Specimens were preloaded to 0.1 N and then deflected at a rate of 10 mm/min. Similar to the radial strength testing a stiffness quantity was defined as the slope of the initial linear region for comparative analysis between samples Flexibility testing was conducted for the AM Intrastent and commercial IntraStent LD Max. A summary of test parameters is provided in Table 5 and an image of the test setup is provided in Figure 42.

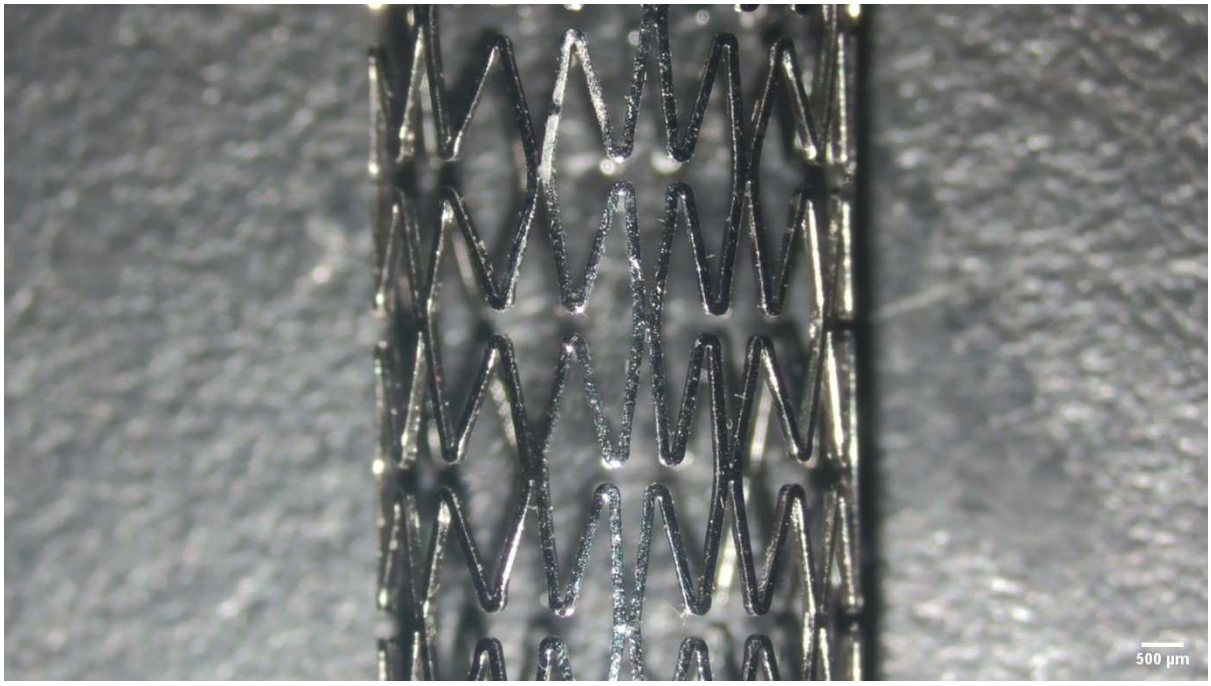


Figure 41 Microscopy image of Medtronic IntraStent

Table 5 Stent type, geometric and testing parameters for flexibility testing

| Stent Type | Length (mm) | Diameter (mm) | Span Length (mm) | Deflection (mm) |
|---|---|---|---|---|
| AM Intrastent AB (n=3) | 45.00 | 12 | 39.17 | 7.83 |
| AM Intrastent SB + CE (n=3 | 45.00 | 12 | 39.17 | 7.83 |
| Intrastent LD Max (n=1) | 35.30 | 8.47 | 30.30 | 6.06 |

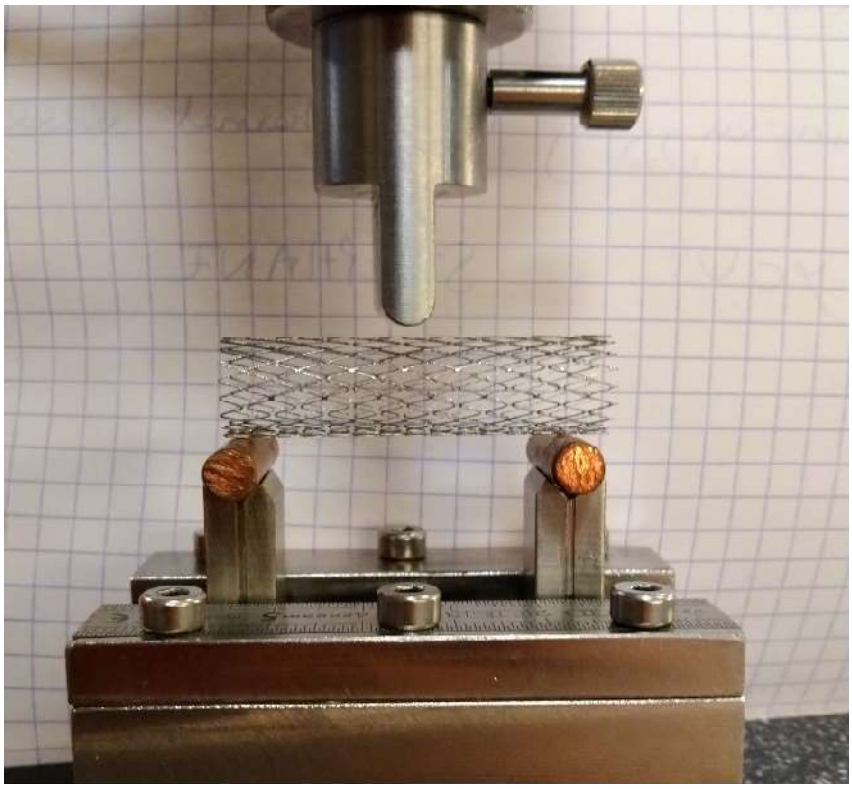

Figure 42 Three-point flexural test setup with sandblasted and chemically etched stent in place

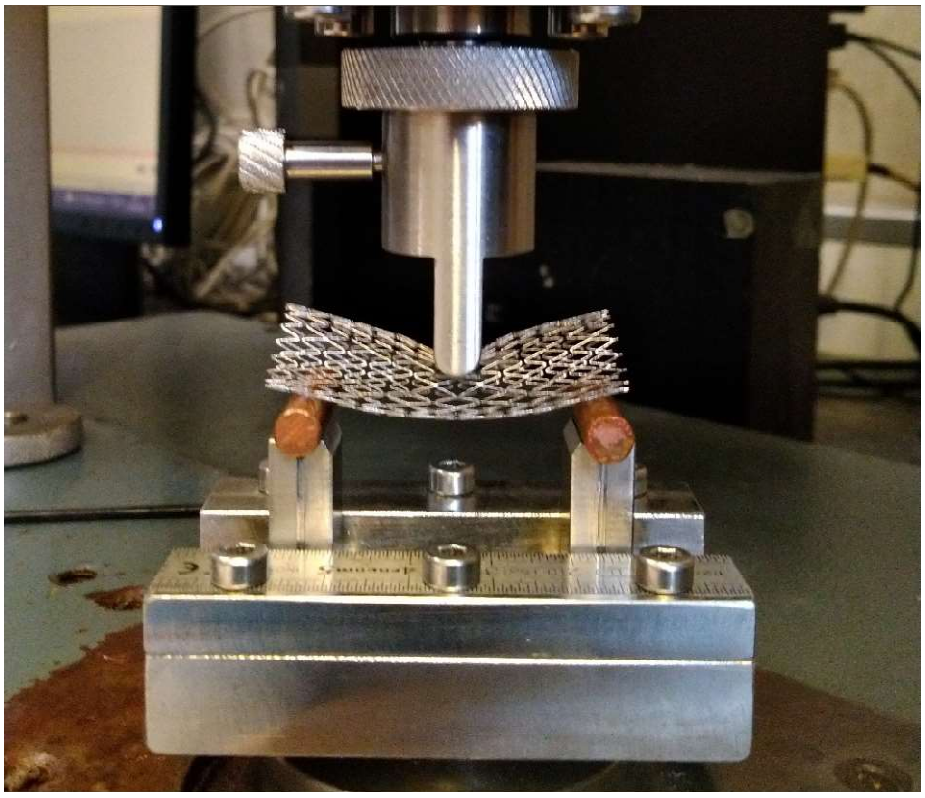

Figure 43 Three-point flexural test on sandblasted and chemically etched stent

## 3.13 AM Stent Crimping

To assess the crimping behaviour of the post-processed AM stents, a specimen from the highest combined sandblasting and etching time was crimped. A 2 mm diameter Boston Scientific Express LD stent delivery system (Boston Scientific, United States) was used to hold the stent in place. The stent was then crimped to this diameter using a Machine Solutions Inc. HV 500 crimping tool (Machine Solutions Inc., United States) and allowed to expand. This same protocol was followed for crimping a post-processed AM tapered stent.


Figure 44 AM IntraStent placed on 2 mm diameter Boston Scientific Express LD stent delivery system.

# Chapter 4. Results

## 4.1 Strut Thickness

Table 6 provides a summary of strut thickness measurement results for the initial feasibility and post processing study. Figure 45 shows a typical microscopy image of an as-built stent strut. Figure 46 and Figure 47 are microscopy images of sand-blasted and combined sandblasting and chemically etched stents respectively. Figure 48 provides a summary of strut thickness quantification for as built (AB), sandblasted (SB), chemical etching (CE) and, combined sandblasting and chemical etching (CE) stents. It should be noted that ± indicates standard deviation in all instances.

Table 6 Strut thickness measurement results for initial feasibility study and post-processing study. N=3 for all groups. SBXX indicates sand blasting and the number of seconds of post-processing and CEXX indicates chemical etching and the number of minutes the specimens were held in the solution.

| Stent Type | Strut Thickness (um) |
|---|---|
| Feasibility Study | |
| As Built | 432.52 ± 0.04 |
| Sand Blasted (120 seconds) | 361.26 ± 4.96 |
| Chemical Etched (20 minutes) | 238.56 ± 9.19 |
| Sand Blasted (120s) and Chemical Etched (20 mins) | 91.34 ± 15.47 |
| Post Processing Study | |
| SB30CE5 | 294.96 ± 25.90 |
| SB70CE7.5 | 284.77 ± 27.27 |
| SB90CE10 | 277.04 ± 50.88 |
| SB110CE12.5 | 189.00 ± 20.69 |
| SB60CE15 | 199.61 ± 15.25 |
| SB40CE17.5 | 173.4 ± 12.00 |
| SB50CE20 | 153.61 ± 8.40 |
| SB80CE22.5 | 141.72 ± 17.56 |
| SB100CE25 | 120.82 ± 15.84 |
| SB120CE27.5 | 91.25 ± 14.40 |
| Tapered Stents | |
| As Built - Upper | 303.33 ± 21.39 |
| As Built - Lower | 373.66 ± 25.50 |
| TP25SB120CE15 - Upper | 220.33 ± 9.87 |
| TP25SB120CE15 - Lower | 289.00 ± 16.52 |

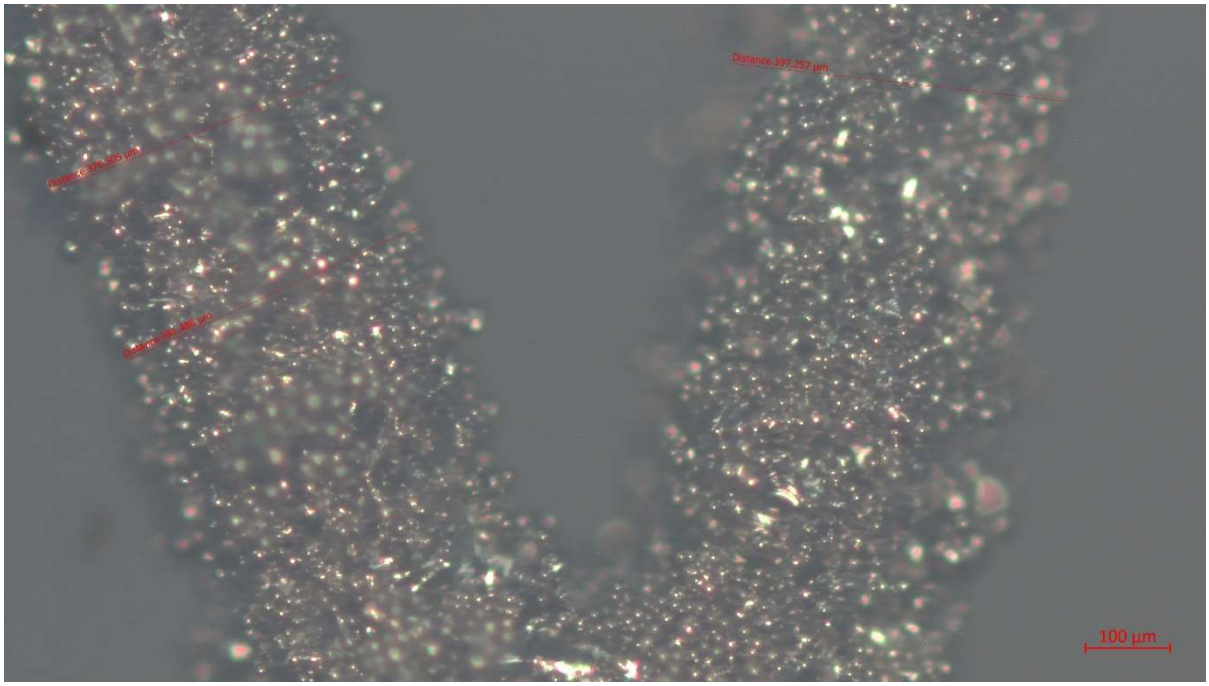


Figure 45 Microscopy image of as built stent with Type I defects visible

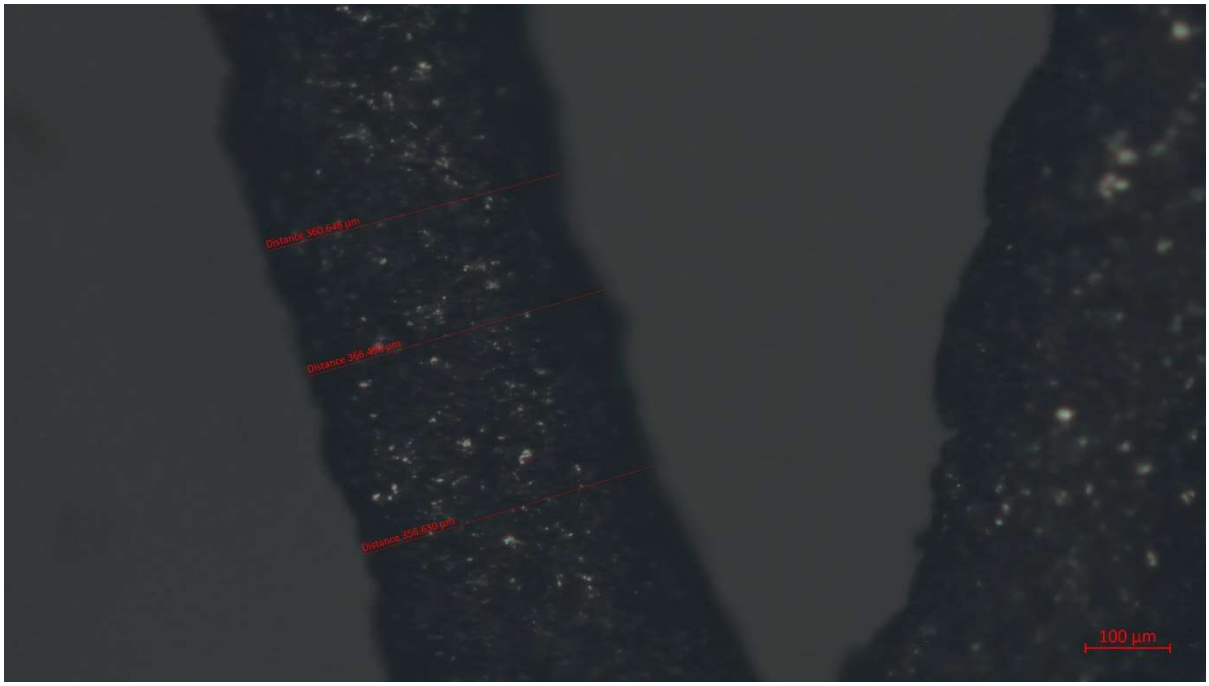


Figure 46 Microscopy image of sand-blasted stent

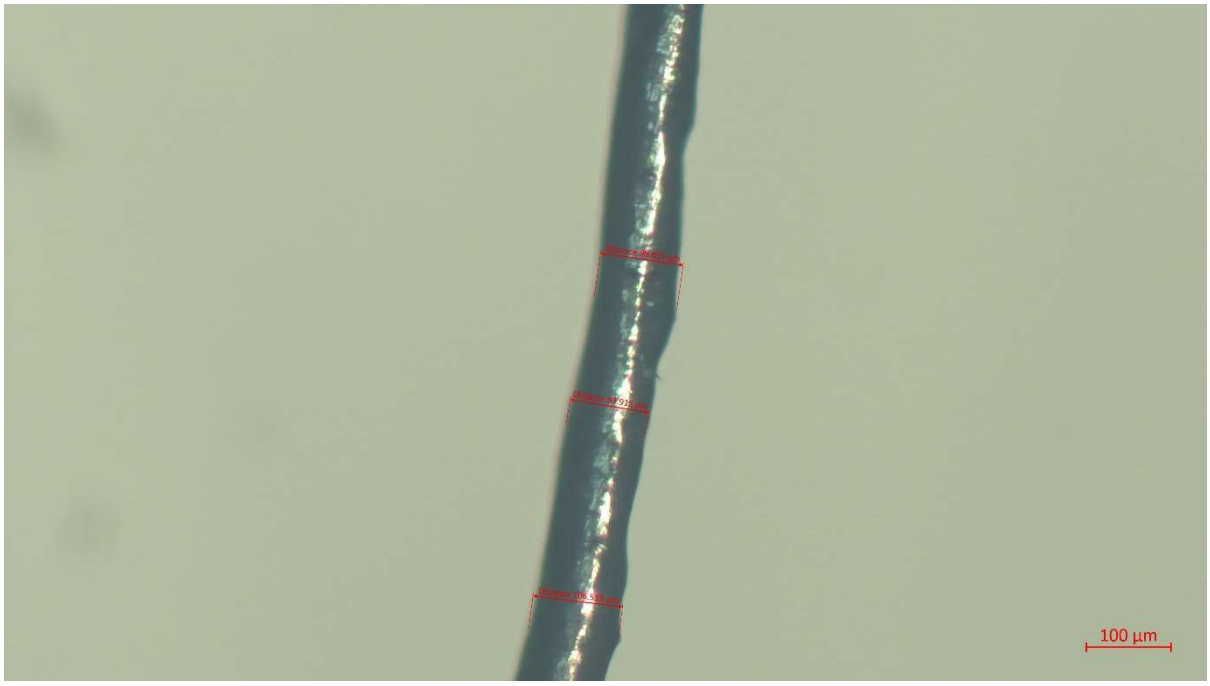


Figure 47 Microscopy image of sand-blasted and chemically etched stent

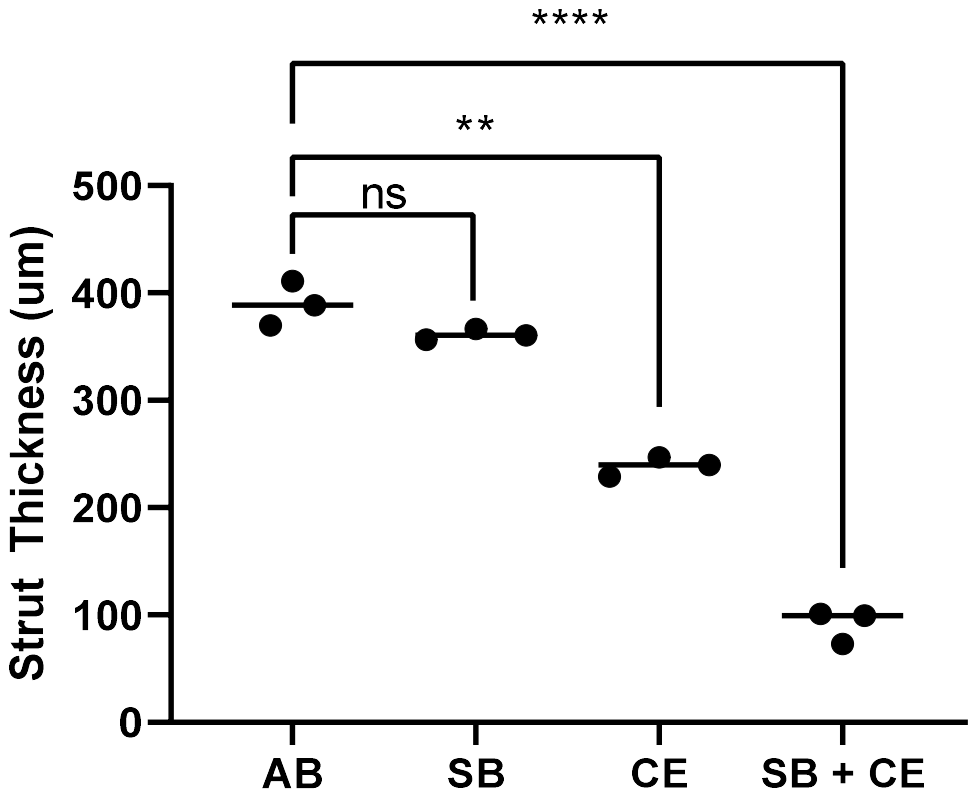


Figure 48 Representative strut thickness quantification for as built (AB), sandblasted (SB), chemical etching (CE) and, combined sandblasting and chemical etching (CE) stents. ** $p < 0.01$, **** $p < 0.0001$, ns = no statistically significant difference and N =3

Figure 49 displays the relationship between sandblasting time and strut thickness including a simple linear regression. Figure 50 similarly, displays the relationship between chemical etching time and stut thickness with simple linear regression.

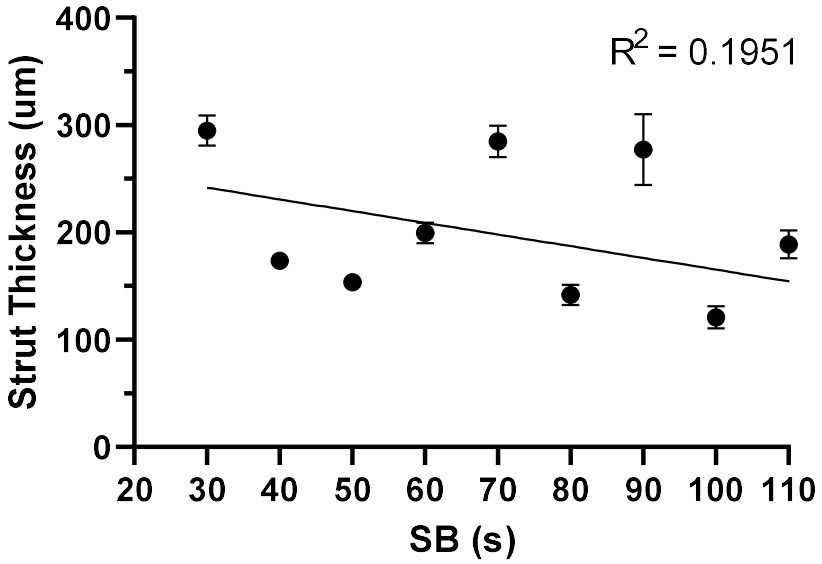


Figure 49 Plot of strut thickness against sandblasting time including simple linear regression. N = 5

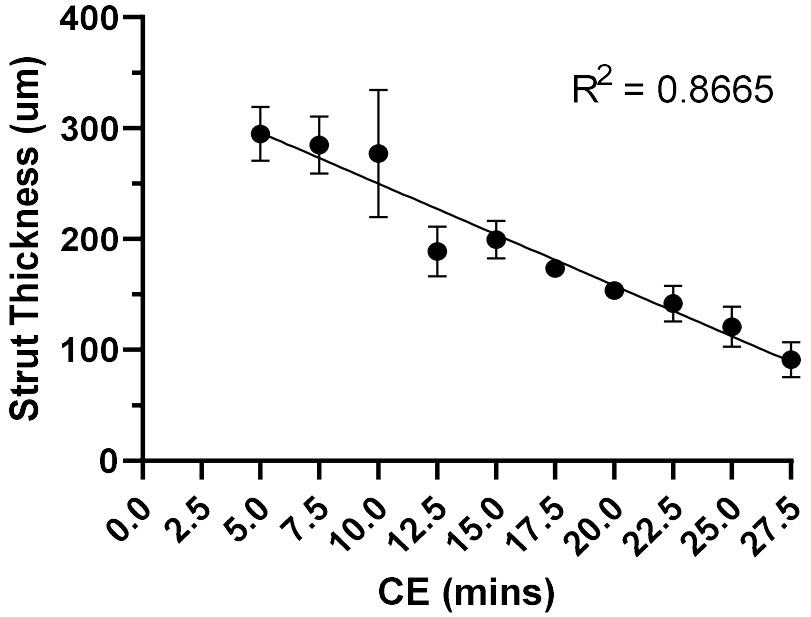


Figure 50 Plot of strut thickness against chemical etching time including simple linear regression. N = 5

## 4.2 Surface Roughness

### 4.2.1 Scanning Electron Microscopy

Figure 51 displays an SEM image of an as built stent. Figure 52 displays an SEM image of a sandblasted stent. Figure 53 displays an SEM image of a sandblasted and chemically etched stent.


Figure 51 Scanning electron microscopy (SEM) image of as built (AB) stent

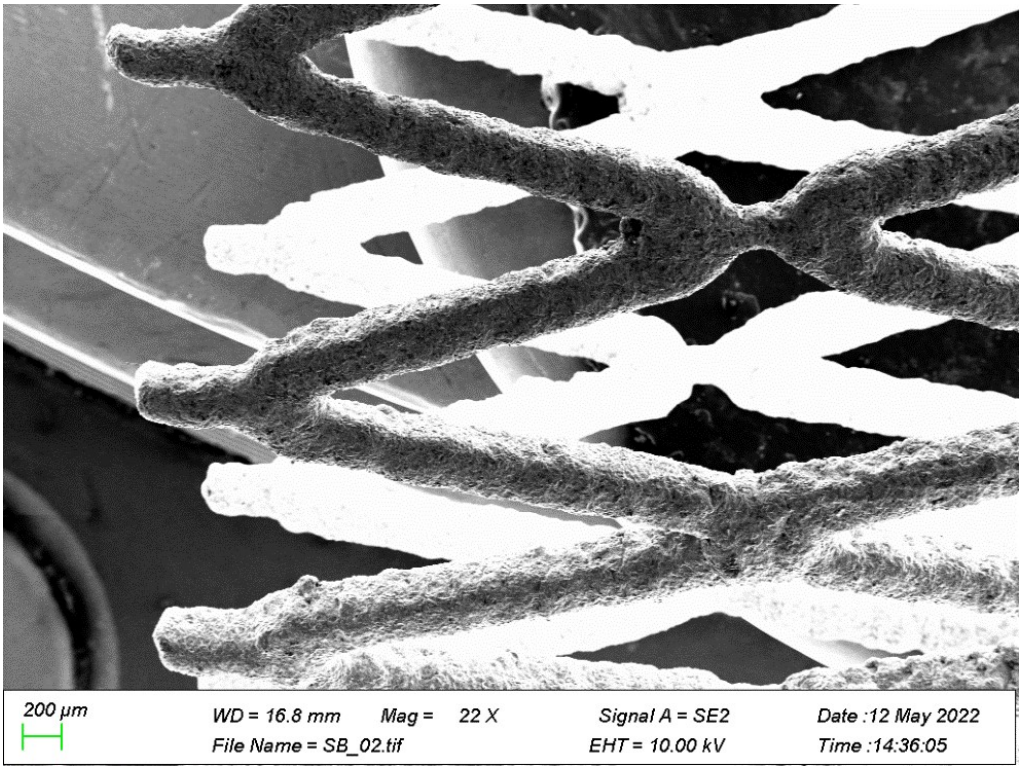


Figure 52 Scanning electron microscopy (SEM) image of sandblasted (SB) stent

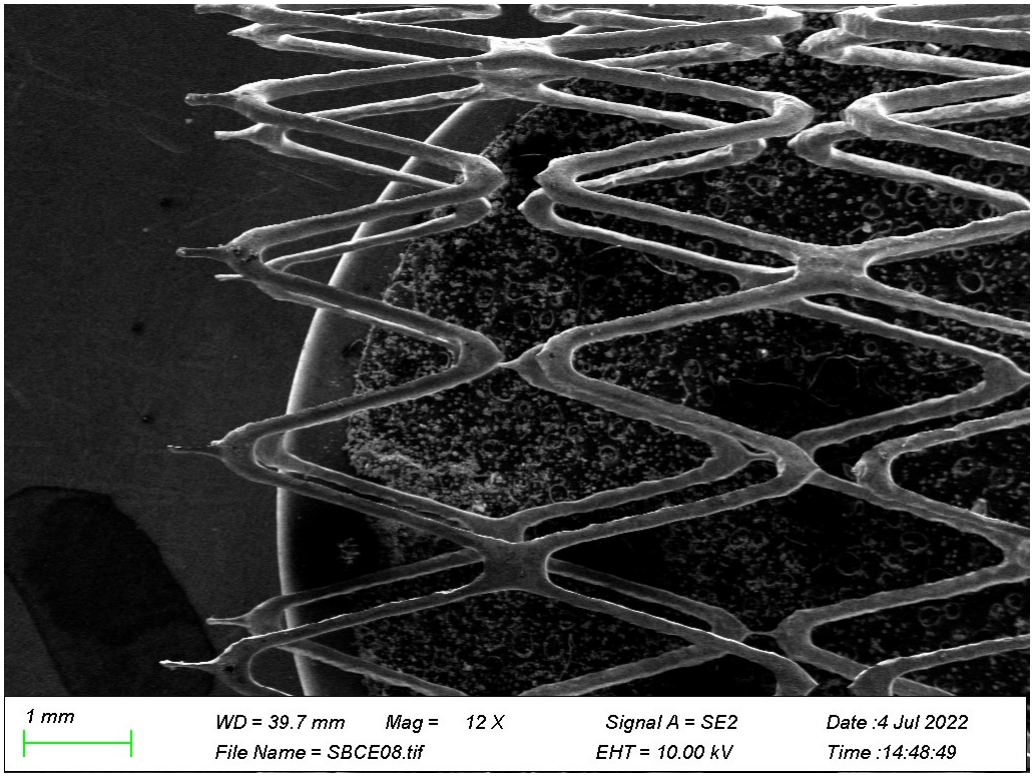


Figure 53 Scanning electron microscopy (SEM) image of sanblasted and chemically etched (SB+CE) stent

### 4.2.2 White Light Interferometry

Table 7 provides a summary of surface roughness results for each post-processing group and several commercial stents. Figure 54 displays surface roughness quantification for as built (AB), sandblasted (SB) and combined sandblasted and chemically etched (SB + CE) AM IntraStent. An unknown coronary stent, Abbot Multi-Link and Medtroinc Driver are also presented in this figure.

Table 7 Arithmetical surface roughness ($R_a$) results. N=5 for all groups

| Stent Type | Ra (um) |
|---|---|
| As Built | 0.86 ± 0.07 |
| Sandblasted (120 seconds) | 0.40 ± 0.04 |
| Sandblasted (120 seconds) and Etched (20 minutes) | 0.23 ± 0.02 |
| Multi-Link | 0.05 ± 0.01 |
| Driver | 0.12 ± 0.02 |

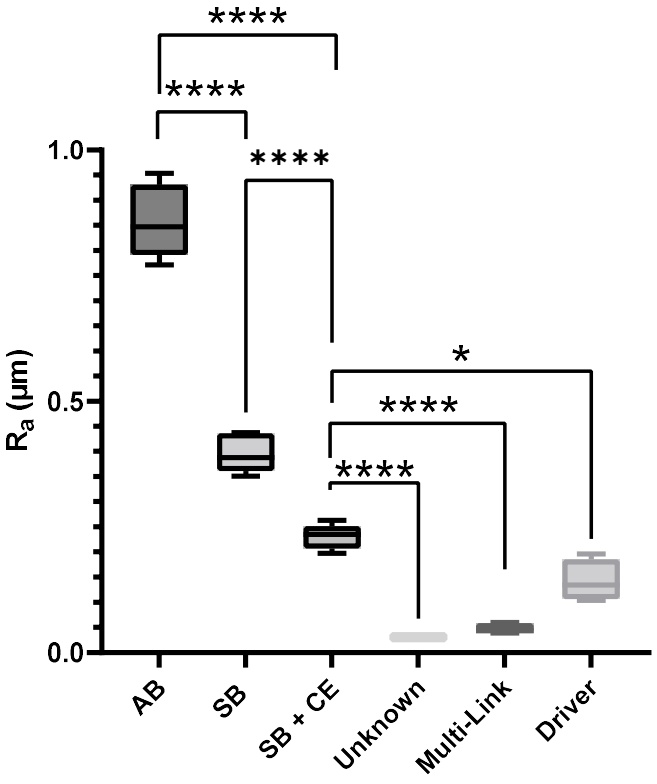


Figure 54 Arithmetical surface roughness ($R_a$) results for as built (AB), sandblasted (SB) and combined sandblasted and chemically etched (SB + CE) AM IntraStent. An unknown coronary stent, Abbot Multi-Link and Medtroinc Driver are also presented. **** $p < 0.0001$ and N = 5

## 4.3 Radial Strength

Table 8 displays all radial strength testing data for the post-processing study, commercial comparison, and tapered stents. Figure 55 displays representative radial strength testing data for as built, post-processed and commercial stents. Figure 56 displays radial strength testing data for an AM IntraStent sandblasted for 120 seconds and chemically etched for 27.5 minutes. Figure 57 displays radial strength testing results for the AM tapered stents.

Table 8 Summary for radial strength testing for post-processing stud, commercial comparison study and tapered stents. N=3 for post-processing study groups, N=1 for commercial comparison and tapered stents.

| Stent Type | Radial Stiffness (N/mm) | 50% Compression Force (N) |
|---|---|---|
| Post Processing Study | | |
| SB30CE5 | 3.14 ± 0.61 | 17.90 ± 3.18 |
| SB70CE7.5 | 2.43 ± 0.82 | 14.35 ± 4.18 |
| SB90CE10 | 2.14 ± 0.43 | 12.67 ± 1.96 |
| SB110CE12.5 | 0.59 ± 0.29 | 4.21 ± 1.47 |
| SB60CE15 | 0.60 ± 0.06 | 4.33 ± 0.22 |
| SB40CE17.5 | 0.57 ± 0.02 | 3.98 ± 0.41 |
| SB50CE20 | 0.34 ± 0.06 | 3.00 ± 0.36 |
| SB80CE22.5 | 0.24 ± 0.09 | 2.64 ± 0.32 |
| SB100CE25 | 0.17 ± 0.03 | 2.19 ± 0.04 |
| SB120CE27.5 | 0.13 ± 0.07 | 1.00 ± 0.32 |
| Commercial Comparison | | |
| Valeo | 3.86 | 2.07 |
| Tapered Stent | | |
| TP25 | 2.35 | 13.23 |
| TP25SB120CE15 | 0.32 | 1.82 |

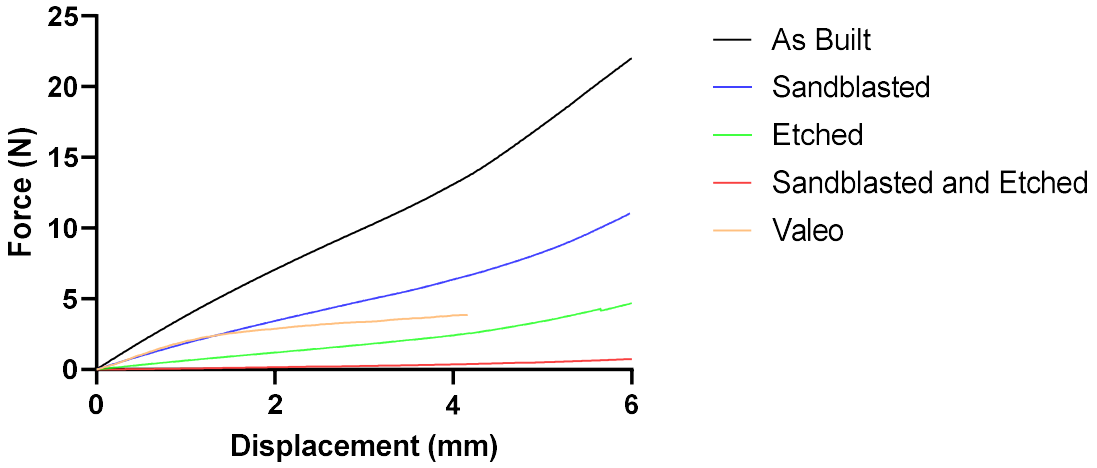


Figure 55 Representative radial strength testing results for AM IntraStent as built (AB), sandblasted (SB), chemically etched (CE), combined sandblasting and chemical etching (SB + CE) and Valeo vascular stent

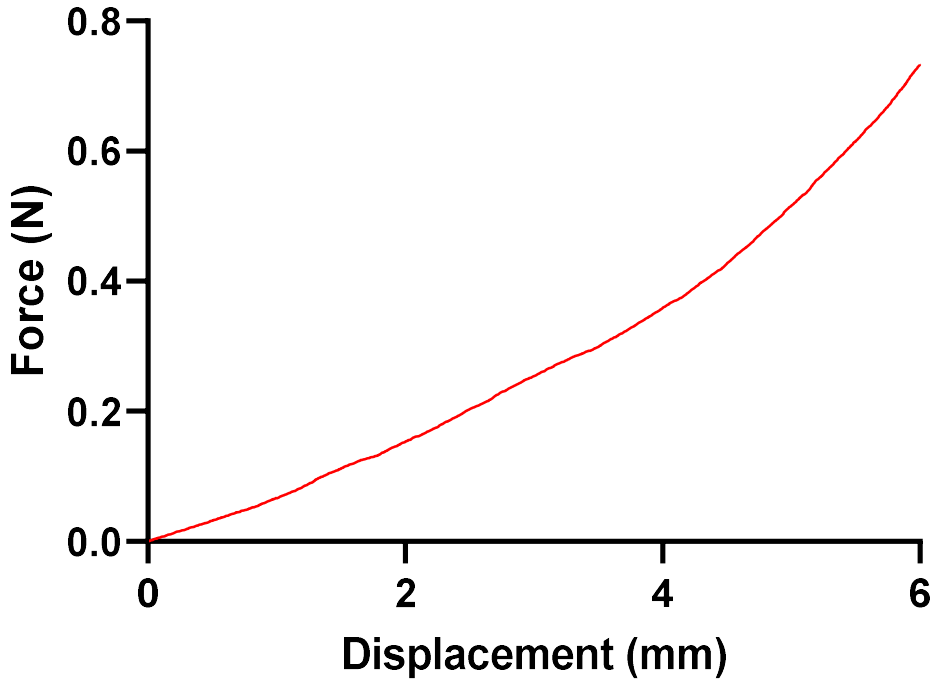


Figure 56 Radial strength testing results for AM IntraStent sandblasted for 120 seconds and chemically etched for 27.5 minutes

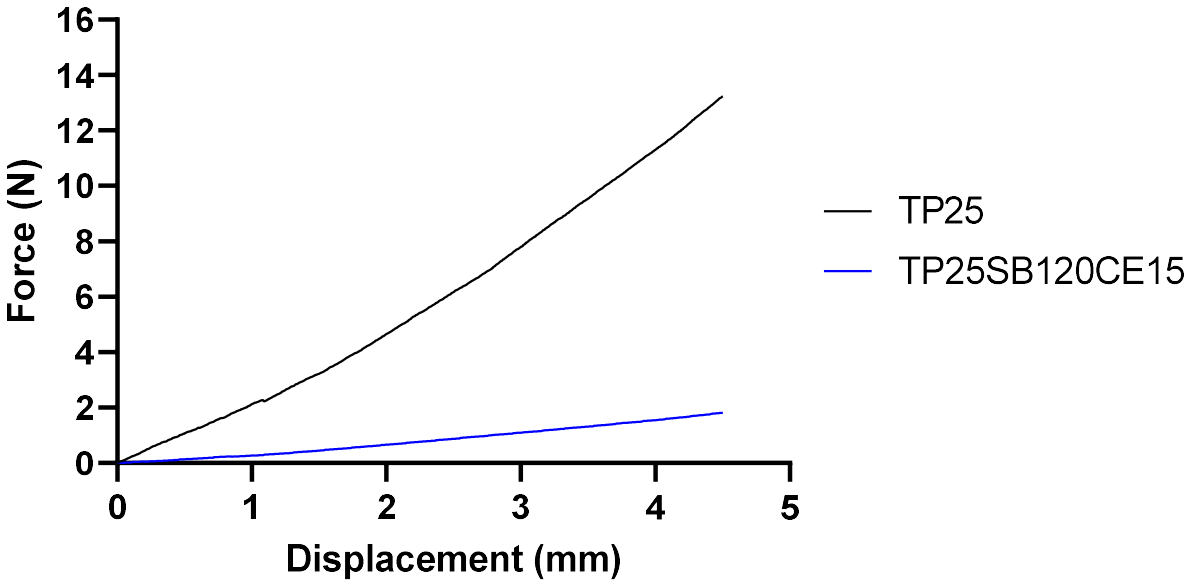


Figure 57 Radial strength testing results for tapered AM stent design as built and post-processed

Figure 58 displays a plot of radial stiffness against sand blasting time with simple linear regression. Similarly, Figure 59 plots radial stiffness against chemical etching time with simple linear regression. Figure 60 displays the commercial Valeo stent after radial strength testing.

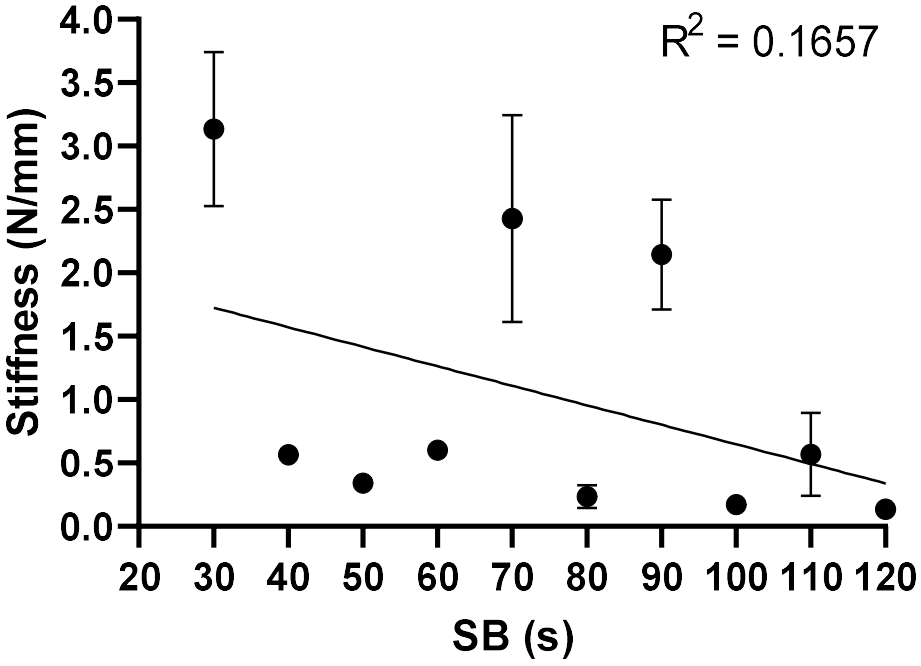


Figure 58 Plot of radial stiffness against sandblasting time including simple linear regression. N = 5

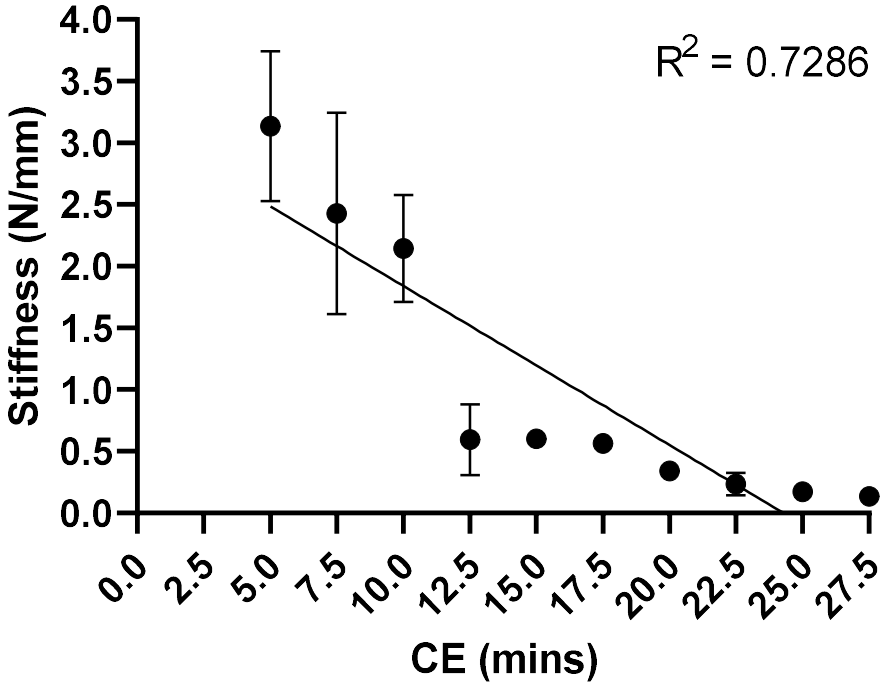


Figure 59 Plot of radial stiffness against chemical etching time including simple linear regression. N = 5

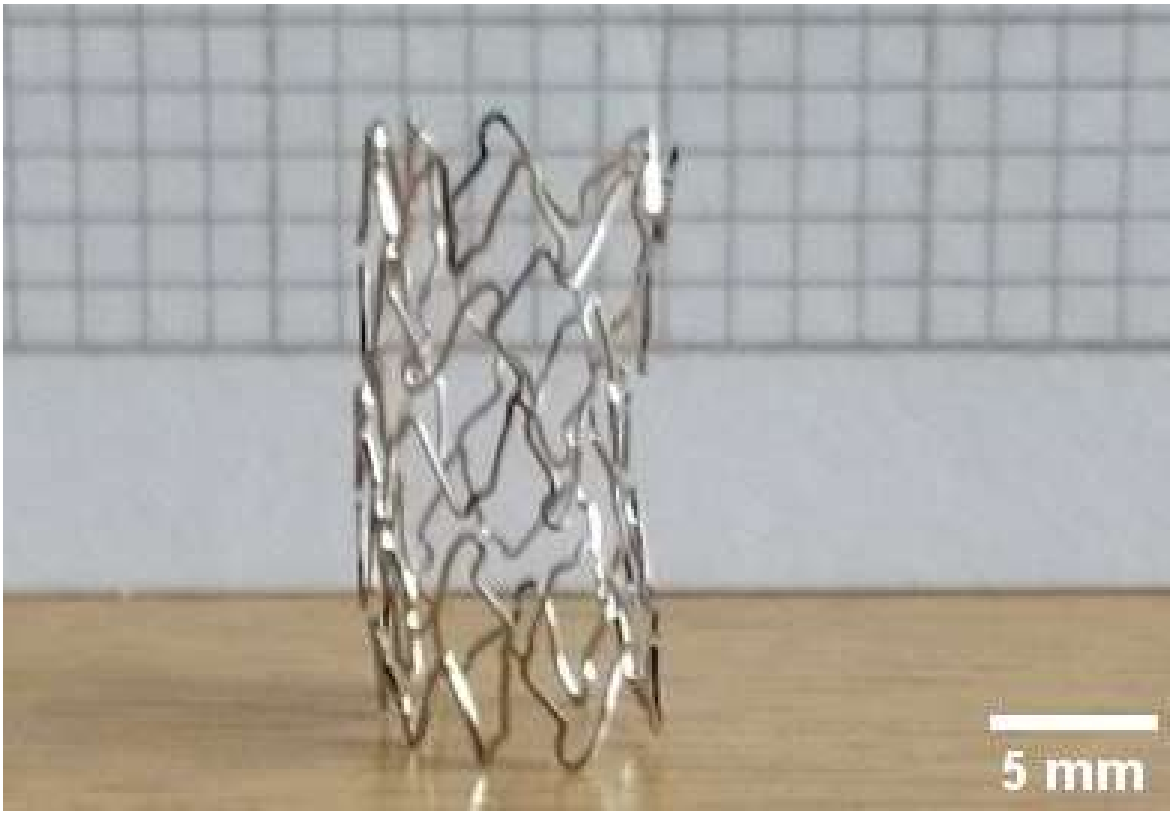


Figure 60 BARD Valeo vascular stent after compression testing

## 4.4 Flexibility

Table 9 provides a summary of all flexibility testing showing bending stiffness and maximum force results. Figure 61 provides all flexibility testing data. Figure 62 displays representative flexibility testing results for AM IntraStent as built (AB), combined sandblasting and chemical etching (SB + CE) and commercial IntraStent.

Table 9 Summary of flexibility testing with bending stiffness and maximum force results.

| Stent Type | Bending Stiffness (N/mm) | Maximum Force (N) |
|---|---|---|
| As Built (N=3) | 6.24 ± 0.04 | 39.90 ± 2.61 |
| SB120CE27.5 (N=3) | 0.29 ± 0.02 | 1.68 ± 0.24 |
| SB120CE27.5CE5 (N=2) | 0.15 ± 0.04 | 0.96 ± 0.18 |
| IntraStent (N=1) | 1.70 | 3.96 |

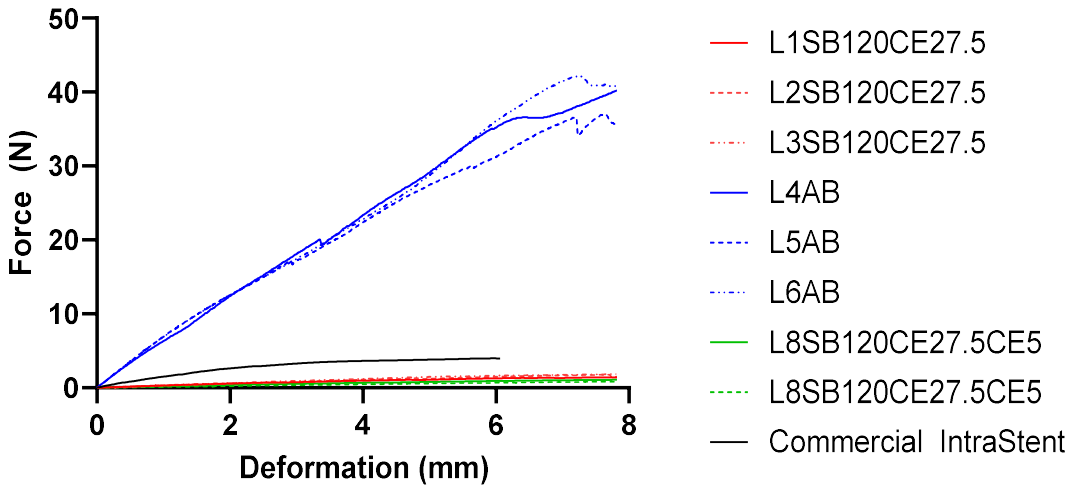


Figure 61 Flexibility testing results for all stent groups

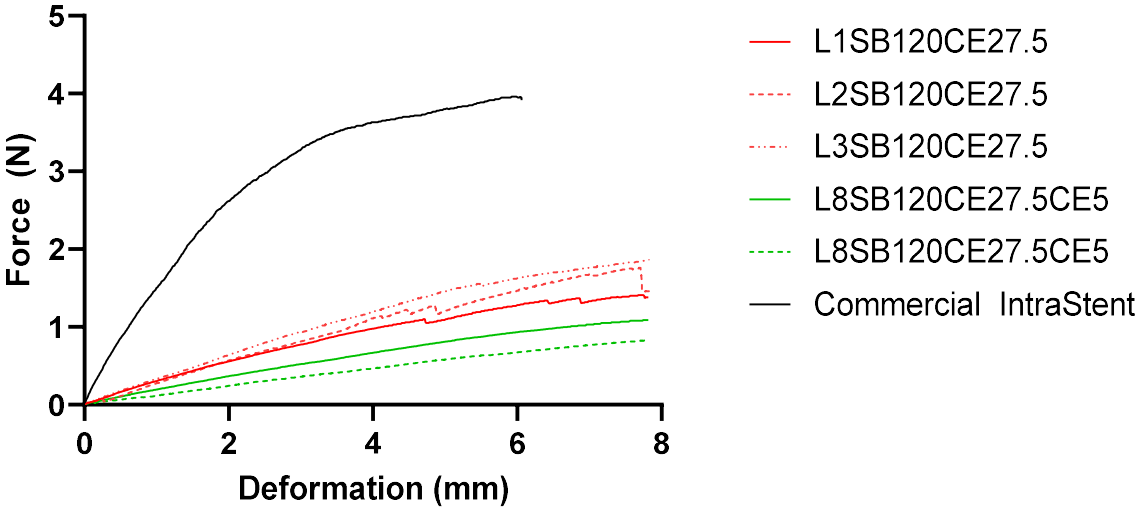


Figure 62 Flexibility testing results for combined sand blasting and chemical etching and commercial stent design

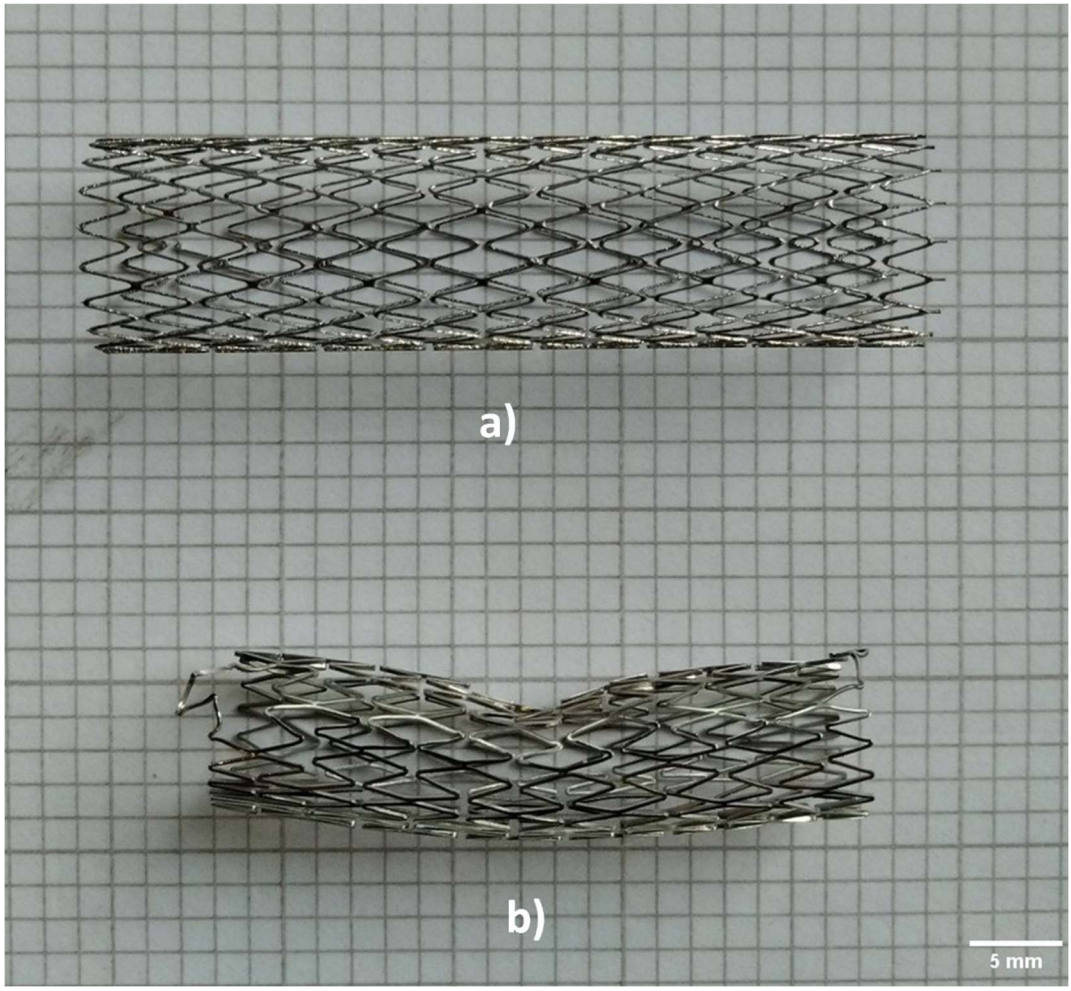


Figure 63 Post-processed AM stent (a) and commercial IntraStent (b) after three-point flexural testing

## 4.5 AM Stent Crimping

Figure 64displays a comparison between an as built tapered IntraStent and a specimen that underwent crimping onto a 2 mm wire after post processing. Table 10 provides a summary of elastic recoil results.

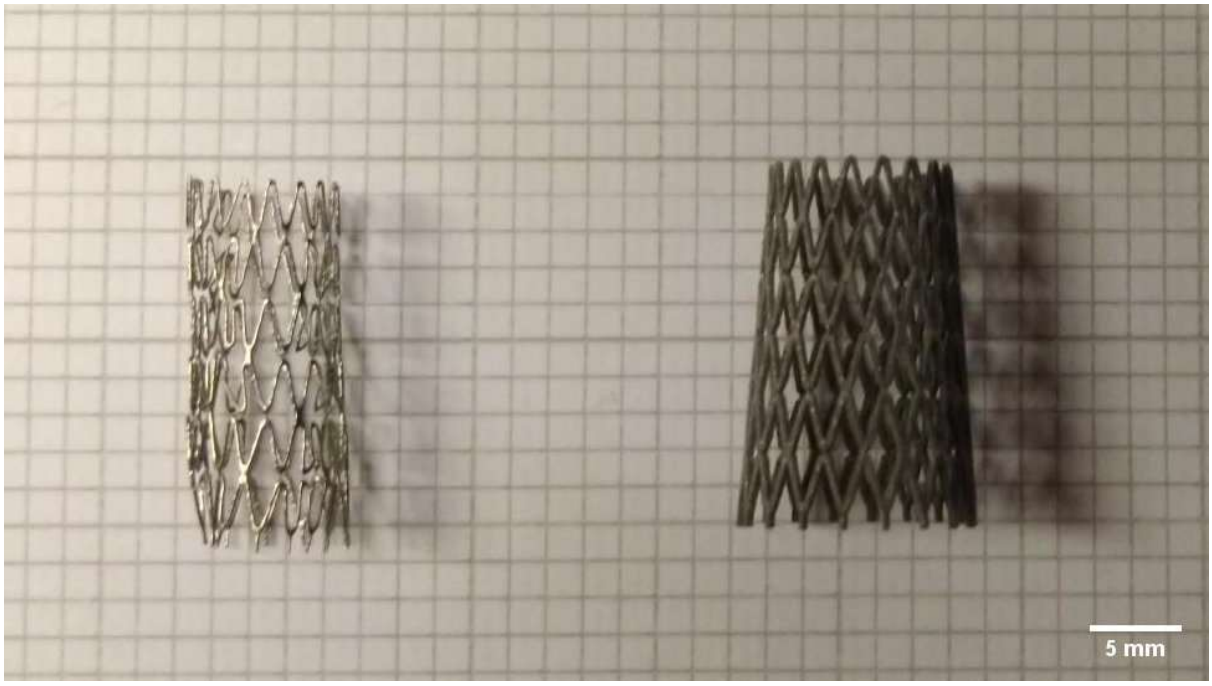


Figure 64 Crimped tapered stent with diameter of 8.5 mm after 120 seconds of sandblasting and 15 minutes of chemical etching

Table 10 Summary of elastic recoil results for AM stents

| Stent Type | Crimp Diameter (mm) | Expanded Diameter (mm) | Elastic Recoil (%) |
|---|---|---|---|
| SB120CE27.5 | 2.2 | 7.5 | 71% |
| TP25SB120CE15 | 2.2 | 8.5 | 74% |

## 4.6 Permanent Deformation

Table 11 provides a summary of permanent deformation measurements comparing commercial and AM stents.

Table 11 Summary of permanent deformation measurements comparing commercial stents for radial strength testing and flexural strength testing.

| Stent Type | Original Diameter (mm) | Recovered Diameter (mm) | Permanent Deformation (%) |
|---|---|---|---|
| Radial Strength Testing | | | |
| SB120CE27.5 | 12 | 12 | 0% |
| Valeo | 8.34 | 8.17 | 2.00% |
| Flexural Strength Testing | | | |
| SB120CE27.5 | 12 | 12 | 0% |
| IntraStent | 8.47 | 7.38 | 12.87% |

# Chapter 5. Discussion

## 5.1 Strut Thickness

The strut thickness results presented in Figure 46 indicate that sandblasting can effectively remove Type I defects. From Figure 48, sandblasting alone does not lead to a statistically significant difference in strut thickness. The use of chemical etching alone was shown to decrease strut thickness to a statistically significant level near 200 um from an average of 380 um. The combination of sandblasting and chemical etching has been shown to have the capability of developing stents with a strut thickness below 100 um. These strut sizes are below any previous work on AM metal stents [17], [18]. The ability to create stents with this wide range of strut thicknesses with post processing opens the possibility of using these devices for peripheral or coronary applications where strut thicknesses can range from 60-140 um.

Figure 58 indicates that there is little correlation between the sandblasting time and strut thickness. Figure 59 shows a much stronger correlation between chemical etching time and strut thickness, whereby increased chemical etching time correlates with a decrease in strut thickness. This relationship shows that chemical etching is the dominant factor in the post-processing workflow. These results overall show the feasibility of controlling strut thickness with post-processing and, the ability to achieve predictable and reproducible results. Variability may be reduced through mixing during the chemical etching process.

In the context of the tapered stent designs, the variation in strut thickness must be considered when selecting post-processing parameters. Using the 120 seconds of sandblasting and 27.5 minute of chemical etching on the tapered stents resulted in a portion of the stent being completely dissolved losing all structural integrity. To mitigate this, the chemical etching time was reduced to 15 minutes and all support structures were removed leading to achieve an open celled tapered design. To develop a controlled strut thickness control methodology with post-processing for stents with varied diameter, investigating the relationship between chemical etching parameters and initial strut thickness may be helpful in this respect.

Comparing with previous AM work seen in Table 12, strut thicknesses have ranged between 580 – 120 um. McGee *et al.* [17] achieved a strut thickness of 152 ± 43 um for chemically etched titanium stents ad the work of Wiesent *et al.* [19] ranging from 90-120 um for electropolished CoCr. In the context of AM titanium stents, this work, with the post-

processing technique presented has produced titanium AM stents with the lowest strut thickness to date being under 100 um.

## 5.2 Surface Roughness

### 5.2.1 Scanning Electron Microscopy

Figure 51 clearly shows Type I and Type II defects present on the as-built AM stents. The results of sandblasting shown in Figure 52 show effective Type I defect removal but with a clearly rough surface finish, little overall material removal and support structures still present. The combination of sandblasting and chemical etching, seen in Figure 53, decreases strut thickness further and enables the removal of support structures, realizing an open cell design like the commercial IntraStent. It is noted that support and material removal was not observed as fully homogenous within specimens. This may be caused by the formation of gas bubbles that becomes stuck to the specimen inhibiting material removal locally and causing uneven etching. This behaviour has been noted in the literature [94] and agitation during the chemical etching process may mitigate this issue.

Qualitatively, these results are an improvement on previous work described by McGee *et al.* [17], as seen in Figure 65. This improvement may be due to the use of sandblasting prior to chemical etching. The removal of Type I defects creates a more uniform surface area for chemical etching and may increase process efficiency, enabling the manufacture of smaller strut thicknesses and the use of lower concentration of acids in etching solutions.

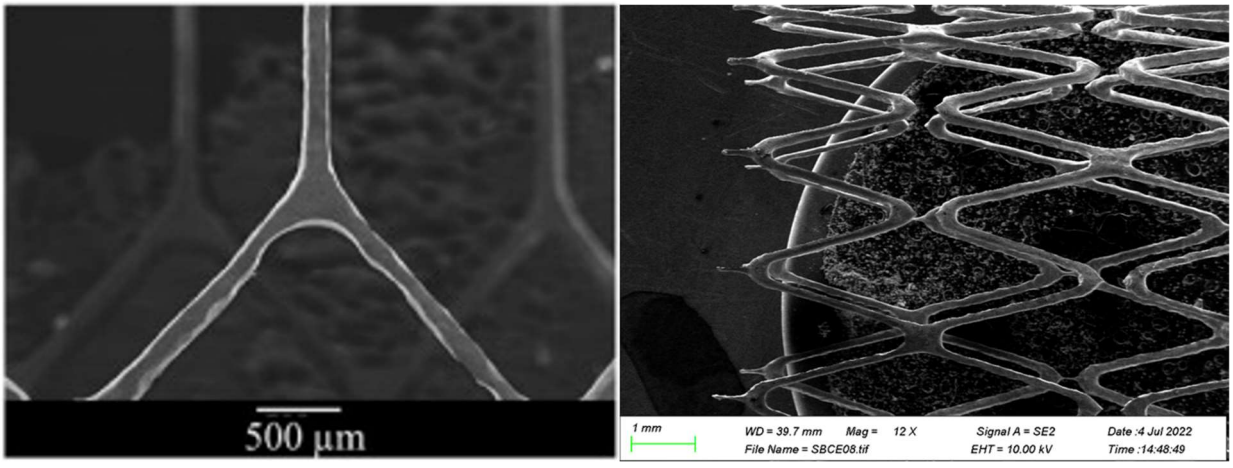


Figure 65 SEM image of stent strut from McGee *et al.* [17] and this work after post processing

### 5.2.2 White Light Interferometry

The use of sandblasting leads to a lower average surface roughness from the as built geometry as seen in Figure 54. There is a statistically significant reduction of 52% between the mean values. The combination of sandblasting and chemical etching further reduces the mean surface roughness a statistically significant amount with 70% reduction between mean values. Comparing to commercial stents, there is a statistically significant difference between the combined sandblasting and chemical etching stents, the unknown coronary stent and Multi-Link stent where commercial roughness values are lower. In the case of the Driver stent there is a low level of statistical significance in the difference with the combined sandblasted and chemically etched stent. This result may indicate that with some fine tuning of post processing parameters such as the acid concentration or size of blasting media, there is potential to achieve surface roughness levels similar to commercial stents. The addition of an electro-polishing step, commonly used in commercial stent fabrication may decrease surface roughness further.

Comparing with Ra value reported in the literature for AM stents presented in Table 12, this work presents the lowest average surface roughness for AM stents. The as built stents have 77% lower average surface roughness than the lowest as built value reported in the literature by McGee *et al.* [17]. This indicates that the printing parameters used in this study are better optimized for a smooth surface finish. Similarly, a 70% decrease in surface roughness is seen between the etched stents in McGee *et al*. and the combined sand blasted and chemically etched stents in this work. This work shows the lowest average surface roughness for both as built and post-processed stents to date.It is of note that a similar surface roughness is achieved using glass bead blasting compared to sandblasting in the work presented by Grad *et al.*[23], noting that the blasting media used has a particle size distribution of 70-110 um. This is similar to the 120 um particle size blasting media used in this thesis. Conversely, the same work notes a much higher surface roughness for sandblasted specimens, with the mean being 81% higher. Grad *et al.* notes the sandblasting media used had a particle size of 500-700 um, showing that particle size has a large influence on the surface roughness achieved by media blasting stents. This reinforces the previously stated point that decreasing the particle size may reduce the surface roughness further. Similarly, the lowest surface roughness reported in the literature by Grad *et al.* is after the use of electropolishing. There may be some influence of SS316L and its suitability for electropolishing, but this warrants further investigation of the use of electropolishing in the context of this work.

A limitation of using Ra as a comparison quantity for surface roughness is its dependence on sampling parameters used and filtering techniques applied in post-processing software. Most work within the literature does not provide much detail on this, specifically parameters such as the back scan length, sampling length and invalid pixel filtering. ISO specifies recommended sampling lengths for given Ra ranges but there are generally not achievable at the length scales of AM stents. The inclusion of additional surface roughness quantites such as the maximum peak to valley height (Rz) in combination with Ra may put surface roughness into better context for analysis in future work.

Table 12 Comparison of Ra values for AM stents in the literature. Values from this work are indicated in bold

| Stent Type | Material | Stut Thickness (um) | Ra (um) | Source |
|---|---|---|---|---|
| **As Built** | **Ti64** | **432.52 ± 0.04** | **0.86 ± 0.07** | |
| **Sandblasted** | **Ti64** | **361.26 ± 4.96** | **0.40 ± 0.04** | |
| **Sandblasted and Etched** | **Ti64** | **91.34 ± 15.47** | **0.23 ± 0.02** | |
| **Multi-Link** | **CoCr** | **100** | **0.05 ± 0.01** | |
| **Driver** | **CoCr** | **90** | **0.12 ± 0.02** | |
| AM Closed Cell Design | CoCr | 250-300 | 12.00-9.50 | [13] |
| AM Parametric Design As Built | CoCr | 160-195 | 9.3 | [14] |
| AM Parametric Design Electropolished | CoCr | 90-120 | 3 | [19] |
| AM Open Cell Aortic Design As Built | SS316L | N/A | 5.5 | [20] |
| AM Open Cell Aortic Design Sand Blasted | SS316L | N/A | 2.2 | [20] |
| AM Open Cell Aortic Glass Blast | SS316L | N/A | 0.5 | [20] |
| AM Open Cell Aortic Electropolish | SS316L | N/A | 0.25 | [20] |
| AM Tubing | SS316L | 500 | 6.68 | [20] |
| AM Simple Honeycomb | Ti64 | 580 ± 26 | 3.76 ± 1.34 | [17] |
| AM Novel Design Etched | Ti64 | 246 ± 36 | 1.13 ± 0.71 | [17] |
| AM Simple Honeycomb Etched | Ti64 | 152 ± 43 | 0.39 ± 0.28 | [17] |

## 5.3 Radial Strength

The results in Figure 55 indicate a clear decrease in radial stiffness with post processing. Radial stiffness is seen to decease with sandblasting, a greater amount with chemical etching and even more so with the combined sandblasting and chemically etched stents. This trend is like that seen for strut thickness. Similar results are seen for the tapered stent in Figure 57.

Like strut thickness, there is little correlation between sandblasting time and radial stiffness as seen in Figure 58. A stronger correlation is seen between chemical etching time and radial stiffness whereby increased chemical etching time correlates with decreased radial stiffness. At 12.5 minutes of chemical etching a large drop in radial stiffness is seen, this may be caused by the removal of support structures. It is noted that no fractures were seen for any radial strength testing.

Comparing the commercial VALEO stent, the force displacement behaviour is similar to the sandblasted AM stents, but all AM stents exhibit a more linear response than the commercial stent. For the combined sandblasted and chemically etched very little permanent deformation occurs in comparison to the VALEO stent. These results show the feasibility of compressing AM stents into a delivery sheath for deployment. The large amount of radial recoil also opens questions around balloon expansion deployment - these stents may require large amounts of overinflation to induce permanent deformation to achieve a desired lumen gain.

For the tapered results, similar behaviour is seen to the post-processing study where a decrease in radial stiffness and maximum compression force is seen with post-processing. It is difficult to directly compare the tapered devices to those with a uniform diameter using parallel plate crush testing due to non-uniform contact with the plates during testing. In this context, the use of a radial crimping device may be more appropriate or the use of computational modelling including stress analysis to develop a better understanding of the mechanical behaviour of these devices. Increased sample numbers and investigating testing techniques in future work would also improve understanding of mechanical performance.

Comparing results to the literature presented in Table 13 and Table 14, the post-processed AM stents in this work were within the range and below typical radial strength properties reported in the literature. In the context of previously produced AM stents, this work has produced stents with a 50% lower maximum compression force and 71% lower radial stiffness compared to the work for McGee *et al.* [17] that also used titanium. Additionally, the stents in this study had a 32% lower radial stiffness than the lowest reported in the literature by Wiesent *et al.* [22] and therefore the lowest radial stiffness achieved for AM stents to date. In comparison to the commercial stents presented in these tables, the work of Bae *et al.* [95] notes a 50% compression force range of 2.73 – 3.89 N for CoCr and SS316L stents, this work has produced stents within this range of values and thus have comparable

radial strength characteristics to commercial stents. Comparing the radial stiffness values presented in literature, commercial NiTi stents have been shown to range between 0.2 – 0.9 N/mm in Malcekis *et al.* [76], this work has also produced stents within this range. It is of note the stents in this work have the radial characteristics of commercial CoCr and SS316L stents in terms of compression force required to reach 50% deformation and of commercial NiTi stents in terms of radial stiffness.

The variability in results may be explained by variations in the chemical etching process previously discussed and the positioning of samples on the parallel plates may play a role in determining radial stiffness.

It is of note that with the use of appropriate heat treatment methods for Ti6Al4V such as HIP, greater radial stiffnesses may be achieved. This is supported by the work of Kasperovich *et al*.[21] where an increase in Young's Modulus was observed for heat treated specimens, in turn this would increase the scaffolding ability of devices while maintaining lower strut thicknesses.

Overall, these results show the feasibility of developing stents with varied radial strength properties along the stent length with AM and post-processing. Stents with these properties may be useful for treatment of diseases such as aortic coarctation, where devices could be made radially stiffer at the coarctation region and less so proximal and distal to the coarctation where tissue is less affected or unaffected by the disease. These properties could ensure sufficient lumen gain and scaffolding at the coarctation region and, prevent overstretching and thus tissue damage outside of the coarctation by conforming to the vessel instead of stretching it during balloon expansion. These factors may reduce tissue injury rates in stent treatment of aortic coarctation in comparison to commercial devices that have uniform radial stiffness to ensure sufficient lumen gain.

Table 13 Comparison of force required to reach compression of 50% for a given stent diameter in the literature. Results from this work are indicated in bold

| Stent Type | Material | Stut Thickness (um) | Diameter (mm) | Length (mm) | 50% Compression Force (N) | Source |
|---|---|---|---|---|---|---|
| **SB30CE5** | **Ti64** | **294.96 ± 25.90** | **12** | **15** | **17.90 ± 3.18** | |
| **SB70CE7.5** | **Ti64** | **284.77 ± 27.27** | **12** | **15** | **14.35 ± 4.18** | |
| **SB90CE10** | **Ti64** | **277.04 ± 50.88** | **12** | **15** | **12.67 ± 1.96** | |
| **SB110CE12.5** | **Ti64** | **189.00 ± 20.69** | **12** | **15** | **4.21 ± 1.47** | |
| **SB60CE15** | **Ti64** | **199.61 ± 15.25** | **12** | **15** | **4.33 ± 0.22** | |
| **SB40CE17.5** | **Ti64** | **173.4 ± 12.00** | **12** | **15** | **3.98 ± 0.41** | |
| **SB50CE20** | **Ti64** | **153.61 ± 8.40** | **12** | **15** | **3.00 ± 0.36** | |
| **SB80CE22.5** | **Ti64** | **141.72 ± 17.56** | **12** | **15** | **2.64 ± 0.32** | |
| **SB100CE25** | **Ti64** | **120.82 ± 15.84** | **12** | **15** | **2.19 ± 0.04** | |
| **SB120CE27.5** | **Ti64** | **91.25 ± 14.40** | **12** | **15** | **1.00 ± 0.32** | |
| AM Closed Cell AB | SS316L | 200 ± 25 | 3.7 | 16.94 | 7.11 ± 0.63 | [19] |
| AM Closed Cell HT | SS316L | 210 ± 35 | 3.7 | 16.94 | 5.87 ± 0.49 | [19] |
| AM Closed Cell EP-HT | SS316L | 130 ± 30 | 3.7 | 16.94 | 2.39 ± 0.23 | [19] |
| CNUH Stent | CoCr | N/A | 3 | N/A | 2.40 ± 0.27 | [89] |
| Promus Element | PtCrL | N/A | N/A | N/A | 2.89 ± 0.28 | [89] |
| Cypher | SS316L | N/A | N/A | N/A | 3.89 ± 0.34 | [89] |
| Resolute Integrity | CoCrL | N/A | N/A | N/A | 3.71 ± 0.31 | [89] |
| Xience PRIME | CoCrL | N/A | N/A | N/A | 2.73 ± 0.24 | [89] |
| AM Simple Honeycomb | Ti64 | 580 ± 26 | 10 | 19.89 | 107.87 | [17] |
| AM Novel Design Etched | Ti64 | 246 ± 36 | 10 | 18.59 | 8.41 ± 2.60 | [17] |
| AM Honeycomb Etched | Ti64 | 152 ± 43 | 10 | 19.89 | 1.43 ± 0.37 | [17] |

Table 14 Comparison of radial stiffness results in the literature for commercial and AM stents. Results from this work are indicated in bold.

| Stent Type | Material | Stut Thickness (um) | Diameter (mm) | Length (mm) | Radial Stiffness (N/mm) | Source |
|---|---|---|---|---|---|---|
| **SB30CE5** | **Ti64** | **294.96 ± 25.90** | **12** | **15** | **3.14 ± 0.61** | |
| **SB70CE7.5** | **Ti64** | **284.77 ± 27.27** | **12** | **15** | **2.43 ± 0.82** | |
| **SB90CE10** | **Ti64** | **277.04 ± 50.88** | **12** | **15** | **2.14 ± 0.43** | |
| **SB110CE12.5** | **Ti64** | **189.00 ± 20.69** | **12** | **15** | **0.59 ± 0.29** | |
| **SB60CE15** | **Ti64** | **199.61 ± 15.25** | **12** | **15** | **0.60 ± 0.06** | |
| **SB40CE17.5** | **Ti64** | **173.4 ± 12.00** | **12** | **15** | **0.57 ± 0.02** | |
| **SB50CE20** | **Ti64** | **153.61 ± 8.40** | **12** | **15** | **0.34 ± 0.06** | |
| **SB80CE22.5** | **Ti64** | **141.72 ± 17.56** | **12** | **15** | **0.24 ± 0.09** | |
| **SB100CE25** | **Ti64** | **120.82 ± 15.84** | **12** | **15** | **0.17 ± 0.03** | |
| **SB120CE27.5** | **Ti64** | **91.25 ± 14.40** | **12** | **15** | **0.13 ± 0.07** | |
| AM Type 1 | CoCroMo | 200 | 5 | 80 | 0.75 | [15] |
| AM Type 2 | CoCroMo | 180 | 5 | 804 | 0.23 | [15] |
| AM Type 3 | CoCroMo | 200 | 5 | 804 | 0.75 | [15] |
| AM Type 4 | CoCroMo | 180 | 5 | 80 | 0.73 | [15] |
| AM Type 5 | CoCroMo | 200 | 5 | 80 | 0.38 | [15] |
| AM Type 6 | CoCroMo | 200 | 5 | 80 | 0.19 | [15] |
| AM Type 7 | CoCroMo | 180 | 5 | 80 | 0.31 | [15] |
| Absolute Pro | NiTi | N/A | 6.99 ± 0.45 | 80 | 0.56 | [70] |
| Supera | NiTi | N/A | 6.99 ± 0.45 | N/A | 0.3 | [70] |
| LifeStent | NiTi | N/A | 6.99 ± 0.45 | N/A | 0.84 | [70] |
| Innova | NiTi | N/A | 6.99 ± 0.45 | N/A | 0.66 | [70] |
| Zilver | NiTi | N/A | 6.99 ± 0.45 | N/A | 0.28 | [70] |
| Smart Control | NiTi | N/A | 6.99 ± 0.45 | N/A | 0.2 | [70] |
| Smart Flex | NiTi | N/A | 6.99 ± 0.45 | N/A | 0.6 | [70] |
| EverFlex | NiTi | N/A | 6.99 ± 0.45 | N/A | 0.64 | [70] |
| Viabahn | NiTi | N/A | 6.99 ± 0.45 | N/A | 0.78 | [70] |
| Tigris | NiTi | N/A | 6.99 ± 0.45 | N/A | 0.66 | [70] |
| Misago | NiTi | N/A | 6.99 ± 0.45 | N/A | 0.68 | [70] |
| Complete SE | NiTi | N/A | 6.99 ± 0.45 | N/A | 0.9 | [70] |
| AM Simple Honeycomb | Ti64 | 580 ± 26 | 10 | 19.89 | 61.17 | [17] |
| AM Novel Design Etched | Ti64 | 246 ± 36 | 10 | 18.59 | 3.67 ± 1.17 | [17] |
| AM Honeycomb Etched | Ti64 | 152 ± 43 | 10 | 19.89 | 0.45 ± 0.12 | [17] |

## 5.4 Flexibility

Like strut thickness and radial stiffness results, increased flexibility is seen with post processing. In the case of the as built and combined chemically etched and sandblasted, struts fractured during mechanical testing. The addition of a 5 minute chemical etching cycle in fresh solution removed this issue and increased flexibility further. These results indicate that chemical etching parameters, such as solution volume, may need to be adjusted based on a given stent volume or mass. In this case, the longer stents with greater surface area led to a decrease in the efficiency of etching and thus required a larger volume of etching solution. Overall, a 98% reduction in bending stiffness and 92% reduction in maximum force was achieved between the as built and most flexible post processed AM stents.

Comparing with the commercial IntraStent, the AM devices experienced much less permanent deformation as seen in offering increased flexibility and recovery over contemporary commercial devices. Overall, these results, with an emphasis on the AM stent with no fractures, show the capability of AM stents traversing tortuous vessels easily and imposing a lower force on vessels during travel to the delivery site than commercial devices. This could potentially decrease the likelihood of vessel straightening post-delivery and thus decrease the potential for complications for patients post-procedure. It is of interest to note that the work of Kim et al. [96] concluded that the stent design architecture has the greatest influence on stent flexibility, and is thus design and material dependent.

Comparing with reported AM and commercial stents shown in Table 15, the stents in this work have a lower bending stiffness than those reported in Omar *et al.* [15] and has roughly 50% lower bending stiffness than the Multi-Link Vision reported in the same paper. Comparing with the NiTi stents measured in Maleckis *et al.* [76], the AM stents in this work are much stiffer, but this is expected due to the woven construction of these NiTi stents allowing for greater flexibility and elasticity overall. In summary, this work has produced AM stents with the lowest bending stiffness to date, reported values lower than some CoCr commercial devices and are stiffer than commercial NiTi stents.

Table 15 Comparison of flexural stiffness results for AM stents and commercial stents in the literature. Results from this work are given in bold.

| Stent Type | Material | Stut Thickness (um) | Diameter (mm) | Length (mm) | Flexural Stiffness (N/mm) | Source |
|---|---|---|---|---|---|---|
| **As Built** | **Ti64** | **432.52 ± 0.04** | **12** | **45** | **6.24 ± 0.04** | |
| **SB120CE27.5** | **Ti64** | **~300** | **12** | **45** | **0.29 ± 0.02** | |
| **SB120CE27.5CE5** | **Ti64** | **~200** | **12** | **45** | **0.15 ± 0.04** | |
| AM Type 1 | CoCroMo | 200 | 5 | 80 | 0.44 | [15] |
| AM Type 2 | CoCroMo | 180 | 5 | 804 | 0.17 | [15] |
| AM Type 3 | CoCroMo | 200 | 5 | 804 | 0.36 | [15] |
| AM Type 4 | CoCroMo | 180 | 5 | 80 | 0.36 | [15] |
| AM Type 5 | CoCroMo | 200 | 5 | 80 | 0.17 | [15] |
| AM Type 6 | CoCroMo | 200 | 5 | 80 | 0.18 | [15] |
| AM Type 7 | CoCroMo | 180 | 5 | 80 | 0.19 | [15] |
| Multi Link Vision | CoCr | N/A | 3 | N/A | 0.31 | [15] |
| Liberte | N/A | 97 | N/A | N/A | 0.17 | [15] |
| Driver Sprint | N/A | N/A | N/A | N/A | 0.08 | [15] |
| Gazelle | N/A | N/A | N/A | N/A | 0.3 | [15] |
| Absolute Pro | NiTi | N/A | 6.99 ± 0.45 | N/A | 0.02 | [70] |
| Supera | NiTi | N/A | 6.99 ± 0.45 | N/A | 0.03 | [70] |
| LifeStent | NiTi | N/A | 6.99 ± 0.45 | N/A | 0.02 | [70] |
| Innova | NiTi | N/A | 6.99 ± 0.45 | N/A | 0.03 | [70] |
| Zilver | NiTi | N/A | 6.99 ± 0.45 | N/A | 0.04 | [70] |
| Smart Control | NiTi | N/A | 6.99 ± 0.45 | N/A | 0.01 | [70] |
| Smart Flex | NiTi | N/A | 6.99 ± 0.45 | N/A | 0.05 | [70] |
| EverFlex | NiTi | N/A | 6.99 ± 0.45 | N/A | 0.05 | [70] |
| Viabahn | NiTi | N/A | 6.99 ± 0.45 | N/A | 0.01 | [70] |
| Tigris | NiTi | N/A | 6.99 ± 0.45 | N/A | 0.01 | [70] |
| Misago | NiTi | N/A | 6.99 ± 0.45 | N/A | 0.01 | [70] |
| Complete SE | NiTi | N/A | 6.99 ± 0.45 | N/A | 0.04 | [70] |

## 5.5 Stent Crimping & Permanent Deformation

In the assessment of crimping behaviour, no fractures were seen compressing from a 12 mm diameter onto a 2 mm diameter catheter. A large amount of radial recoil was seen, re-expanding to 7.5 mm upon release. As previously discussed, this may be advantageous for placing AM devices within delivery systems but leads to questions about over-expansion requirements for a given lumen gain target.

In the context of the tapered stent results presented in Figure 64, it is difficult to compare these results as the stents fractured during the crimping process. This indicates that the post-processing parameters used for these devices require further optimization and investigation.

It is not possible to compare the results presented in this work to the elastic recoil results reported for commercial stents in the literature presented in Table 16 due to the method of measurement. Typically, stents are expanded then elastic recoil is measured as the final expansion diameter after balloon deflation whereas this work investigated elastic recoil after crimping. Future work may include printing devices in the crimped state and using balloon expansion to compare elastic recoil to commercially available stents.

Overall, the AM stents tested in this work were very elastic with little to no permanent deformation after mechanical testing. These results indicate that these AM stents are more elastic than typical balloon expandable stents available.

Table 16 Comparison of elastic recoil results for stents for commercial stents in the literature

| Stent Type | Material | Diameter (mm) | Length (mm) | Elastic Recoil (%) | Source |
|---|---|---|---|---|---|
| BeStent | Steel | 3 | 18 | 1.54 ± 0.81 | [52] |
| Crossflex | Steel | 3 | 15 | 2.14 ± 0.83 | [52] |
| Helistent | SS316L | 3 | 16 | 2.41 ± 0.76 | [52] |
| NIR 7 | Steel | 3 | 16 | 2.45 ± 0.59 | [52] |
| Crossflex LC | SS316L | 3 | 18 | 2.71 ± 0.40 | [52] |
| PC Coated Stent | Steel | 3-4 | 15 | 2.80 ± 0.82 | [52] |
| GFX | SS316L | 3 | 18 | 2.97 ± 1.72 | [52] |
| CIA | Steel | 3 | 14 | 3.30 ± 1.00 | [52] |
| RX Duet | SS316L | 3 | 18 | 3.43 ± 0.64 | [52] |
| Phytis | Steel | 3 | 16 | 3.69 ± 129 | [52] |
| MiniCrown | SS316L | 3 | 17 | 3.87 ± 0.46 | [52] |
| Crown CR153 | SS316L | 3-4 | 15 | 3.92 ± 0.32 | [52] |
| Sequence Stent | Steel | 3 | 18 | 4.28 ± 0.33 | [52] |
| Tenax Complete | SS316L | 3 | 15 | 4.79 ± 0.90 | [52] |
| PS 154 | SS316L | 3-5 | 15 | 4.92 ± 0.99 | [52] |
| PS 153 | SS316L | 3-6 | 15 | 5.40 ± 1.29 | [52] |
| Multilink HP | SS316L | 3 | 15 | 5.43 ± 1.40 | [52] |
| MicroStent II | SS316L | 3 | 18 | 6.72 ± 1.89 | [52] |
| Wiktor | Tantalum | 3 | 16 | 7.72 ± 1.06 | [52] |
| XT Stent | SS316L | 3 | 15 | 8.69 ± 4.42 | [52] |
| AngioStent | Platinum | 3 | 15 | 8.76 ± 3.16 | [52] |
| GRII | Steel | 3 | 20 | 11.00 ± 3.1 | [52] |
| ParagonE | NiTi | 3 | 16 | 16.51 ± 2.89 | [52] |

## 5.6 Pushing Boundaries of Stent Manufacturing

Overall, this work led to the successful production of open cell AM stent designs with a lower radial stiffness and increased flexibility compared to commercial stents and previous AM stent work. The use of post-processing in this context enables the fabrication of a wide range of strut thicknesses in a controllable and reproducible manner. The combination of sandblasting and then chemical etching is key to this, sandblasting leads to a more even surface finish through defect removal enabling more homogenous and efficient material removal with chemical etching. The correlations between chemical etching times, strut thickness and radial stiffness show the potential in creating stents with tuneable local mechanical properties such as varied thickness to achieve a desired radial stiffness or flexibility profile along a stent length.

The successful production and post processing of a tapered stent design with AM shows the potential in using AM to realize stents designs that are difficult to fabricate with conventional manufacturing techniques such as those seen in Figure 67. Within the context of tapered and non-uniform strut designs, an investigation of print parameters and strut thickness capabilities is required. In order to print stents with variable thickness, the ability to change the print parameters, namely the hatch scan definition, should be changed to ensure uniform print properties along the length of the stent. This is currently not possible with the commercial 3D metal printers available. Additionally, AM has the potential to decrease prototyping and process development time for devices that may be more suited for treatment of congenital heart disease or paediatric use cases by not required bespoke stent tubing or complicated laser fabrication techniques.

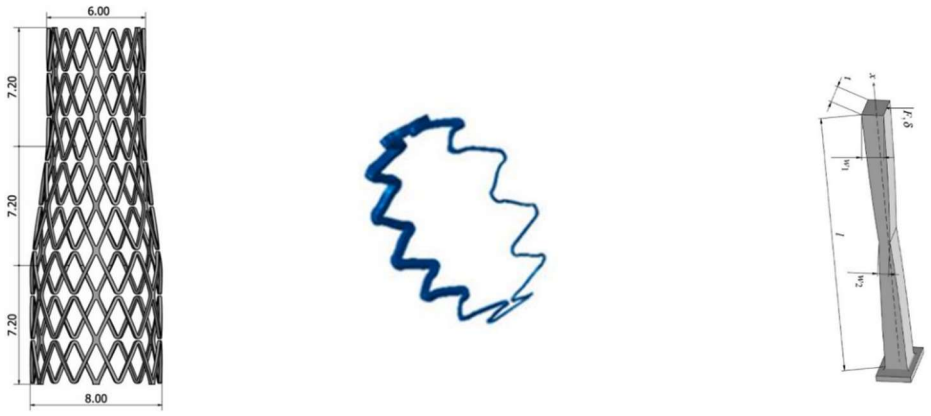


Figure 66 Examples varied diameter, varied thickness, and tapered strut profile stents [9], [10],[11]

## 5.7 Towards Patient Specific Designs with AM

As shown, pushing the boundaries of stent manufacturing with AM may enable the commercial viability of patient specific stents for cases with a clear clinical need such as aortic coarctation. AM offers rapid manufacturing capabilities for bespoke stents and potential for tuneable geometric and mechanical properties as required. The potential to combine this technology with medical imaging used in pre-clinical assessment and computational modelling for device design may enable patient specific devices in this context. A potential workflow is illustrated in Figure 68.

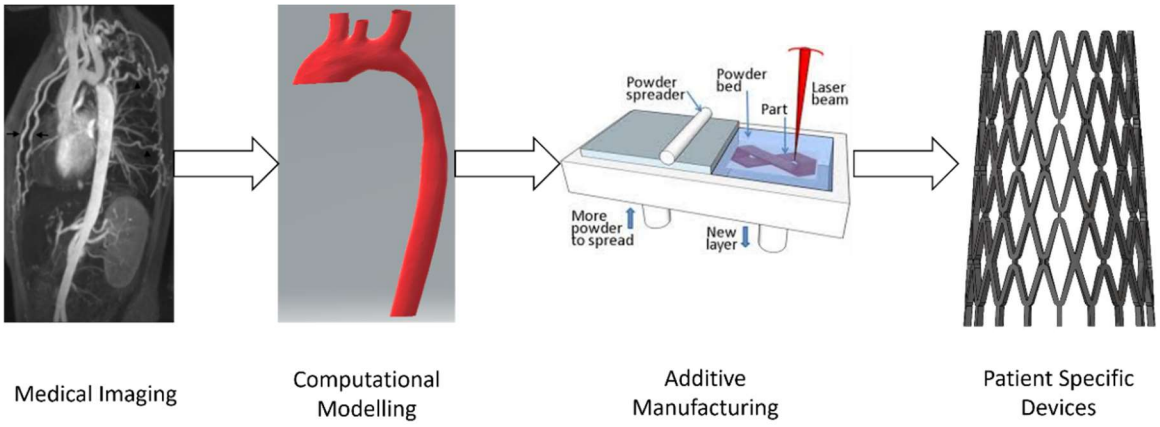


Figure 67 Potential workflow for development of patient specific devices

# Chapter 6. Conclusions

This work has demonstrated the feasibility of recreating and adapting open cell commercial stent designs and fabricating them using additive manufacturing and post-processing techniques. These devices offer radial stiffness tunability,, greater bending flexibility and overall elasticity compared to contemporary commercial stents and AM stents presented in the literature.

The development of the tapered stent design in this work pushes the boundaries of stent manufacturing in the context of AM. These devices are no longer constrained by typical laser cut tubing considerations nor do they require self-supporting designs to be compatible with AM due to the post-processing technique presented in this work.

Overall, by enabling rapid prototyping and feasible manufacturing of these bespoke devices, patient or disease specific devices may become commercially viable with further development.

# Bibliography


[1] R. D. Torok, "Coarctation of the aorta: Management from infancy to adulthood," *World J. Cardiol.*, vol. 7, no. 11, p. 765, 2015, doi: 10.4330/wjc.v7.i11.765.

[2] H. Suradi and Z. M. Hijazi, "Current management of coarctation of the aorta," *Glob. Cardiol. Sci. Pract.*, vol. 2015, no. 4, pp. 1–11, Sep. 2015, doi: 10.5339/gcsp.2015.44.

[3] T. J. Forbes *et al.*, "Intermediate follow-up following intravascular stenting for treatment of coarctation of the aorta," *Catheter. Cardiovasc. Interv.*, vol. 70, no. 4, pp. 569–577, Oct. 2007, doi: 10.1002/ccd.21191.

[4] A. D. Karaosmanoglu, R. D. A. Khawaja, M. R. Onur, and M. K. Kalra, "CT and MRI of Aortic Coarctation: Pre- and Postsurgical Findings," *Am. J. Roentgenol.*, vol. 204, no. 3, pp. W224–W233, Mar. 2015, doi: 10.2214/AJR.14.12529.

[5] B. O'Brien and W. Carroll, "The evolution of cardiovascular stent materials and surfaces in response to clinical drivers: A review," *Acta Biomater.*, vol. 5, no. 4, pp. 945–958, May 2009, doi: 10.1016/j.actbio.2008.11.012.

[6] F. Ing, "Stents: What{\textquotesingle}s available to the pediatric interventional cardiologist?," *Catheter. Cardiovasc. Interv.*, vol. 57, no. 3, pp. 374–386, Oct. 2002, doi: 10.1002/ccd.10342.

[7] R. Holzer and Z. Hijazi, "The off-versus on-label use of medical devices in interventional cardiovascular medicine?: Clarifying the ambiguity between regulatory labeling and clinical decision making, Part {III}: Structural heart disease interventions," *Catheter. Cardiovasc. Interv.*, vol. 72, no. 6, pp. 848–852, Nov. 2008, doi: 10.1002/ccd.21708.

[8] K. Shibbani, D. Kenny, D. McElhinney, Z. M. Hijazi, and T. Moran, "Identifying Gaps in Technology for Congenital Interventions: Analysis of a Needs Survey from Congenital Interventional Cardiologists," *Pediatr. Cardiol.*, vol. 37, no. 5, pp. 925–931, Apr. 2016, doi: 10.1007/s00246-016-1372-0.

[9] S. Maffia *et al.*, "Selective laser melting of {NiTi} stents with open-cell and variable diameter," *Smart Mater. Struct.*, vol. 30, no. 10, p. 105010, Aug. 2021, doi: 10.1088/1361-665x/ac1908.

[10] R. He, L. Zhao, V. V. Silberschmidt, H. Willcock, and F. Vogt, "Pioneering personalised design of femoropopliteal nitinol stents," *Mater. Sci. Eng. C*, vol. 130, no. July, p. 112462, Nov. 2021, doi: 10.1016/j.msec.2021.112462.

[11] G. Alaimo, F. Auricchio, M. Conti, and M. Zingales, "Multi-objective optimization of nitinol stent design," *Med. Eng. {\&} Phys.*, vol. 47, pp. 13–24, Sep. 2017, doi: 10.1016/j.medengphy.2017.06.026.

[12] G. M. N. C. K. S. S. W. S. K.-P. H. H. Wessarges Y. Hagemann R., "Additive Manufacturing of Vascular Implants by Selective Laser Melting," *Biomed Tech*, 2014.

[13] A. G. Demir and B. Previtali, "Additive manufacturing of cardiovascular {CoCr} stents by selective laser melting," *Mater. {\&} Des.*, vol. 119, pp. 338–350, Apr. 2017, doi: 10.1016/j.matdes.2017.01.091.

[14] V. Finazzi, A. G. Demir, C. A. Biffi, F. Migliavacca, L. Petrini, and B. Previtali,

"Design and functional testing of a novel balloon-expandable cardiovascular stent in {CoCr} alloy produced by selective laser melting," *J. Manuf. Process.*, vol. 55, pp. 161–173, Jul. 2020, doi: 10.1016/j.jmapro.2020.03.060.

[15] M. A. Omar, B. T. H. T. Baharudin, S. Sulaiman, M. I. S. Ismail, and M. A. Omar, "Evaluation of chemical composition, heat treatment, mechanical properties and electro chemical polishing for additively manufactured stent using {ASTM} F75 cobalt based superalloy ({CoCrMo}) by selective laser melting ({SLM}) technology.," *Adv. Mater. Process. Technol.*, pp. 1–20, Dec. 2020, doi: 10.1080/2374068x.2020.1860598.

[16] E. Langi *et al.*, "Microstructural and Mechanical Characterization of Thin-Walled Tube Manufactured with Selective Laser Melting for Stent Application," *J. Mater. Eng. Perform.*, vol. 30, no. 1, pp. 696–710, Jan. 2021, doi: 10.1007/s11665-020-05366-9.

[17] O. M. McGee *et al.*, "An Investigation into Patient-Specific 3D Printed Titanium Stents and the use of Etching to Overcome Selective Laser Melting Design Constraints," *J. Mech. Behav. Biomed. Mater.*, vol. In Press, Mar. 2022, doi: 10.1101/2021.03.07.434132.

[18] V. Finazzi *et al.*, "Design rules for producing cardiovascular stents by selective laser melting: Geometrical constraints and opportunities," *Procedia Struct. Integr.*, vol. 15, pp. 16–23, Jan. 2019, doi: 10.1016/j.prostr.2019.07.004.

[19] A. M. da Silva Costa *et al.*, "Co–Cr–Mo alloy fabricated by laser powder bed fusion process: grain structure, defect formation, and mechanical properties," *Int. J. Adv. Manuf. Technol.*, vol. 116, no. 7–8, pp. 2387–2399, 2021, doi: 10.1007/s00170-021-07570-w.

[20] J. Suryawanshi, K. G. Prashanth, and U. Ramamurty, "Mechanical behavior of selective laser melted 316L stainless steel," *Mater. Sci. Eng. A*, vol. 696, no. April, pp. 113–121, 2017, doi: 10.1016/j.msea.2017.04.058.

[21] G. Kasperovich and J. Hausmann, "Improvement of fatigue resistance and ductility of TiAl6V4 processed by selective laser melting," *J. Mater. Process. Technol.*, vol. 220, pp. 202–214, 2015, doi: 10.1016/j.jmatprotec.2015.01.025.

[22] L. Wiesent *et al.*, "Computational analysis of the effects of geometric irregularities and post-processing steps on the mechanical behavior of additively manufactured 316L stainless steel stents," *{PLOS} {ONE}*, vol. 15, no. 12, p. e0244463, Dec. 2020, doi: 10.1371/journal.pone.0244463.

[23] M. Grad, N. Nadammal, U. Schultheiss, P. Lulla, and U. Noster, "An integrative experimental approach to design optimization and removal strategies of supporting structures used during L-PBF of SS316L aortic stents," *Appl. Sci.*, vol. 11, no. 19, p. 9176, Oct. 2021, doi: 10.3390/app11199176.

[24] T. H. William, *Chemical Milling The technology of cutting materials by Etching*. Clarendon Press, 1976.

[25] K. S. Chan, M. Koike, B. W. Johnson, and T. Okabe, "Modeling of alpha-case formation and its effects on the mechanical properties of titanium alloy castings," *Metall. Mater. Trans. A Phys. Metall. Mater. Sci.*, vol. 39, no. 1, pp. 171–180, 2008, doi: 10.1007/s11661-007-9406-0.

[26] A. Balyakin, E. Goncharov, and E. Zhuchenko, “The effect of preprocessing on surface quality in the chemical polishing of parts from titanium alloy produced by SLM,” *Mater. Today Proc.*, vol. 19, pp. 2291–2294, 2019, doi: 10.1016/j.matpr.2019.07.671.

[27] P. Lhuissier, C. de Formanoir, G. Martin, R. Dendievel, and S. Godet, “Geometrical control of lattice structures produced by EBM through chemical etching: Investigations at the scale of individual struts,” *Mater. Des.*, vol. 110, pp. 485–493, Nov. 2016, doi: https://doi.org/10.1016/j.matdes.2016.08.029.

[28] G. Pyka, G. Kerckhofs, I. Papantoniou, M. Speirs, J. Schrooten, and M. Wevers, “Surface Roughness and Morphology Customization of Additive Manufactured Open Porous Ti6Al4V Structures,” *Materials (Basel).*, vol. 6, no. 10, pp. 4737–4757, 2013, doi: 10.3390/ma6104737.

[29] T. Persenot, J.-Y. Buffiere, E. Maire, R. Dendievel, and G. Martin, “Fatigue properties of {EBM} as-built and chemically etched thin parts,” *Procedia Struct. Integr.*, vol. 7, pp. 158–165, 2017, doi: 10.1016/j.prostr.2017.11.073.

[30] M. Bezuidenhout, G. Ter Haar, T. Becker, S. Rudolph, O. Damm, and N. Sacks, “The effect of {HF}-{HNO}3 chemical polishing on the surface roughness and fatigue life of laser powder bed fusion produced Ti6Al4V,” *Mater. Today Commun.*, vol. 25, p. 101396, Dec. 2020, doi: 10.1016/j.mtcomm.2020.101396.

[31] C. de Formanoir, M. Suard, R. Dendievel, G. Martin, and S. Godet, “Improving the mechanical efficiency of electron beam melted titanium lattice structures by chemical etching,” *Addit. Manuf.*, vol. 11, pp. 71–76, Jul. 2016, doi: 10.1016/j.addma.2016.05.001.

[32] S. M. Ahmadi *et al.*, “From microstructural design to surface engineering: A tailored approach for improving fatigue life of additively manufactured meta-biomaterials,” *Acta Biomater.*, vol. 83, pp. 153–166, Jan. 2019, doi: 10.1016/j.actbio.2018.10.043.

[33] K. Karami *et al.*, “Continuous and pulsed selective laser melting of Ti6Al4V lattice structures: Effect of post-processing on microstructural anisotropy and fatigue behaviour,” *Addit. Manuf.*, vol. 36, p. 101433, Dec. 2020, doi: 10.1016/j.addma.2020.101433.

[34] Y. Y. Sun *et al.*, “Fatigue Performance of Additively Manufactured Ti-6Al-4V: Surface Condition vs. Internal Defects,” *JOM*, vol. 72, no. 3, pp. 1022–1030, Jan. 2020, doi: 10.1007/s11837-020-04025-7.

[35] R. L. Mueller and T. A. Sanborn, “The history of interventional cardiology: Cardiac catheterization, angioplasty, and related interventions,” *Am. Heart J.*, vol. 129, no. 1, pp. 146–172, Jan. 1995, doi: 10.1016/0002-8703(95)90055-1.

[36] C. T. Dotter and M. P. Judkins, “Transluminal Treatment of Arteriosclerotic Obstruction,” *Circulation*, vol. 30, no. 5, pp. 654–670, Nov. 1964, doi: 10.1161/01.cir.30.5.654.

[37] C. T. Dotter, “Transluminally-placed Coilspring Endarterial Tube Grafts,” *Invest. Radiol.*, vol. 4, no. 5, pp. 329–332, Sep. 1969, doi: 10.1097/00004424-196909000-00008.

[38] R. A. Schatz, “A view of vascular stents.,” *Circulation*, vol. 79, no. 2, pp. 445–457, Feb. 1989, doi: 10.1161/01.CIR.79.2.445.

[39] C. T. Dotter, R. W. Buschmann, M. K. McKinney, J. Rösch, and J. Rosch, "Transluminal expandable nitinol coil stent grafting: preliminary report.," *Radiology*, vol. 147, no. 1, pp. 259–260, Apr. 1983, doi: 10.1148/radiology.147.1.6828741.

[40] J. C. Palmaz, R. R. Sibbitt, S. R. Reuter, F. O. Tio, and W. J. Rice, "Expandable intraluminal graft: a preliminary study. Work in progress.," *Radiology*, vol. 156, no. 1, pp. 73–77, Jul. 1985, doi: 10.1148/radiology.156.1.3159043.

[41] MicroChemicals, "02. Wet etching metals Al Au Cu Cr Ni Ti Ag," p. 7, [Online]. Available: www.microchemicals.com/downloads/application_notes.html.

[42] T. Watson, M. W. I. Webster, J. A. Ormiston, P. N. Ruygrok, and J. T. Stewart, "Long and short of optimal stent design," *Open Hear.*, vol. 4, no. 2, pp. 1–6, 2017, doi: 10.1136/openhrt-2017-000680.

[43] J. C. Palmaz, "Balloon-expandable intravascular stent," *Am. J. Roentgenol.*, vol. 150, no. 6, pp. 1263–1269, Jun. 1988, doi: 10.2214/ajr.150.6.1263.

[44] T. W. Duerig, M. Wholey, and M. Dunitz, "A comparison of balloon- and self-expanding stents," *Minim. Invasive Ther. {\&} Allied Technol.*, vol. 11, no. 4, pp. 173–178, Jan. 2002, doi: 10.1080/136457002760273386.

[45] U. Sigwart, J. Puel, V. Mirkovitch, F. Joffre, and L. Kappenberger, "Intravascular Stents to Prevent Occlusion and Re-Stenosis after Transluminal Angioplasty," *N. Engl. J. Med.*, vol. 316, no. 12, pp. 701–706, Mar. 1987, doi: 10.1056/nejm198703193161201.

[46] H.-Y. Song, J. H. Kim, and C. J. Yoon, "History of Self-Expandable Metal and Self-Expandable Plastic Stent Development," in *Self-Expandable Stents in the Gastrointestinal Tract*, Springer New York, 2012, pp. 35–49.

[47] J. Friedrich, J. Vogel, J. Görich, A. Rieber, N. Rilinger, and H.-J. Brambs, "Erste klinische Erfahrung mit einem neuen Nitinolstent im biliären System," *{RöFo} - Fortschritte auf dem Gebiet der Röntgenstrahlen und der Bildgeb. Verfahren*, vol. 162, no. 05, pp. 429–435, May 1995, doi: 10.1055/s-2007-1015910.

[48] "ISO 25539-2:2020, Cardiovascular implants — Endovascular devices — Part 2: Vascular stents."

[49] ASTM F3067-14, "Guide for Radial Loading of Balloon Expandable and Self Expanding," pp. 1–19, 2014, doi: 10.1520/f3067-14.

[50] "Non-Clinical Engineering Tests and Recommended Labeling for Intravascular Stents and Associated Delivery Systems - Guidance for Industry and FDA Staff," 2011.

[51] T. Specimens and T. Units, "ASTM F2079, Test Method for Measuring Intrinsic Elastic Recoil of Balloon-Expandable Stents," vol. 02, no. June 2008, pp. 2008–2010, 2009, doi: 10.1520/f2079-09r17.

[52] P. Barragan *et al.*, "Elastic recoil of coronary stents: A comparative analysis," *Catheter. Cardiovasc. Interv.*, vol. 50, no. 1, pp. 112–119, May 2000, doi: 10.1002/(sici)1522-726x(200005)50:1<112::aid-ccd25>3.0.co;2-x.

[53] Y. Yamamoto, D. L. Brown, T. A. Ischinger, A. Arbab-Zadeh, and W. F. Penny, "Effect of stent design on reduction of elastic recoil: A comparison via quantitative intravascular ultrasound," *Catheter. Cardiovasc. Interv.*, vol. 47, no. 2, pp. 251–257,

Jun. 1999, doi: 10.1002/(sici)1522-726x(199906)47:2<251::aid-ccd26>3.0.co;2-m.

[54] C. Lally, D. J. J. Kelly, and P. J. J. Prendergast, "Stents," in *Wiley Encyclopedia of Biomedical Engineering*, Hoboken, NJ, USA: American Cancer Society, 2006.

[55] C. Brandt-Wunderlich, C. Schwerdt, P. Behrens, N. Grabow, K.-P. Schmitz, and W. Schmidt, "A method to determine the kink resistance of stents and stent delivery systems according to international standards," *Curr. Dir. Biomed. Eng.*, vol. 2, no. 1, pp. 289–292, Sep. 2016, doi: 10.1515/cdbme-2016-0064.

[56] ASTM, "Standard Guide for Three-Point Bending of Balloon Expandable Vascular Stents," *Astm*, vol. 08, no. October, pp. 4–9, 2015, doi: 10.1520/F2606-08R14.2.1.4.

[57] D. M. Wiktor, S. W. Waldo, and E. J. Armstrong, "Coronary Stent Failure: Fracture, Compression, Recoil, and Prolapse," *Interv. Cardiol. Clin.*, vol. 5, no. 3, pp. 405–414, 2016, doi: 10.1016/j.iccl.2016.03.004.

[58] G. Leibundgut *et al.*, "Longitudinal compression of the platinum-chromium everolimus-eluting stent during coronary implantation: Predisposing mechanical properties, incidence, and predictors in a large patient cohort," *Catheter. Cardiovasc. Interv.*, vol. 81, no. 5, pp. E206--E214, Nov. 2012, doi: 10.1002/ccd.24472.

[59] J. A. Ormiston, B. Webber, B. Ubod, J. White, and M. W. I. Webster, "Stent Longitudinal Strength Assessed Using Point Compression," *Circ. Cardiovasc. Interv.*, vol. 7, no. 1, pp. 62–69, Feb. 2014, doi: 10.1161/circinterventions.113.000621.

[60] ASTM F2081-01, "ASTM F2081, Guide for Characterization and Presentation of the Dimensional Attributes of Vascular Stents," *Current*, vol. 06, no. April, pp. 1–4, 2001, doi: 10.1520/F2081-06R17.1.6.

[61] "ASTM F2394, Guide for Measuring Securement of Balloon Expandable Vascular Stent Mounted on Delivery System." doi: 10.1520/f2394-07r17.

[62] ASTM, "ASTM F239 - Standard Guide for Measuring Securement of Balloon Expandable Vascular Stent Mounted on Delivery System 1," *Astm*, vol. 07, no. Reapproved, pp. 1–13, 2013, doi: 10.1520/F2394-07R17.2.

[63] W. M. P. F. Bosman, B. L. S. B. van der Burg, H. M. Schuttevaer, S. Thoma, and P. P. H. Joosten, "Infections of Intravascular Bare Metal Stents: A Case Report and Review of Literature," *Eur. J. Vasc. Endovasc. Surg.*, vol. 47, no. 1, pp. 87–99, Jan. 2014, doi: 10.1016/j.ejvs.2013.10.006.

[64] "ISO 11135:2014, Sterilization of health-care products — Ethylene oxide."

[65] "ISO 17666:2006 ,Sterilization of health care products — Moist heat."

[66] "ISO 11137:2017, Sterilization of health care products — Radiation."

[67] "ASTM F640, Test Methods for Determining Radiopacity for Medical Use." doi: 10.1520/f0640-20.

[68] K. Kolandaivelu and F. Rikhtegar, "The Systems Biocompatibility of Coronary Stenting," *Interv. Cardiol. Clin.*, vol. 5, no. 3, pp. 295–306, Jul. 2016, doi: 10.1016/j.iccl.2016.02.001.

[69] "ISO 10993:2018, Biological evaluation of medical devices."

[70] K. K. Kapnisis, D. O. Halwani, B. C. Brott, P. G. Anderson, J. E. Lemons, and A. S. Anayiotos, "Stent overlapping and geometric curvature influence the structural integrity and surface characteristics of coronary nitinol stents," *J. Mech. Behav. Biomed. Mater.*, vol. 20, pp. 227–236, Apr. 2013, doi: 10.1016/j.jmbbm.2012.11.006.

[71] "ASTM F2129, Test Method for Conducting Cyclic Potentiodynamic Polarization Measurements to Determine the Corrosion Susceptibility of Small Implant Devices." doi: 10.1520/f2129-19a.

[72] C. Trépanier, X.-Y. Gong, T. Ditter, A. Pelton, Y. Neely, and R. Grishaber, "Effect of Wear and Crevice on the Corrosion Resistance of Overlapped Stents," *SMST-2006 - Proc. Int. Conf. Shape Mem. Superelastic Technol.*, 2006, doi: 10.1361/cp2006smst265.

[73] "ASTM G71, Guide for Conducting and Evaluating Galvanic Corrosion Tests in Electrolytes." doi: 10.1520/g0071-81r19.

[74] F. Testing and P. D. Testing, "Standard Guide for Fatigue-to-Fracture ( FtF ) Methodology for Cardiovascular," vol. 2016, pp. 1–14, 2021, doi: 10.1520/F3211-17.2.

[75] "ASTM F2942, Guide for in vitro Axial, Bending, and Torsional Durability Testing of Vascular Stents." doi: 10.1520/f2942-19.

[76] K. Maleckis *et al.*, "Comparison of femoropopliteal artery stents under axial and radial compression, axial tension, bending, and torsion deformations," *J. Mech. Behav. Biomed. Mater.*, vol. 75, no. June, pp. 160–168, Nov. 2017, doi: 10.1016/j.jmbbm.2017.07.017.

[77] Astm, "Standard Guide for in vitro Axial , Bending , and Torsional Durability Testing of," *Astm*, vol. i, pp. 1–15, 2014, doi: 10.1520/F2942-19.cadaver.

[78] ASTM, "ASTM F2447, Test Methods for in vitro Pulsatile Durability Testing of Vascular Stents," *Current*, vol. 07, no. C, pp. 1–10, 2011, doi: 10.1520/F2477-19.1.9.

[79] S. Materials, "Standard Test Method for Measurement of Magnetically Induced Displacement Force," pp. 4–9, 2013, doi: 10.1520/F2052-15.Copyright.

[80] M. R. Environment, "ASTM F2213, Test Method for Measurement of Magnetically Induced Torque on Medical Devices in the Magnetic Resonance Environment," *Annu. B. ASTM Stand.*, vol. 06, no. Reapproved 2011, pp. 1–8, 2012, doi: 10.1520/F2213-17.1.

[81] M. R. Environment, "ASTM F2182, Test Method for Measurement of Radio Frequency Induced Heating On or Near Passive Implants During Magnetic Resonance Imaging," *Annu. B. ASTM Stand.*, vol. i, no. December, pp. 1–12, 2002, doi: 10.1520/f2182-19e02.

[82] American Society for Testing and Materials, "Standard Test Method for Evaluation of MR Image Artifacts from Passive Implants (F2119-07)," *ASTM Int.*, vol. 07, no. Reapproved 2013, pp. 1–4, 2010, doi: 10.1520/F2119-07R13.2.

[83] J. F. Dyet, W. G. Watts, D. F. Ettles, and A. A. Nicholson, "Mechanical properties of metallic stents: How do these properties influence the choice of stent for specific lesions?," *Cardiovasc. Intervent. Radiol.*, vol. 23, no. 1, pp. 47–54, Jan. 2000, doi: 10.1007/s002709910007.

[84] S. V. Lossef, R. J. Lutz, J. Mundorf, and K. H. Barth, “Comparison of Mechanical Deformation Properties of Metallic Stents with Use of Stress-Strain Analysis,” *J. Vasc. Interv. Radiol.*, vol. 5, no. 2, pp. 341–349, Mar. 1994, doi: 10.1016/S1051-0443(94)71499-8.

[85] L. A. Garcia, S. E. Hosley, D. S. Baim, and J. P. Carrozza, “In vivo assessment of stent recoil in normal porcine arteries: Evaluation of contemporary stent designs,” *Catheter. Cardiovasc. Interv.*, vol. 53, no. 2, pp. 277–280, 2001, doi: 10.1002/ccd.1165.

[86] W. Schmidt, R. Andresen, P. BEHRENS, and K.-P. SCHMITZ, “Comparison of mechanical properties of peripheral self-expanding Nitinol and balloon-expandable stainless-steel stents,” 2004.

[87] R. Wang and K. Ravi-Chandar, “Mechanical response of a metallic aortic stent - Part I: Pressure-diameter relationship,” *J. Appl. Mech. Trans. ASME*, vol. 71, no. 5, pp. 697–705, 2004, doi: 10.1115/1.1782650.

[88] H. Isayama *et al.*, “Measurement of radial and axial forces of biliary self-expandable metallic stents,” *Gastrointest. Endosc.*, vol. 70, no. 1, pp. 37–44, Jul. 2009, doi: 10.1016/j.gie.2008.09.032.

[89] M. Hirdes, F. Vleggaar, M. de Beule, and P. Siersema, “In vitro evaluation of the radial and axial force of self-expanding esophageal stents,” *Endoscopy*, vol. 45, no. 12, pp. 997–1005, Nov. 2013, doi: 10.1055/s-0033-1344985.

[90] C. R. Johnston, K. Lee, J. Flewitt, R. Moore, G. M. Dobson, and G. M. Thornton, “The Mechanical Properties of Endovascular Stents: An In Vitro Assessment,” *Cardiovasc. Eng.*, vol. 10, no. 3, pp. 128–135, Aug. 2010, doi: 10.1007/s10558-010-9097-9.

[91] “ISO - ISO 4288:1996 - Geometrical Product Specifications (GPS) — Surface texture: Profile method — Rules and procedures for the assessment of surface texture.” .

[92] B. Van Hooreweder, K. Lietaert, B. Neirinck, N. Lippiatt, and M. Wevers, “{CoCr} F75 scaffolds produced by additive manufacturing: Influence of chemical etching on powder removal and mechanical performance,” *J. Mech. Behav. Biomed. Mater.*, vol. 68, pp. 216–223, Apr. 2017, doi: 10.1016/j.jmbbm.2017.02.005.

[93] ASTM, “E407-07: Standard Practice for Microetching Metals and Alloys,” *ASTM Int. West Conshohocken, PA*, pp. 1–21, 2012.

[94] E. Lyczkowska, P. Szymczyk, B. Dybała, and E. Chlebus, “Chemical polishing of scaffolds made of Ti-6Al-7Nb alloy by additive manufacturing,” *Arch. Civ. Mech. Eng.*, vol. 14, no. 4, pp. 586–594, 2014, doi: 10.1016/j.acme.2014.03.001.

[95] I. Bae *et al.*, “Mechanical behavior and in vivo properties of newly designed bare metal stent for enhanced flexibility,” *J. Ind. Eng. Chem.*, vol. 21, pp. 1295–1300, 2015, doi: 10.1016/j.jiec.2014.05.045.

[96] D. Bin Kim *et al.*, “A Comparative Reliability and Performance Study of Different Stent Designs in Terms of Mechanical Properties: Foreshortening, Recoil, Radial Force, and Flexibility,” *Artif. Organs*, vol. 37, no. 4, pp. 368–379, 2013, doi: 10.1111/aor.12001.